การประมาณแรงสึนามิกระทำต่อสะพานบนชายฝั่งโดยคำนึงถึงรูปแบบครบถ้วน
ของตอม่อและพื้นสะพาน

นาย ที เหลียง หลอ

วิทยานิพนธ์นี้เป็นส่วนหนึ่งของการศึกษาตามหลักสูตรปริญญาวิศวกรรมศาสตรดุษฎีบัณฑิต
สาขาวิชาวิศวกรรมโยธา ภาควิชาวิศวกรรมโยธา
คณะวิศวกรรมศาสตร์ จุฬาลงกรณ์มหาวิทยาลัย
ปีการศึกษา 2552
ลิขสิทธิ์ของจุฬาลงกรณ์มหาวิทยาลัย

TSUNAMI FORCE ESTIMATION ON INLAND BRIDGES
CONSIDERING COMPLETE PIER-DECK CONFIGURATIONS

Mr. Tze Liang Lau

ศูนย์วิทยทรัพยากร
จุฬาลงกรณ์มหาวิทยาลัย

A Dissertation Submitted in Partial Fulfillment of the Requirements
for the Degree of Doctor of Philosophy Program in Civil Engineering
Department of Civil Engineering
Faculty of Engineering
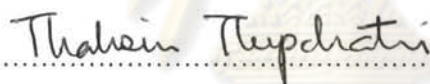Chulalongkorn University
Academic Year 2009

Thesis Title	TSUNAMI FORCE ESTIMATION ON INLAND BRIDGES CONSIDERING COMPLETE PIER-DECK CONFIGURATIONS
By	Mr. Tze Liang Lau
Field of study	Civil Engineering
Thesis Advisor	Professor Panitan Lukkunaprasit, Ph.D.
Thesis Co-advisor	Professor Tatsuo Ohmachi, D.Eng.
	Assistant Professor Anat Ruangrassamee, Ph.D.

Accepted by the Faculty of Engineering, Chulalongkorn University in Partial Fulfillment of Requirements for the Doctoral Degree

.... Dean of the Faculty of Engineering

(Associate Professor Boonsom Lerdhirunwong , Dr.Ing.)

THESIS COMMITTEE

.... Chairman

(Professor Thaksin Thepchatri , Ph.D.)

.... Advisor

(Professor Panitan Lukkunaprasit , Ph.D.)

.... Co-Advisor

(Professor Tatsuo Ohmachi , D.Eng.)

.... Co-Advisor

(Assistant Professor Anat Ruangrassamee , Ph.D.)

.... Examiner

(Associate Professor Taksiah A. Majid , Ph.D.)

ที เหลียง หลอ : การประมาณแรงสึนามิกระทำต่อสะพานบนชายฝั่งโดยคำนึงถึงรูปแบบครบถ้วน
ของตอม่อและพื้นสะพาน.
(TSUNAMI FORCE ESTIMATION ON INLAND BRIDGES CONSIDERING COMPLETE
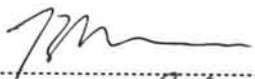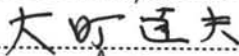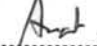PIER-DECK CONFIGURATIONS)
อ.ที่ปรึกษา : ศ.ดร.ปณิธาน ลักคุณะประสิทธิ์, อ.ที่ปรึกษาร่วม : PROF. TATSUO OHMACHI,
ผศ.ดร.อาณัติ เรืองรัศมี, 135 หน้า.

ทฤษฎีสำหรับการประมาณแรงเนื่องจากสึนามิไม่สามารถประยุกต์ใช้ได้โดยง่ายสำหรับสะพานด้วยองค์
ความรู้ในปัจจุบัน เนื่องจากความซับซ้อนของการแพร่กระจายคลื่นน้ำสู่ชายฝั่งและการปฏิสัมพันธ์ระหว่างคลื่นและ
โครงสร้าง งานวิจัยนี้มุ่งเน้นศึกษาลักษณะการไหลของการท่วมบ่าจากสึนามิ (tsunami surge) รอบๆ สะพานที่อยู่
บนชายฝั่ง รวมทั้งค่าความดันและแรงที่กระทำต่อสะพาน แบบจำลองเสาตอม่อเดี่ยวและแบบจำลองเสาตอม่อที่
เชื่อมต่อกับพื้นสะพานโดยสมบูรณ์ถูกทดสอบในรางชลศาสตร์ โดยจำลองตามมาตราส่วนที่ถูกต้องกับโครงสร้าง
สะพานแบบที่มีคานหน้าตัดรูปตัวไอ ได้พิจารณาพื้นสะพาน 5 ลักษณะ ทั้งแบบมีช่องเปิดและไม่มีช่องเปิดบริเวณ
คาน และ/หรือ แผงกันตก จากผลการทดลองแรงจากการท่วมบ่าที่วัดได้บริเวณเสาตอม่อจากแบบจำลองเสาตอม่อ
ที่เชื่อมต่อกับพื้นสะพานโดยสมบูรณ์มีค่ามากกว่าค่าที่วัดได้จากแบบจำลองเสาตอม่อเดี่ยวพอสมควร ซึ่งแสดงให้
เห็นว่าวิธีการคำนวณแรงจากการท่วมบ่าที่กระทำต่อเสาตอม่อที่ใช้ในปัจจุบันจำเป็นต้องได้รับการปรับปรุงสำหรับ
กรณีที่มีปฏิสัมพันธ์ระหว่างเสาตอม่อกับพื้นสะพาน นอกจากนี้สะพานที่คานหรือแผงกันตกมีช่องเปิดซึ่งยังไม่เคยมี
การทำการศึกษามาก่อนสำหรับการบรรเทาความเสี่ยงภัยเนื่องจากสึนามิ แสดงให้เห็นว่าแรงและพลังงานที่ส่งถ่าย
เข้าสู่โครงสร้างนั้นมีค่าลดลงตลอดทั้งช่วงเวลาที่แรงกระทำ

แบบจำลองเชิงตัวเลขที่สอดคล้องกับแบบจำลองทางกายภาพได้ถูกสร้างขึ้นในโปรแกรมที่ทำการคำนวณ
พลศาสตร์ของไหล (computational fluid dynamics) และสอบเทียบกับผลจากการทดสอบในรางชลศาสตร์ จาก
แบบจำลองเชิงตัวเลขที่ทำการสอบเทียบแล้วนำไปปรับเปลี่ยนสำหรับวิเคราะห์กรณีของพื้นสะพานซึ่งแปรเปลี่ยน
ความสูงต่างๆ โดยพิจารณาคลื่นจากเหตุการณ์รุนแรงที่สุด ผลแบบจำลองเชิงตัวเลขยืนยันถึงความจำเป็นที่ต้อง
จำลองสะพานให้มีสภาพเหมือนจริงโดยมีเสาตอม่อและพื้นสะพานโดยครบถ้วน ในกรณีที่จำลองโดยไม่มีเสาตอ
ม่อหรือกรณีจำลองพื้นสะพานแบบคานรูปตัวไอเป็นแบบหน้าตัดกล่องสี่เหลี่ยม ค่าแรงแนวราบและแรงยกสูงสุดที่
กระทำต่อพื้นสะพานขณะที่คลื่นกระทบมีค่าต่ำกว่าค่าที่ได้จากกรณีที่พิจารณารูปแบบสะพานจริงประมาณ 15%
และ 60% ตามลำดับ

สุดท้ายของงานวิจัยนี้ได้เสนอสมการเอ็มพิริคัลที่ใช้ในการประมาณแรงเนื่องจากสึนามิกระทำต่อพื้น
สะพาน โดยแบ่งแรงออกเป็น 4 องค์ประกอบหลัก ได้แก่ แรงสูงสุดแนวราบ, แรงที่เปลี่ยนแปลงอย่างช้าๆ ใน
แนวราบ, แรงยก และแรงโน้มถ่วง ค่าแรงต่างๆ ที่กระทำบนพื้นสะพานสามารถคำนวณได้จากเฉลี่ยของค่าแรงที่
เปลี่ยนแปลงอย่างช้าๆในแนวราบ

ภาควิชา วิศวกรรมโยธา	ลายมือชื่อนิสิต	
สาขาวิชา วิศวกรรมโยธา	ลายมือชื่ออาจารย์ที่ปรึกษา	
ปีการศึกษา 2552	ลายมือชื่ออาจารย์ที่ปรึกษาร่วม	
	ลายมือชื่ออาจารย์ที่ปรึกษาร่วม	
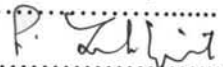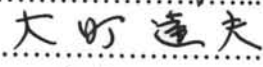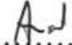
TZE LIANG LAU : TSUNAMI FORCE ESTIMATION ON INLAND BRIDGES CONSIDERING COMPLETE PIER-DECK CONFIGURATIONS. THESIS ADVISOR : PROF. PANITAN LUKKUNAPRASIT, Ph.D., THESIS CO-ADVISORS : PROF. TATSUO OHMACHI, D.Eng., ASST. PROF. ANAT RUANGRASSAMEE, Ph.D., 135 pp.

Theoretical approach for estimating tsunami-induced forces with today's state-of-the-art cannot be easily applied for bridges due to the complexities of the wave propagation on shore and wave-structure interaction. In this thesis, the research works focus on the investigation of the flow characteristics of tsunami surges around inland bridges and tsunami pressures and forces on bridges. Stand-alone piers and complete pier-deck bridge models which are proportionally scaled from a typical I-girder bridge prototype were employed experimentally. Five configurations of bridge decks with and without perforations in girders and/or parapets were considered. The experimental results reveal that the surge forces on the piers measured from a complete pier-deck model are substantially higher than those measured from the stand-alone piers model. This indicates that the customary method of computing the surge forces on the pier independently for simplicity under the current practice needs to be reviewed for the case of the tsunami-pier-deck interaction. In addition, bridges with perforation in the girders and/or parapets, which have not yet been studied in research for tsunami hazard mitigation, show reduction of forces and less energy input into the structure throughout the time-history.

A numerical model in accordance with the physical model was next constructed in a computational fluid dynamics (CFD) program and verified using the recorded experimental data. The validated model was then extended to simulate bridge prototypes of seven different deck clearances subjected to the most severe wave scenario. The issue of simplification in bridge deck is addressed. The utilization of a complete pier-deck bridge model for a realistic representation is supported by the numerical results. With the piers excluded or simplification of an I-girder deck to a box girder deck, the maximum horizontal and vertical uplift forces on the deck at the initial wave impingement are significantly underestimated by about 15 % and 60% from those predicted for the actual configuration, respectively.

Finally, an empirical method to estimate tsunami forces on bridge decks was proposed. Tsunami forces on bridge decks are categorized into four main components, i.e. horizontal peak, horizontal slowly-varying, vertical uplift and additional gravity forces. Pressure distribution of the horizontal slowly-varying force on bridge deck is established and three other force components are computed as some multiples of the mean slowly-varying force component.

ACKNOWLEDGEMENTS

CONTENTS

List of Tables

List of Figures

Abbreviations and Notations

Abbreviations

2D	Two-Dimensional
3D	Three-Dimensional
CFD	Computational Fluid Dynamics
CPU	Central Processing Unit
FAVOR	Fractional Area / Volume Obstacle Representation
RANS	Reynolds Averaged Navier-Stokes
VOF	Volume of Fluid

Notations

A_r	Area scale
A_x	Fractional areas open to flow in x-direction
A_y	Fractional areas open to flow in y-direction
A_z	Fractional areas open to flow in z-direction
C_d	Drag coefficient
f_i	Viscous acceleration in i-direction
F	Force
F_{bridge}	Force on the entire bridge
F_{deck}	Force on the bridge deck
$F_{deck,m}$	Force on the bridge deck in the model
$F_{deck,p}$	Force on the bridge deck in the prototype
F_f	Friction force
F_{max}	Maximum force
F_{pier}	Force on the bridge pier
F_r	Force scale
Fr	Froude number
F_{sv}	Slowly-varying force
F_{v+}	Maximum uplift force
F_{v-}	Maximum additional gravity force

g	Gravitational acceleration
g_i	Body acceleration in the i-direction
Gi	Girder i
GX+PY	Girders with X % perforations and parapets with Y % perforations
H	Nominal wave height
h_{max}	Maximum wave height (from the ground to the crest)
$h*$	Deck clearance
$h*/H$	Ratio of deck clearance to the wave height
L	Length dimension
P_i	Pressure gauge i
$P_{i,b}$	Back face pressure of pressure gauge i
$P_{i,f}$	Front face pressure of pressure gauge i
P_r	Pressure scale
p	Pressure
Q_r	Flow scale
T_r	Time scale
t	Time
u	Velocity in x-direction
V_F	Volume fraction of fluid
V_r	Volume scale
V_r	Velocity scale
v	Velocity in y-direction
W	Self weight
w	Velocity in z-direction
z	Height from the datum (bed or ground)

Greek letters

ρ	Fluid density

CHAPTER I

INTRODUCTION

Tsunamis are destructive waves which comprise a series of long waves with several hundred kilometers in wave length and several hundreds to a thousand kilometers per hour in flow velocity. They are generally generated in a body of water by an impulsive disturbance of the seabed that vertically displaces the water column. They differ from other water waves caused by winds, hurricanes, storms and floods because they propagate at very high speeds and travel great and transoceanic distances with very little energy losses. When tsunamis approach a shore, their tremendous amount of energy remains nearly constant, thus, induce huge forces. The high inundation level and the fast-moving water of tsunami flow cause catastrophe to coastal structures and loss of lives.

The occurrence of the unprecedented 2004 Indian Ocean tsunami caused severe fatalities and heavy damage to structures including bridges. The enormous force exerted by the tsunami was once again witnessed. Among other incidents, the tsunami floated a 10-MW barge-mounted diesel station 3 km inland in Banda Aceh (Scawthorn et al., 2006), shifted a heavy dredger onto the wharves in Sri Lanka (Ballantyne, 2006) and drifted a police patrol boat 1.2 km inland in Thailand. This disastrous event has attracted the attention of scientists and engineers to accurately estimate wave forces on bridges imposed by tsunamis so that the effective mitigation measures can be formulated.

1.1 Research Background and Motivations

The post-tsunami surveys have evidently demonstrated the damage of bridges in Sumatra, Sri Lanka, India and Thailand during the 2004 tsunami event (Kusakabe et al., 2005; Unjoh, 2005; Iemura et al., 2005; Ballantyne, 2006; Maheshwari et al., 2006; Scawthorn et al., 2006; Sheth et al., 2006; Lukkunaprasit and Ruangrassamee, 2008). Bridges subjected to tsunamis suffered failure through a total or partial wash-away of bridge decks from their abutments, for examples bridges connecting Banda Aceh and Meulaboh (Figures 1.1a and 1.1b), Melamalakudi Bridge in India (Figure 1.1c) and Arugam Bay Bridge in Sri Lanka (Figure 1.1d). The failure of bridges disrupts the commutation of the community; nevertheless, the great concern of the failure is its consequence on the possibility of hampering the emergency relief efforts that are needed

immediately after a disastrous event, as had been observed in Banda Aceh during the 2004 event (Ghobarah et al., 2006).

(a) Banda Aceh (Unjoh, 2005)   (b) Banda Aceh (Yim, 2005)

(c) India (Sheth et al., 2006)   (d) Sri Lanka (Ballantyne, 2006)

Figure 1.1 Partial to total damage of bridges during the 2004 Indian Ocean Tsunami

Tsunami-induced forces on bridges are not well understood due to the paucity of studies on tsunami impact on bridges. Because of the complexity of the wave propagation on shore and wave-structure interaction, theoretical approach for the determination of tsunami-induced forces cannot be easily applied for a complete bridge structure with today's state-of-the-art. Therefore, the first part of this research was carried out to experimentally study the flow characteristics of tsunami around the complete pier-deck bridges and to estimate tsunami forces on bridges. Physical model tests were conducted in a wave flume to investigate the actions of tsunamis on a stand-alone piers and a complete pier-deck bridge models. The 1/100 bridge models were downscaled based on a typical inland highway bridges in Thailand with solid I-beam girders and parapets configurations.

The experimental study was further extended to explore the tsunami loading on four other types of bridges with perforated girders and/or parapets.

Experimental studies provide a realistic representation on the physical mechanics of the wave flow; however, various constraints were encountered: (a) the real phenomena of wave attack on bridge model might not be well represented in such a small scale model, (b) detailed measurement of wave pressure at the relatively small scale model could not be realized even though miniature instruments were used, (c) the force exerted on the bridge deck of the complete pier-deck rigid model could not be determined by simply subtracting the total force that acts on the stand-alone piers model from the one measured in the complete pier-deck model, and (d) vertical forces could not be obtained from the physical modeling due to the limitation of the instrumentation.

To overcome the above-mentioned drawbacks from the experiment, numerical simulations were performed in this study as the subsequent approach to enhance the findings from the hydraulic modeling. These analyses were carried out using the state-of-the-art computational fluid dynamics program which adopts a finite-difference method in the Eulerian hydrodynamic code. A complete pier-deck bridge model which has similar setup in the experimental study was constructed and the calculation results were validated using the recorded experimental data. The analyses were then extended to simulate tsunami flow around the actual bridge prototype to eliminate the scale effect and in turn provide convincing results.

The work presented in this dissertation focuses on the experimental and numerical analyses of inland I-beam girder bridges subjected to tsunamis. A complete pier-deck configuration with proportionally scaled piers and decks are employed. Tsunami loading on a bridge deck with perforated girders and parapets, which appear to be the first study to the author's best knowledge, is investigated. Findings on tsunami forces on bridge pier and deck are beneficial to bridge designers in gaining insights into the estimation of tsunami-induced forces on bridges. The contribution is therefore towards the thorough understanding on the behaviour of inland bridges subjected to tsunamis.

1.2 Research Objectives

The main goal of this research is to investigate the flow characteristics of tsunami flow around bridges and to estimate tsunami forces on bridges experimentally and numerically. The mitigation measures for bridges with perforated decks against tsunami attacks are studied and the effects of the simplification of complex bridge configuration are assessed. The specific objectives of this study are:

i)   To experimentally simulate tsunami flows attacking bridge models and record the forces and pressures on the bridge models with various configurations in terms of perforation areas in bridge girders and parapets.

ii) To numerically reproduce the experimental tests on bridge model configuration without perforations using a validated computation model and simulate the wave flow around bridge prototypes with various configurations in terms of deck clearances.

iii) To assess the reduction of forces on bridges with solid and perforated decks subjected to tsunamis.

1.3 Scopes of Research

The scopes of this study are limited to the following:

i)   A smooth rigid bed with mild slope (1/115) representing Kamala beach profile in Phuket was considered.

ii) The bridge model is placed on a dry bed and subjected to tsunamis in the form known as surges (not bores), striking in right normal to the bridge longitudinal axis.

iii) Due to constraints in the availability of the testing facility, the bridge models were investigated for two nominal wave heights only, viz., 65 mm and 80 mm. Perforated bridge deck models are limited to four different configurations.

iv) The target bridge consisted of an I-beam girder deck with a single column bent in a rectangular shape.

v)   Numerical analysis focuses on bridge prototypes without perforations subjected to 8 m nominal wave height only. Simulations of three simplified bridge configurations are conducted in the numerical analysis.

1.4 Contributions of Research

The significant contributions of this research are as follows,

1) It provides an insight into the tsunami flow characteristics around a realistic inland bridge model that consists of a complete pier-deck bridge configuration as the first ever study.

2) It reveals the importance of employing a complete pier-deck model to estimate the surge force on the bridge pier with limited deck height which obstructs the flow.

3) An expression for estimating the horizontal slowly-varying forces is derived and an empirical method for estimating the peak horizontal, vertical uplift and additional gravity forces is proposed.

4) The effect of perforations in bridge girders and/or parapets for mitigating tsunami forces on bridges which has not yet been investigated in research is evaluated.

1.5 Outline of Dissertation

This dissertation documents the research work into six chapters. Research background, motivations and objectives are presented in Chapter I. Chapter II reviews the literatures and findings of tsunami acting on vertical wall-type structures and bridges in both the experimental and numerical studies. Chapters III and IV outline the methodology and procedure, as well as the recorded or computed results in the experimental and numerical modeling, respectively. Significant findings and contributions to tsunami force estimation on bridge deck are discussed in Chapter V. Finally the conclusions of this research work are drawn and future recommendations are suggested in Chapter VI. A list of references and appendices are attached in the final part of this dissertation.

CHAPTER II

LITERATURE REVIEW

The main focus of this study concentrates on the assessment of tsunami forces on inland bridges whose development is still in its infancy. Several design guidelines to estimate tsunami forces on vertical wall-type offshore structures such as seawall, breakwater and dikes have been proposed. In these cases, the structures stand from the base with no lateral variation in their exposed surfaces to the wave attack. Thus, the maximum impulsive force occurs at the leading wave front during the initial wave attack, which is coincident with the maximum flow velocity. However, I-beam girder bridges with complex configurations exhibit distinct behaviour than those aforementioned structures with uniform frontal area under the action of tsunamis. The flow wave front of tsunami strikes the bridge piers at initial wave impingement on bridges and then splashes upward with subsequent increase in the flow depth. The flow around the bridge deck is obstructed by the cross beam, girders and parapets which are protruded from the girders.

Comprehensive studies have been conducted experimentally to investigate tsunami actions on coastal structures due to breaking and non-breaking waves. Because of the paucity of study on inland bridges subjected to broken wave, selected literatures on experimental studies on vertical wall-type structures subjected to tsunami bores and surges, which are closely related to the current study, are briefly discussed in the earlier section. It is followed by the recent works on bridges subjected to coastal storms and tsunamis. Related studies to the perforated bridge deck are explained in the last section.

2.1 Tsunami Bores and Surges

Tsunami bores and surges are the broken waves with long wave lengths. When tsunami propagates in run-up zone where the water depth keeps decreasing towards on shore, the wave increases in its height and breaks when it loses its stability. The wave breaks in a plunging mode and it is known as bores when the over-turned tip of the wave touches down on the water surface (Yeh, 2007). Therefore, bores contain a large quantity of air entrapment in the wave front. After that, tsunami bores propagate on dry ground and it is known as a surge as described in Camfield (1994) and Yeh (2007). Based on the experiments by Cross (1967) and Ramsden (1996) in which bores and surges of similar

strengths were generated, the characteristics of bores and surges and their effect on a vertical wall are shown as follows:

- Bores have relatively steep wave front than surges;
- Wave height behind the bore front is higher than the one of the surge, and
- An overshoot in force at the initial wave impingement on a vertical wall with a factor of 1.5 as compared to the subsequent quasi-steady force is measured for tsunami bores while there is no such overshoot observed in tsunami surges (Ramsden, 1996).

2.2 Issues on Bridge Deck Failure Mechanisms

Various phenomena observed during the post-disaster have improved the understanding of the bridge behavior under the wave attack. Unjoh (2005) reported that bridges in Banda Aceh that survived during the 2004 Indian Ocean tsunami are those equipped with shear key, uplift stopper or stiff connection between the deck and substructure. Iemura et al. (2005) surveyed three coastal bridges damaged in Banda Aceh. Their decks were displaced non-uniformly in the direction of tsunami flow. Iemura et al. (2005) claimed that the decks were not washed away due to the interlocking of the decks from this non-uniform deck movement.

The topography is also an important cause of bridge failure. Okada et al. (2005) postulated the failure mechanism of Omori Bridge, Hokkaido, Japan by Typhoon Songda. The bridge was located along a cliff. Based on their experimental simulation, it is believed that the incident wave collided with the reflected wave from the cliff just below the bridge deck. Both horizontal and vertical forces exerted on the deck, damaged the bearing and caused four spans of girder deck to fall from their piers, consistent with the actual damage.

The incident of the Hurricane Katrina in 2005 provides an understanding of air entrainment under the deck to the damage of bridge decks. The Interstate 10 (I-10) twin span bridge suffered severe damage while two nearby bridges sustained minor damage during the same storm surge attack. Two low approaches of the bridge which consisted of simply supported precast concrete spans completely or partially fell into the water or experienced excessive lateral displacement. A simple hydrostatic analysis was conducted in the laboratory to investigate the effect of air trapped beneath the damaged bridge deck as reported in Farris et al. (2007). The deck was simplified as a rectangular hollow box

with the opening at the bottom side. The result revealed that when the ratio of the volume of trapped air in a hollow box to the volume of the corresponding solid rectangular box reached a value of 55 %, the effective gravity load of the box became zero, and the concrete box floated on the surface of the water. Under this condition, even a small horizontal disturbance caused by drag force, wave action, or wind could relatively easily move the bridge deck laterally. The floatation of the deck was found to be the main cause of the displacement of the deck, which is justified with supporting evidences.

2.3 Review on Prediction Formulae for Wave Forces on Bridge Decks

Following the occurrences of Hurricane Ivan in September 2004 and Hurricane Katrina in December 2005 which badly hit and damaged highway bridges in the United States (US), researchers in US in particular carried out extensive studies on wave forces on bridges (Douglass et al., 2006; Modjeski & Masters, 2007; Schumacher et al., 2008; Cuomo et al., 2009). Up to the current stage of this study, several empirical prediction formulae have been proposed for the force estimation on bridge decks due to the coastal waves based on the modified or extended methods by Kaplan's equation (Modjeski & Masters, 2007) and McConnell's equation (Douglass et al., 2006; Cuomo et al., 2009). However, wave forces due to tsunamis are not considered in the above-mentioned studies.

The proposed prediction formulae by Modjeski & Masters (2007) are complicated involving numerous empirical coefficients. As opposed to the extended Kaplan's equations, the modified McConnell's equations are much more simple. The fundamental principle behind the McConnell's approach is to define the wave forces as some proportions of the fundamental forces acting on the vertical plane of the deck. The reference forces in the horizontal and vertical components which are 'apparent hydrostatic forces' are first determined. The maximum impact loads corresponding to those components are then computed as some multiples of their reference forces. The number of girders supporting the bridge deck is taken into account in the horizontal load multiplier. The proposed prediction formulae by Douglass et al. (2006) for estimating the forces on bridge decks subjected to storm waves have been adopted as the interim guidance in the Federal Highway Administrative Hydraulic Engineering Circular No. 25 (HEC-25) (Douglass and Krolak, 2008). Cuomo et al. (2009) further modified the McConnell's method for bridge deck subjected to coastal waves and expressed the multiplier in a polynomial function based on extensive experimental data.

2.4 Experiments of Tsunami Loading on Vertical Wall-Type Structures

Physical modeling has been adopted extensively for the investigation of the effects of tsunamis on maritime structures in the laboratory using wave flumes. Various scales of the experimental setup for tsunami forces on vertical wall-type coastal structures such as sea walls, breakwaters, land structures and other tsunami protection structures have been studied over the past few decades. Fukui et al. (1963), Cross (1967), Togashi (1986), Ramsden (1996), Asakura et al. (2000), Ikeno and Tanaka (2003), and Arikawa et al. (2005) simulated tsunami bores advancing over a dry bed and striking onshore structures, while Tanimoto et al. (1984), Ramsden and Raichlen (1990), Ramsden (1996), Hamzah et al. (2000), Mizutani and Imamura (2000) and Ikeno et al. (2001) investigated the effect of tsunami bores on structures partially submerged in a certain depth of still-water.

The well known formulation proposed by Goda (1973) has been used for estimating wave forces on breakwater. Even though this formulation is derived for coastal waves (standing wave, breaking wave or post-breaking wave), due to its applicability for long period wave, it is adopted for tsunami force estimation. Above the sea water level, Goda's formula predicts the maximum surge height of 1.5 times the maximum wave height and the maximum pressure of 1.1 times the hydrostatic pressure at the sea water level based on the maximum wave height, which is defined as the elevation between the wave crest and the wave trough.

Research on tsunami action on the dike with various slopes was studied by Fukui et al. (1963). They categorized the bore pressure acting on the dike with various slopes into two types, i.e. impulsive and continuous pressures. Impulsive pressure is obtained when the bore first surges up the dike while continuous pressure is attained when the reflected bore collides with the incident bore and the standing wave in front of the dike exerts certain hydrostatic pressure on the dike. For a vertical wall, the vertical distributions proposed for impulsive and continuous pressures by Fukui et al. (1963) mark the maximum run-up height of 3.4 and 1.33 times the incident wave height and 4.5 and 1 times the hydrostatic pressure at the base of the wall, respectively.

Tsunami bores and surges on a vertical wall were investigated by Togashi (1986) and Ramsden (1996). Both studies found that the hydrodynamic forces on the vertical wall are less than the one predicted from the hydrostatic forces based on the measured run-up heights on the wall. Togashi (1986) calculated the hydrodynamic force which

mainly consists of drag force by using the averaged velocity over the heights in front of the wall. The drag force due to the reflected bores is found to be 10 % to 40 % of the hydrostatic force based on the measured wave height in front of the wall. Similar trend is also recorded in the experimental results of Ramsden (1996): the maximum forces due to the reflected bores, surge and non-breaking wave measured from the experiments are smaller than those determined as the hydrostatic forces based on the maximum recorded run-up heights on the wall. Cross (1967) proposed a formulation to estimate the surge forces on a vertical wall while the impact forces on a vertical wall due to tsunami bores were recommended in Ramsden (1996). Experimental simulations on a vertical wall partially submerged (1/5 of the wall height) in the still-water subjected to tsunami bores were conducted by Hamzah et al. (2000). The wall was center-spanned across 0.4 of the width of the flume. Two types of pressure peaks corresponding to the maximum impulsive pressure and standing wave pressure were observed. The experimental results were supported by the computational results based on the Navier-Stokes equations incorporating the Volume of Fluid (VOF) method.

Tanimoto et al. (1984) recommended wave pressure distributions on a vertical breakwater based on the experimental results using a sine wave. The linear pressure distribution with a maximum pressure of 2.2 times the hydrostatic pressure at the still-water level based on the height of tsunami body (not the maximum of the wave front) and decreasing to zero at the maximum surge height of 3 times the wave height from the still-water level was proposed. A uniform pressure of 2.2 times the hydrostatic pressure is extended to the base of breakwater which is submerged in the water.

The formulation was then improved by Ikeno et al. (2001) and Ikeno and Tanaka (2003) for offshore and onshore vertical walls subjected to tsunami bores and surges, respectively. For offshore wall, larger pressure of 3 times the hydrostatic pressure at the still-water level is exerted on the wall and decreases linearly to 2.2 times the hydrostatic pressure at a distance of 0.5 times the wave height below the still-water level. For onshore wall, the pressure distribution in Ikeno et al. (2001) is further improved for a distance between 0.5 times the wave height above and below the still-water level where the maximum pressure of 4 times the hydrostatic pressure occurred at the still-water level. The formulation of tsunami forces on offshore prevention structures such as seawalls and breakwaters was also studied by Mizutani and Imamura (2000, 2002).

Tsunami forces on land structures were investigated by Asakura et al. (2000) and the findings have been adopted in the design of land structures as stipulated in various

design guidelines. The experiments were carried out in both the wave flume and wave basin. Short and long period waves were generated using piston- and pump-type wave makers, respectively. The land structure was placed on a dry bed. Two kinds of waves were recorded, i.e. waves with and without split waves of shorter period in the wave front. Two different dimensionless pressure distributions were then proposed. For the case without short period waves riding on the wave front, a linear relationship with the maximum pressure of 3 times the hydrostatic pressure at the base and zero at the run-up height on the structure of 3 times the maximum run-up flow depth was proposed. For the case with short period waves in the wave front, the short period waves increase the pressure during the first impact at the lower part of the structure. The maximum pressure of 5.4 times the hydrostatic pressure is attained at the base and it decreases to 2.2 times the hydrostatic pressure at 0.8 times the run-up height while the remaining portion of the pressure distribution is the same as the one proposed for the wave without split short period waves. These formulations are based on the flow at the maximum depth with Froude number of 1.6. The authors reported that the estimated forces from the proposed maximum pressure profile are nearly 20 % higher than the recorded maximum wave forces.

Tsunami forces on land structures were also extensively investigated by Arikawa et al. (2005, 2006, 2007, 2008). Standing wave pressure on land structures was further investigated and it could be adequately predicted by Asakura's formula, the impulsive pressure was nearly 9 times the hydrostatic pressure based on the wave height in front of the land structure (Arikawa et al., 2006). The behaviour of the concrete wall subjected to tsunamis was also studied by Arikawa et al. (2007, 2008).

2.5 Experimental Studies on Bridges Subjected to Tsunamis

Interestingly, experimental studies of tsunami forces on bridges have only been conducted recently by Kataoka et al. (2006), Shoji and Mori (2006), Iemura et al. (2007), Sugimoto et al. (2008) and Moriyama et al. (2008). All these studies employed rigid bed models. Out of these researches, only Iemura's study placed the bridge model on a dry bed whereas bridge models in the other studies were placed in certain depths of still-water. Single span bridge models were installed on abutments across the width of the water channel in small to medium scale wave flumes for all the studies except Kataoka's work

in which three spans of bridge decks were installed in a large scale wave flume. Various model scales from 1/18 to 1/108 were adopted.

Kataoka et al. (2006) measured the impulsive forces followed by the drag forces on the bridge due to tsunami attacks under various combinations of wave heights and still-water depths, thus, simulated non-breaking, breaking and broken (bores) waves. An inverted box (with opening at the bottom face) was employed. They found that the impulsive forces much depended on the wave breaking conditions; thus, the impulsive forces could not be represented in any simple formulation. On the other hand, the drag forces on the bridge deck, averaged over a 0.5 sec duration, were found to agree quite well with wave height-dependent formula (Goda's formula) stipulated by the Technical Standards and Commentaries of Port and Harbour Facilities of the Japan Port and Harbor Association (JPHA, 1999) with some safety margin. The amplitude of solitary wave was used as the wave height in this case. Moreover, drag forces were independent of the still-water depth. By increasing the width of the deck, smaller peak horizontal forces but larger peak vertical forces were observed. The former phenomenon may be attributed to the longer time lag for forces acting on both the front and back girders, which is identical with the variation of the drag coefficient (C_d) of steel girder bridge deck subjected to wind loading in the guidelines of the Japan Rail Association (JRA, 2002). The latter phenomenon can be explained by the increase of the horizontal projection area exposed to vertical force attack.

Iemura et al. (2007) simulated the damaged Ulee Lheue Bridge in Banda Aceh by tsunami with the estimated height of 12 m. They measured the maximum forces at the first attack of tsunamis on the bridge model, which practically occurred at the same time with the peak flow velocities. They found that the maximum forces could be predicted by the standard drag formula with a C_d of 1.1, based on the averaged peak flow velocities at free flow condition. This value is far lower than the suggested C_d of 2.0 to 2.2 in the Hydraulic Engineering Circular No. 18 by the Federal Highway Administration (Richardson and Davis, 2001).

Shoji and Mori (2006) reproduced the bridge failure mechanism following the site observation in Sri Lanka in physical model tests. In the earlier study, simplified box shape girder decks were placed on the abutments. No pressure or force measurements were made. The failure of the deck was defined to occur when the hydrodynamic force of the wave exceeded the lateral resistant force due to friction. C_d of 2.0 was assumed while the static friction coefficient was determined from the experiments. The correlations between

the flow velocity with flow depth and deck aspect ratio for damaged and survived bridge decks were established. Force measurements were made later in the study by Moriyama et al. (2008) in which downscaled girder decks were employed. The relations for the non-dimensional lateral forces and tsunami wave heights were studied. The drag coefficients for girder decks ranging from 0.85 to 1.34 were back calculated from the standard drag formula.

Sugimoto and Unjoh (2008) modeled two damaged bridges near Banda Aceh: Lueng Ie Bridge and Kr. Cuntuem Bridge. They measured horizontal and vertical forces on rigid bridge decks while the movements of movable bridge decks were also performed. Bridge decks were located at various still-water depths and subjected to 3 m to 6 m depths of tsunamis. The maximum horizontal impulsive forces (drag forces) were compared with the calculated values based on the standard drag formula, using the drag coefficient from JPHA (1999) and the average velocity computed from two wave gauge readings (Sugimoto et al., 2008). The results show that the measured impulsive forces were about 34 % higher than those calculated from the formula. The relationships of the deck failure modes with wave heights, still-water depths and forces were studied.

The results of the above studies do not conclude tsunami forces on bridges. Furthermore, in Kataoka's and Iemura's studies, the bridge piers were constructed as thin as possible in the tests (personal communications with the authors). It is important to observe that, by omitting the piers or making their sizes un-proportionally small in the physical models, they essentially ignore the influence of the piers and deck on the flow condition around each individual component. Therefore, a more realistic model was employed in this research which included both the piers and decks in the actual proportion. Comprehensive and detailed studies on tsunami flow around bridges are vital and need to be explored promptly.

2.6 Numerical Studies of Tsunami Forces on Bridges

Various two- and three-dimensional numerical models had been developed to predict the generation and propagation of tsunami and storm surge in the past. However, the prediction of the terminal effect of tsunami on structures such as bridges is a challenging task due to the complexity of the wave propagation and the fluid-structure interaction. Yim (2005) discussed the development of coupled fluid-structure interaction model for estimating the tsunami and storm surge effects on bridge structures. The

comprehensive fully-coupled fluid-structure interaction model could be divided into wave and structure domains which can be enforced by coupling them via the compatibility and equilibrium criteria at the multi-physics interface using an iterative process.

Numerical studies on bridges subjected to tsunamis were carried out by Nimmala et al. (2006), Endoh and Unjoh (2006) and Ikari and Gotoh (2007). Nimmala's work focused on the determination of the design tsunami force on a real bridge in Oregon, U.S. under the predicted tsunami scenarios from the fault models. A two-dimensional bridge deck model (simplified as a rectangular box with top rounded edges) was considered. The fluid-structure interaction analysis of the bridge was conducted using the state-of-the-art computational mechanics software. Endoh and Unjoh (2006) and Ikari and Gotoh (2007) used the particle method where the motion of the fluid is described in a Lagrangian coordinate. The former study used the Particle Flow Code to simulate an I-girder bridge in a two-dimensional model. The target bridge was located over a dry bed in Banda Aceh, subjected to 30 m high tsunami and a constant velocity of 68 km/h. The latter study used the Moving Particle Semi-implicit (MPS) method to simulate tsunami flow around a simplified rectangular box girder bridge over a wet bed based on the experimental study by Shoji and Mori (2006). Both studies reproduced the failure mechanism of bridges subjected to tsunami attacks.

2.7 Perforations in Bridge Girders and Parapets

Unlike the investigation of the openings in the slab of bridges as described in Cuomo et al. (2009), the use of perforations in bridge girders and parapets for the purpose of tsunami-force mitigation is the first-of-its-kind. The idea of introducing perforations in girders and parapets of bridge deck was initiated based on the observation that buildings with openings in the masonry infill panels suffered less damage during the 2004 tsunami event (Lukkunaprasit and Ruangrassamee, 2008). This approach is similar to the application of girders with openings in the construction industry for facilitating installation of service utilities. From the findings of the studies by Chung and Lawson (2001), Chung et al. (2001), Liu and Chung (2003), Chung et al. (2003) and Lawson et al. (2006), it is possible to employ large openings in steel girders with minimum effects on the shear and the bending resistance of the girders, provided careful sizing and positioning of the openings or special reinforcement around the openings are taken into consideration. An example of the application of perforated girder is shown in Figure 2.1.

Figure 2.1 Girders with perforations in various sizes and shapes (Lawson et al., 2006)

CHAPTER III

EXPERIMENTAL STUDY

This chapter describes the experimental modeling that was conducted in a wave flume at the Hydraulic Laboratory, Asian Institute of Technology, Thailand. Experimental procedure and setup are first described in this chapter. Two types of bridge models, i.e. a complete pier-deck model and a stand-alone piers model are presented. It is then followed by the detailed explanation for measuring instrumentation and calibration. Recorded results from the experimental tests are presented at the end of this chapter.

3.1 Experimental Procedure

A wave flume experiment was conducted to obtain the time histories of pressures and forces on an inland bridge subjected to tsunami loading. Figure 3.1 presents the outline of the experimental procedure. The model study was first carried out to formulate the experimental setup and to evaluate the scaling criteria. A bridge model was then designed and constructed to represent a bridge prototype. The model was installed in the wave flume and the data were recorded after the calibration of instruments was completed. On-site calibration was performed prior to each test to ascertain all instruments in place were functioning properly. The signals from all the instruments were collected by data loggers. On-site re-calibration was also conducted whenever the exceptional signal was detected during data acquisition. The data were then processed in order to produce the required output in terms of time histories of forces and pressures. The details of the test setup, instrumentation, calibration and execution of the experiment are presented in the following sections.
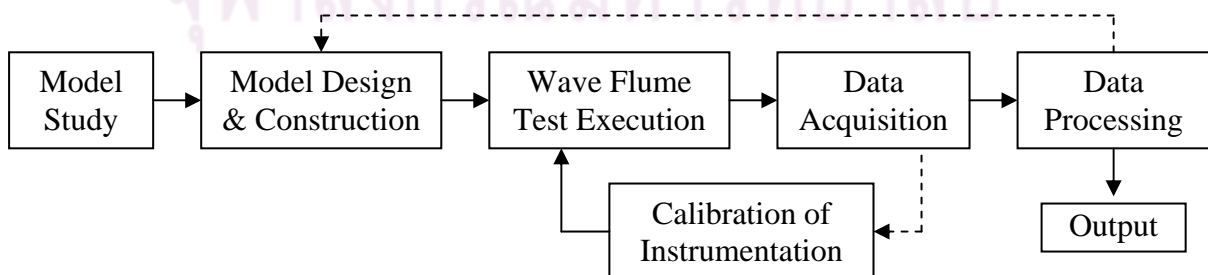
Note: Solid and dotted arrows denote the procedures for routine and special cases, respectively

Figure 3.1 Flow chart of experimental study

3.2 Model-Prototype Relation

The basic principle of the physical modeling is to simulate the characteristics of the prototype by the model which is generally at a reduced scale under certain similitude criterion. In the case of tsunami waves where inertial and gravitational forces are dominant, the Froude number of the model and prototype must be the same (Chanson et al., 2003; Hughes, 2005). Froude number is defined as the square root of the ratio of inertia force to gravity force or weight. Due to the highly turbulent flow that is generated by tsunami around an object, the flow is in the Reynolds number independence regime where the effects of flow viscosity in the model tests could be neglected. With the linear scale of 1/100, the relations between the model and the prototype quantities are summarized in Table 3.1.

Table 3.1   Model-prototype scale relationships

Quantity	Dimension	Scale
Length	L	$L_r = 1:100$
Area	L^2	$A_r = L_r^2 = 1:10,000$
Volume	L^3	$V_r = L_r^3 = 1:1,000,000$
Flow	L^3/T	$Q_r = L_r^{5/2} = 1:100,000$
Time	T	$T_r = L_r^{1/2} = 1:10$
Velocity	L/T	$V_r = L_r/T_r = 1:10$
Force	F	$F_r = L_r^3 = 1:1,000,000$
Pressure	F/L^2	$P_r = L_r = 1:100$

3.3 Experimental Setup

Figure 3.2 illustrates the setup of this experimental study. The hydraulic model experiments were carried out in a wave flume of 1 m × 1m cross section and 40 m length. The rigid bed of the flume was constructed from painted steel plates supported by structural steel sections. A two-dimensional model was applied to represent the Kamala Beach profile in Phuket, Thailand with a compound bed slope of 1/115 (0.5^0) and a flat platform where the model is located. A short steep rise (1/15.6) just before the flat section represented the embankment on the beach. The coastal geometry was downscaled in the model study with the length scale of 1/100.

The water stored in the elevated tank at the farthest right end of the flume in Figure 3.2 was used to generate a tsunami-like solitary wave by a sudden disengagement of the gate through a lever located at the base level of the tank to release the water. Solitary-like waves with different wave heights were generated by varying the amount of released volume of water. The relationship of water volumes and the wave heights at the location of the model (H1) was calibrated prior to the tests of the bridge model in the flume.

Figure 3.3a shows a single solitary wave that was formed at the location near to offshore region (H2). The wave with almost a vertical wave front (Figure 3.3b) broke in the finite depth of still-water as a plunging-type breaker (Figure 3.3c) after losing its stability. The wave then transformed into bore by shoaling a solitary wave at a distance of about 20 m offshore. The turbulent bore runup on shore takes the form of a surge striking the bridge model which is rigidly installed at the downstream end of the flume. The wave then overflowed at the open end (left of Figure 3.2) before entering a pump sump underneath the ground platform.
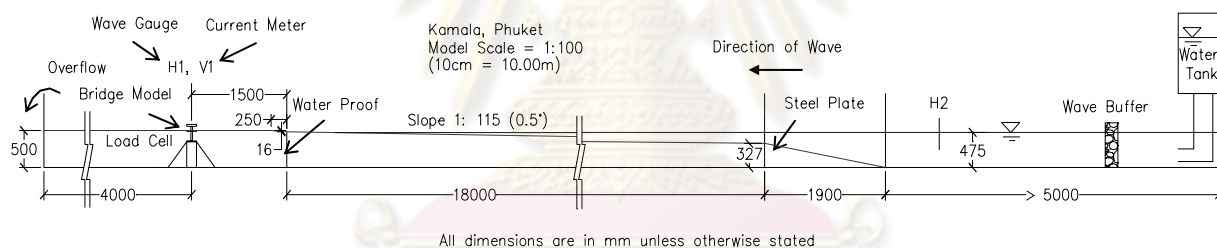
Figure 3.2 Schematic diagram of the experimental setup

Figure 3.3 Simulated tsunami waves and wave breaking

3.4 Target Bridge

The target bridge prototype in this study is a reinforced concrete bridge with I-beam girder which is widely constructed in developing countries around the Indian Ocean. The bridge girders rest on elastomeric bearings, usually made from synthetic or natural rubbers. The bridge, spanning 30 m apart, consists of a deck 13.8 m wide supported by 1.5 m depth girders, and 1 m high parapets. The deck clearance (height from the ground to the girder soffit) is 5.6 m. A ground level of 2.5 m above the mean sea level is considered, reflecting the actual elevation in the southern part of Thailand. The expected tsunami inundation depth at the site is about 6 to 8 m with reference to the ground and the wave hit perpendicularly to the longitudinal axis of the bridge. Since the tsunami force is normally not taken into consideration during the design of inland bridges, these structures are highly vulnerable to damage should a tsunami attack. This may lead to major disaster since bridges are part of lifeline infrastructure which are needed for emergency relief purpose immediately after the event.

3.5 Bridge Models

The 1/100 scaled complete pier-deck bridge model constructed from clear acrylic plates was mounted on a base plate flushes with the surrounding dry bed located downstream which was 25 mm above the still-water level as shown in Figure 3.2. Figures 3.4 and 3.5 illustrate the typical cross-sectional and front views of the bridge models, respectively. The bridge deck has a width to depth ratio or aspect ratio of 5. The bridge girders were numbered in ascending order (G1 to G6) in the direction of flow. The vertical projection area ratio of the deck which included girders and parapets to the piers was about 4.85. Three spans of the bridge deck with each span of 138 mm in width by 300 mm in length were installed across the width of the flume and perpendicular to the flow direction. Out of these three spans, only the middle span was instrumented with pressure gauges and a load cell. It is to be noted that the model included the bridge piers spaced at 137 mm apart. This spacing was intentionally reduced somewhat so as to reduce the size of the base plate supporting the piers. This would practically not affect the test results since the distance between the piers were far apart (about 10 times the width of the pier). The base plate was mounted on a high frequency load cell which was used to record the total horizontal wave forces acting on the complete pier-deck bridge model. Also shown in the figures are the positions of pressure gauges on the model. P_1 designates the

pressure gauge location at the base of the pier while P_2, P_3 and P_4 are those at the mid-span of girders G1, G2 and G3, respectively. The pressure readings were further designated as the front and back face pressures exerting on the girders by the subscripts f and b, respectively.

3.5.1 Solid and Perforated Bridge Deck Models

A solid and four perforated bridge deck models with various perforation ratios in girders and parapets were constructed as given in Table 3.2. They were described thereafter by the notation of GX+PY which denotes the X % perforation area in girders and Y % perforation area in parapets. The bridge deck is solid if X and Y are zeros. The bridge models are G0+P0, G20+P0, G20+P20, G0+P60 and G10+P60. The perforations in girders and parapets were designed in elongated circular and rectangular shapes as displayed in Figure 3.5. These simplified shapes were adopted based on considerations of both practicability in the prototype and feasibility of the model construction.

Table 3.2   Details of perforations

Bridge Model	Perforations in Girders		Perforations in Parapets		Equivalent Area
	(mm^2)	(%)	(mm^2)	(%)	(%)
G0+P0	0	0	0	0	0
G20+P0	900	20	0	0	10.7
G20+P20	900	20	600	20	17.9
G0+P60	0	0	1800	60	21.4
G10+P60	450	10	1800	60	26.8

Note: Frontal area of girder, slab and parapet are 4500 mm^2, 900 mm^2 and 3000 mm^2
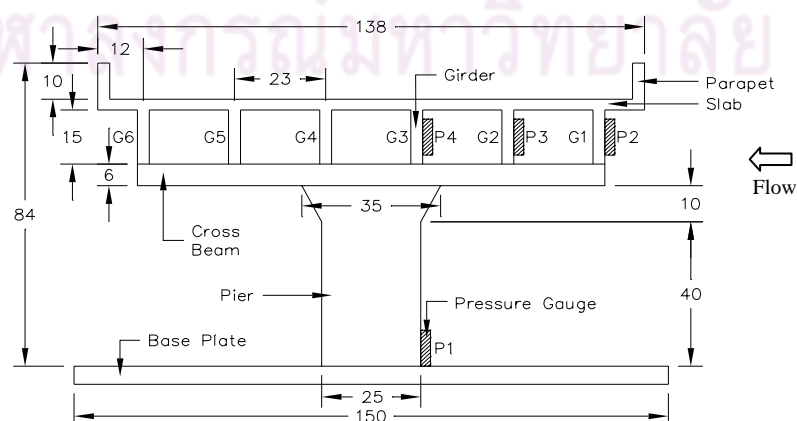
Figure 3.4 Typical cross-sectional view of bridge model (Unit: mm)
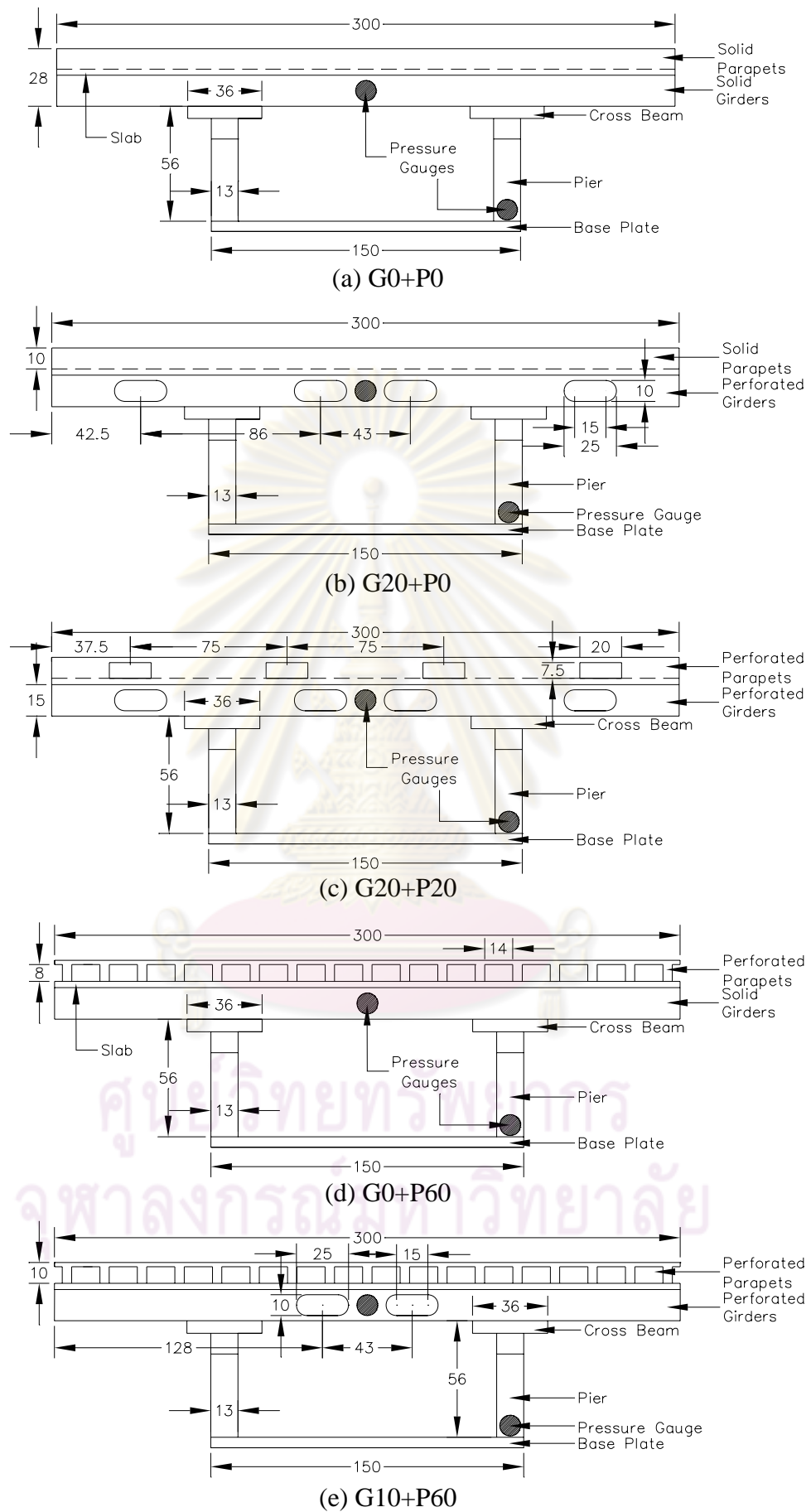
Figure 3.5 Front views of bridge models (Unit: mm)

3.5.2 Stand-Alone Bridge Piers Model

Bridge damage caused by a partial or complete wash-away of the decks from the bridge abutments have been witnessed in the 2004 Indian Ocean Tsunami. An accurate prediction of the tsunami force on the deck is crucial for the structural design of the components of the deck system against such failure. Therefore, experiments were conducted to determine the wave force acting on a model of stand-alone piers without the deck in place as depicted in Figure 3.6. The force time histories on the bridge deck are then determined by excluding the recorded force time histories on the stand-alone piers from the force time-histories on the complete pier-deck bridge model.

(a) Front view   (b) Side view
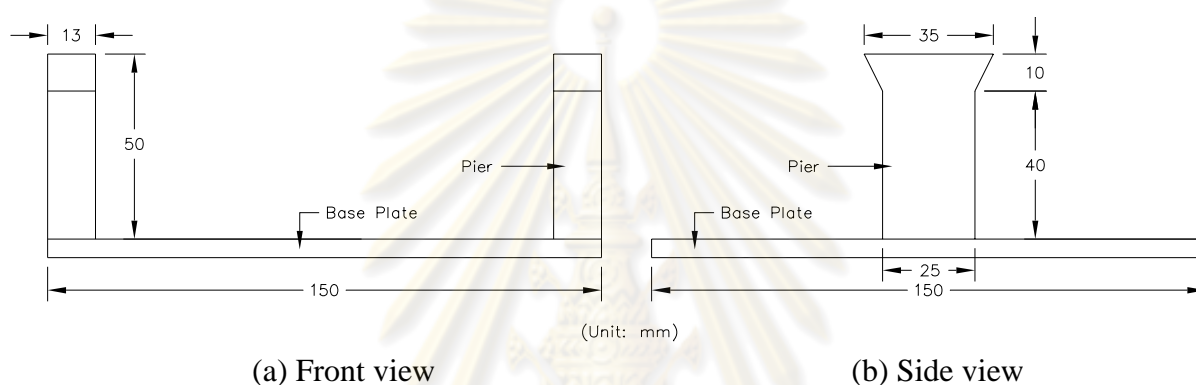
Figure 3.6 Front view and side view of the stand-alone bridge piers model

3.6 Instrumentation

Figure 3.7 shows the schematic diagram of the instrumentation and data acquisition system used in this experiment. DHI Wave Meter (capacitance type wave gauge) and Synthesizer were used to measure the wave profiles at onshore (H1) and offshore (H2) locations as illustrated in Figure 3.2. The velocities of the flow in the flume for various wave heights were recorded by a propeller type current meter at V1 (Figure 3.2). It was connected by the Nixon StreamFlo Digital Indicator and a data logger, Kyowa EDS-400A Compact Recorder. Both wave gauge and current meter were installed at H1 and V1 with the absence of the model during measurement. The wave height and velocity at H1 and V1 were then correlated with the wave height at H2. During the testing of the model, only the wave height at H2 was measured in order to avoid the interference from the instruments on the flow regime in the vicinity of the model. Video and digital cameras were used to capture the wave motion acting on the bridge model.
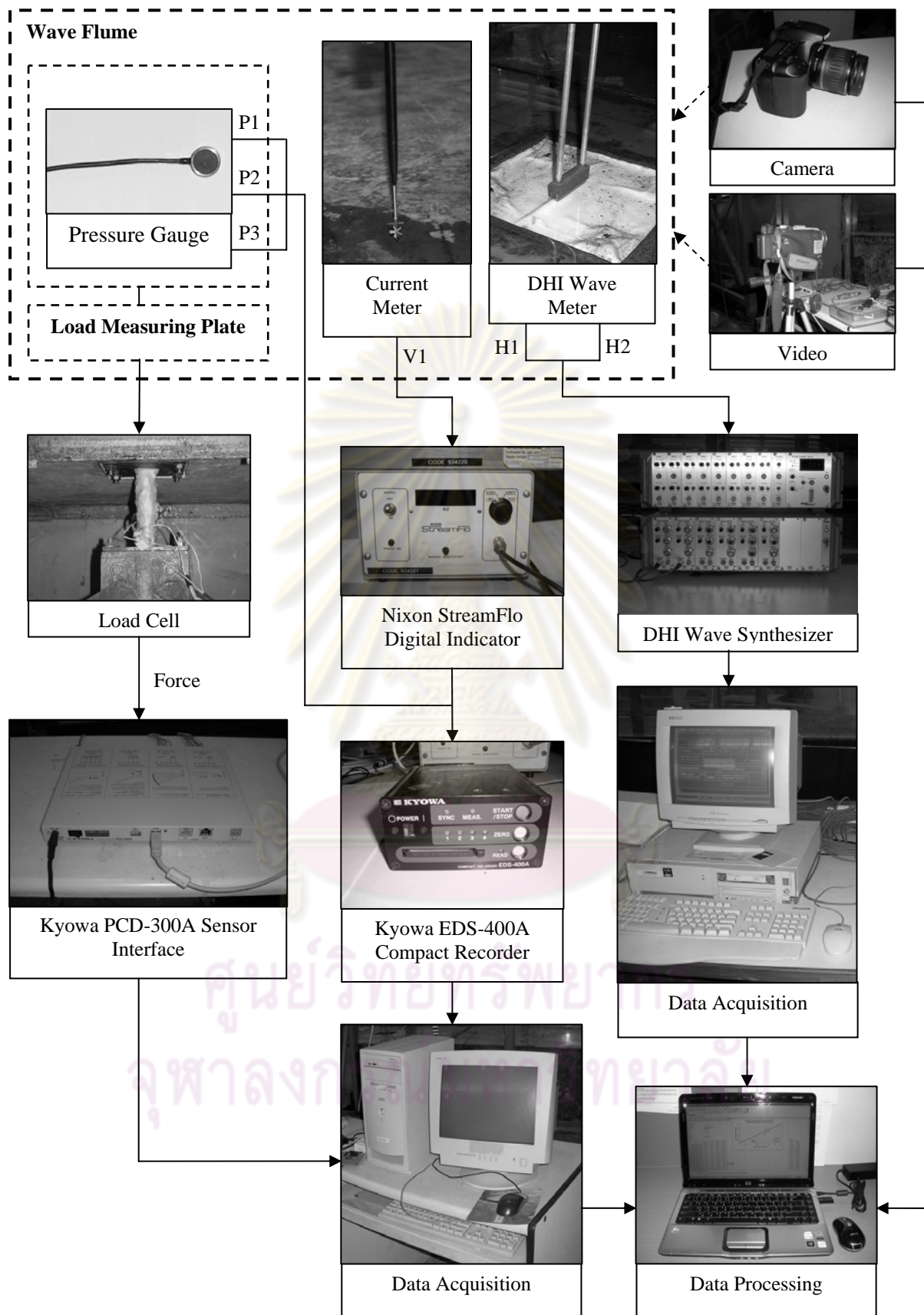
Figure 3.7 Schematic diagram of instrumentation and data acquisition system

Tsunami forces in the horizontal direction were measured by a calibrated high frequency load cell which was mounted at the base of the bridge model. The load cell was calibrated by applying standard weights at various heights from the base of the model using string and a pulley. The recorded value from the load cell represented the total horizontal wave forces acting on the deck and the piers as a result of the wave pressure and the drag. The wave forces that acted on the model were proportionally related to the output voltage signal of the electrical resistance in the Wheatstone bridge circuit. The data were then converted into the required quantities using the calibrated factors.

The wave pressures on the bridge components were measured by means of Sankei water-tight diaphragm type pressure gauges (SSK P310-01 and SSK P310-02) with high frequency response (3.4 kHz and 4.6 kHz, respectively). Each pressure gauge had a circular frontal surface of 10 mm in diameter. The pressure gauges were calibrated by applying a range of hydrostatic pressures in a 0.2 m by 0.2 m in cross-section and 0.6 m high tank. The pressure gauges and load cell were connected to the separated data loggers, Kyowa EDS-400A Compact Recorder and Kyowa PCD-300A Sensor Interface, where the measured physical quantities were collected and stored in the computer. Sampling rates of 500 Hz were applied for both pressure and force measurements in a computerized data acquisition system.

3.7 Calibration

Calibration was carried out to relate the physical quantities measured or received from the instruments to the desired parameter that is needed for the analysis. Calibration for wave height, flow velocity, wave pressure and force are presented in the following sections.

3.7.1 Flow Depth

Flow depth was first calibrated by determining the relationship between the flow depth and voltage of the capacitance wave gauge for two wave gauges (wave gauge No. 1 at H1 and wave gauge No. 2 at H2) used in this experiment. The voltage of the wave gauge at different depth of still-water was recorded as shown in Figure A1 in Appendix A. After obtaining the relationship of flow depth and voltage, the relationship of nominal wave heights, H (defined as the maximum flow depth at the point of interest in the

absence of the model) at locations H1 and H2 was established (Figure A2, Appendix A). Each test was repeated for at least three times.

3.7.2 Velocity

The velocity of flow at the model location was related to the nominal wave height (H1) which was placed at the same location. From the relationship of wave gauges at H1 and H2 described in the previous section, the velocity at the model V1 could be related to the nominal wave height of H2 as illustrated in Figure A3 (Appendix A).

3.7.3 Pressure

Three pressure gauges were used to measure the pressure from the wave. They were placed at various locations, namely P1, P2, P3 and P4, as shown in Figure 3.4. These pressure gauges were calibrated by mounting the pressure gauges in the 150 mm by 150 mm in cross section and 600 mm-high tank. The amplitudes of the pressure gauge at various water depths were recorded. The recorded amplitude was then related to the water depth as shown in Figure A4 (Appendix A).

3.7.4 Force

A high frequency (natural frequency of 106 Hz) load cell that was mounted at the base of the bridge model measured tsunami forces in the horizontal direction. A close-up view of the force measurement device under the bridge model is illustrated in Figure 3.8. It was a strain-gauge type cylindrical tube load cell. The wave force on the bridge model caused changes in strains in the load cell which were measured by the strain gauges attached on opposite sides of the cylindrical tube at two levels. The horizontal shear force was related to the rate of change of the strain readings over the length of the portion instrumented. Prior to the tests, the load cell was calibrated by exerting the standard weights at various heights from the base of the model. In this experiment, the recorded values from the load cell represent the total horizontal wave forces exerted on the deck and the columns as a result of the wave attack on the bridge. The calibration chart for the force is presented in Figure A5 (Appendix A). It was developed by exerting the various forces at different distance measuring from the top of the load cell.
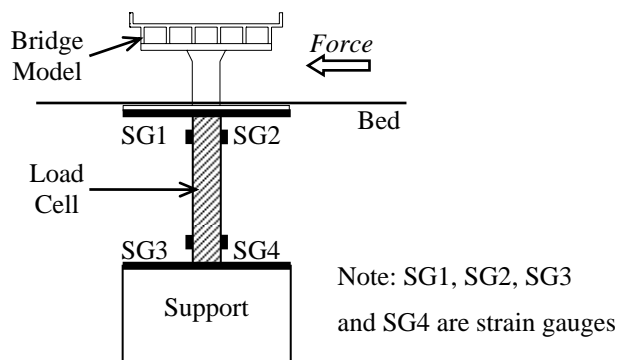
Figure 3.8 Force measurement instrumentation

3.8 Test Program

Two nominal wave heights of 65 mm and 80 mm were performed in the experiment. The nominal wave height is the maximum water level at the location of interest, obtained from the flow in the absence of the bridge model. The two wave heights were selected to describe two severe scenarios of the tsunami attack on bridges. The wave at 65 mm and 80 mm nominal heights were designated to represent a tsunami wave when its crest reached approximately the mid height of bridge girders and when its crest almost overtopped the bridge deck, respectively.

Table 3.3 summarizes the test program of all types of models. A total of five and four test conditions were carried out for G0+P0 and G10+P60 models, respectively, while only one test combination was performed for G20+P0, G20+P20, G0+P60 and stand-alone piers models. Each test condition involved different locations of pressure measurement and it was repeated for at least three times to confirm the repeatability of the experiment.

3.9 Results and Discussion

3.9.1 Relation among Flow Depth, Flow Velocity, Wave Force and Wave Pressures of Solid Bridge Deck (G0+P0)

The typical time histories of the velocity and the height of the wave at the location of the bridge model (in the absence of the model) are depicted in Figure 3.9. In the discussions that follow, the instant when the wave first hits the bridge model is taken as t = 0. It is to be noted that the leading edge of the wave attains a practically maximum velocity at the instant it reaches the location of the bridge model when the wave height is still very small. As the wave increases in height, the velocity decreases significantly, and the maximum wave height is attained at some time later than the instant the velocity is

maximum. Therefore, the peak flow velocity does not coincide with the maximum wave height.

Table 3.3   Summary of test combinations

Cases	Description of Bridge Model	Nominal Height, H (mm)	Total Force	P_1	$P_{2,f}$	$P_{2,b}$	$P_{3,f}$	$P_{3,b}$	$P_{4,f}$	$P_{4,b}$
				Measurement						
			Total Force	Pressure						
SO1_65	G0+P0	65	○		○		○		○	
SO2_65	G0+P0	65	○	○	○	○				
SO3_65	G0+P0	65	○	○			○	○		
SO4_65	G0+P0	65	○	○					○	○
SO5_65	G0+P0	65	○	○						
SO1_80	G0+P0	80	○		○		○		○	
SO2_80	G0+P0	80	○	○	○	○				
SO3_80	G0+P0	80	○	○			○	○		
SO4_80	G0+P0	80	○	○					○	○
SO5_80	G0+P0	80	○	○						
PA1_65	G10+P60	65	○	○	○	○				
PA2_65	G10+P60	65	○	○			○	○		
PA3_65	G10+P60	65	○						○	○
PA4_65	G10+P60	65	○							
PA1_80	G10+P60	80	○	○	○	○				
PA2_80	G10+P60	80	○	○			○	○		
PA3_80	G10+P60	80	○						○	○
PA4_80	G10+P60	80	○							
PB1_65	G20+P0	65	○	○	○	○				
PB1_80	G20+P0	80	○	○	○	○				
PC1_65	G20+P20	65	○	○	○	○				
PC1_80	G20+P20	80	○	○	○	○				
PD1_65	G0+P60	65	○	○	○	○				
PD1_80	G0+P60	80	○	○	○	○				
SA1_65	Stand-alone piers	65	○							
SA1_80	Stand-alone piers	80	○							
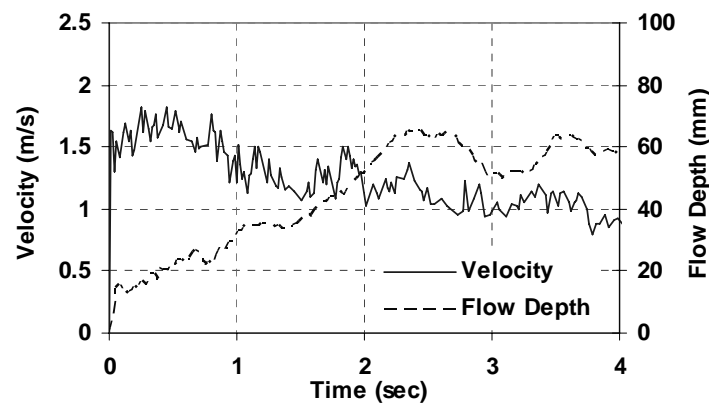
(a) $H = 65$ mm
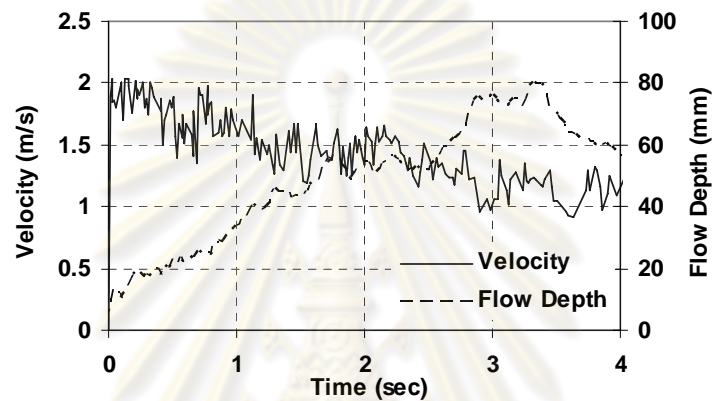
(b) $H = 80$ mm

Figure 3.9 Measured time histories of flow depth (H1) and flow velocity (V1)

The correlation between the flow velocity and the flow depth can be related to the Froude number (*Fr*) of the flow as defined by

$$Fr = v/(gH)^{0.5} \tag{3.1}$$

where *v* is the flow velocity, *g* is the acceleration due to gravity and *H* is the flow depth.

Figure 3.10a presents the correlation between the maximum flow velocity and the nominal wave height in the absence of the model (free flow condition). Both the flow velocity and the wave height shown are the maximum values recorded at different times after the wave attack. The calculated *Fr* of the flow based on the corresponding flow velocity and flow depth is plotted in Figure 3.10b. *Fr* is approximately 7 at the wave front. It decreases to about 2 after one second and then gradually reduces to 1.5 after second 3.
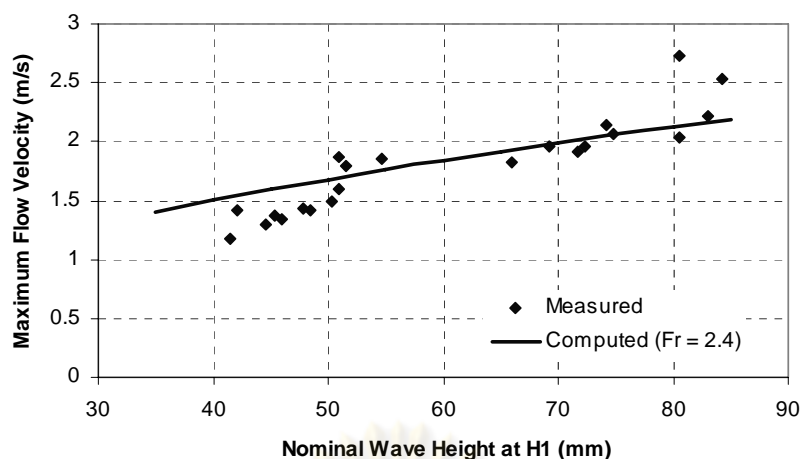
(a) *Fr* calculated based on the maximum flow velocity and flow depth
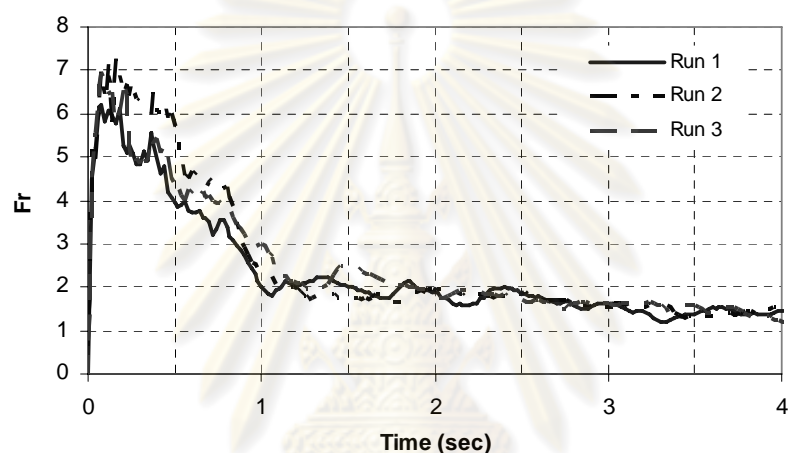
(b) *Fr* calculated based on the corresponding flow velocity and flow depth (*H* = 80 mm)

Figure 3.10 Correlation between flow velocity and flow depth

Figure B1 (Appendix B) illustrates all the recorded force (on bridge deck and pier) and pressure time histories for both nominal wave heights. Even though there are slight variances among those time histories, the overall experimental results show that the forces and pressures which act on the bridge vary in the same trend with good consistency over the time. This indicates that the experiment was conducted in a well-controlled manner and the results are reproducible.

Figures 3.11 and 3.12 present typical time histories of the wave force and wave pressures measured. As the leading edge of the wave strikes the bottom of the bridge piers with a high velocity (Figures 3.13a and 3.14a), part of the upward splash hits the soffit of the cross beams while the remaining splash is diverted sideways. Unfortunately, without prior anticipation of this phenomenon, no pressure gauges were installed on the girders above the pier locations. Nevertheless, it is believed that the shielding effect from the cross beam (which is about three times the width of the pier) would effectively prevent

the upward splash to hit the longitudinal girders sideways. The pressure gauge reading P1 (at the pier) almost instantaneously attains the peak value (about 4.5 times the hydrostatic pressure as shown in Figures 3.11b and 3.12b) while no pressure is recorded at the girders. At this instant, the wave height and the wave force are relatively small, but they increase rapidly with time, and the force records the first peak value of 3.9 N for the nominal wave height of 65 mm at second 0.4 and 5.5 N for the 80 mm wave height at second 0.3 (Figures 3.11a and 3.12a). These forces may be regarded as the peak forces on the piers. Thereafter the wave height increases but the velocity decreases as mentioned earlier with the result of the force being sustained near the peak value for nearly one second.

The pressures on the girders remain zero (except P4 which is most likely due to the minor splash-up) until the height of the wave rises to the lower part of the bridge girders (Figures 3.13b and 3.14b) when the wave splashes over the bridge deck with a height of two times that of the incident wave for the 65 mm nominal wave height and three times for the 80 mm wave height as shown in Figures 3.13d and 3.14c. This results in a rapid increase of wave force and the second peak is attained. The wave forces reach their peaks at second 2.4 and second 1.4 for the 65 mm and 80 mm nominal wave heights, respectively. In the meantime, pressure gauge $P_{2,f}$ (Figures 3.11c and 3.12c) attains its peak value but the pressures at $P_{2,b}$, $P_{3,f}$, $P_{3,b}$, $P_{4,f}$ and $P_{4,b}$ are recorded initially with small negative values consistently in all tests. The value of the second peak force is about three times the first peak value as summarized in Table 3.4. The deflected column of water collapses, falls back on the wave with substantial amount of entrained air. The wave then overtops the bridge deck and travels away from the bridge model (Figures 3.13e - 3.13h and 3.14d – 3.14h).

One may observe from Figures 3.11 and 3.12 that the maximum wave force on the bridge model almost coincides with the occurrence of the peak net pressure at girder G1. Girder G1 is subjected to the highest wave forces compared to the others (girders G2 and G3) because it is exposed to the direct wave attack. The maximum pressures which are 2.0 and 2.9 times the hydrostatic pressure are obtained at the front face of girder G1 for 65 mm and 80 mm nominal wave heights, respectively (Figure B2, Appendix B). Compared to girder G1, the net pressures on girders G2 and G3 are insignificant, especially when the maximum forces are gained. It is also observed that the pressures at the back faces of girders G1, G2 and G3 pick up slightly earlier than the pressures at the front faces.
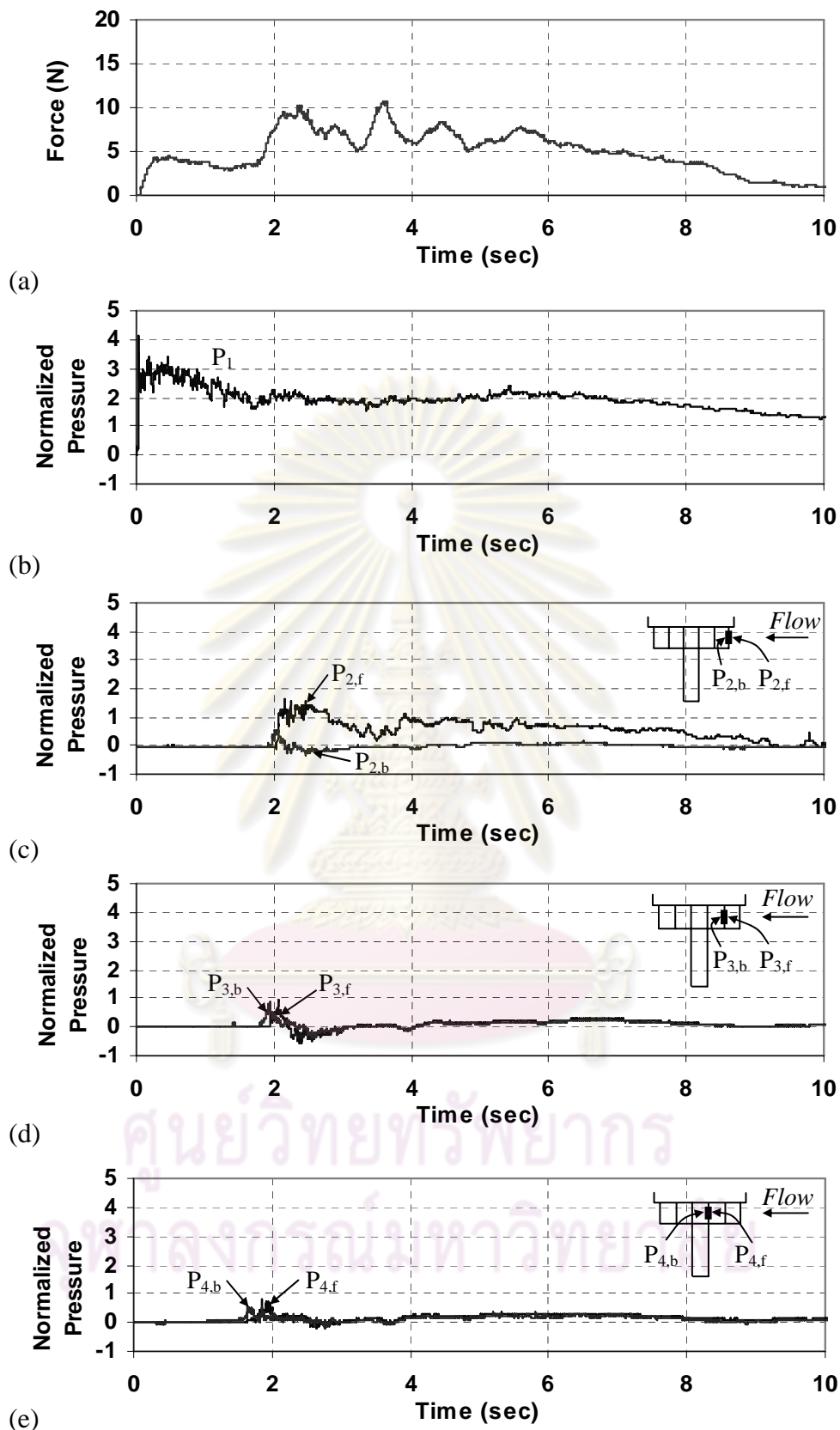
Figure 3.11 Measured time histories of force and pressures ($H = 65$ mm)
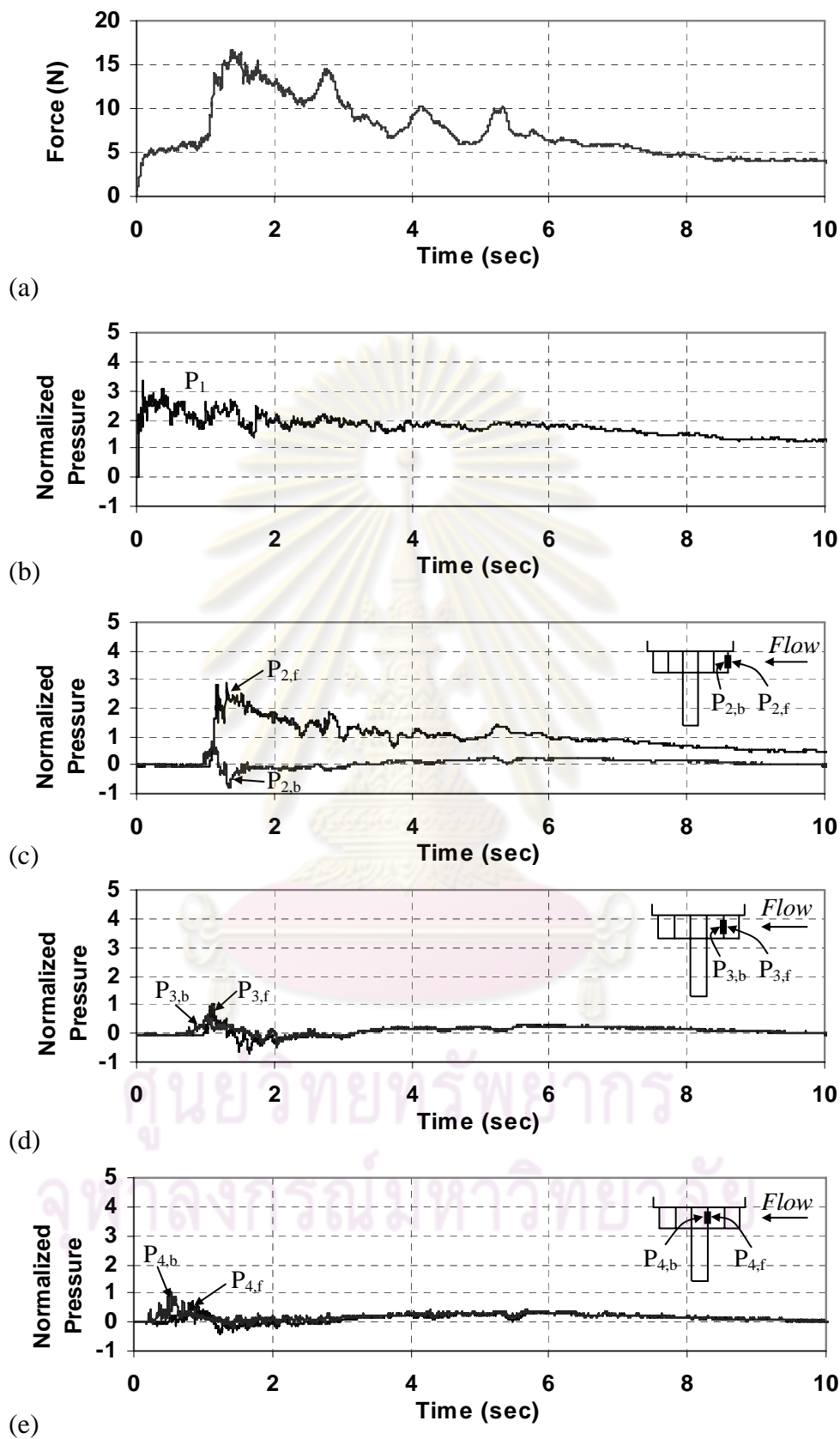
Figure 3.12 Measured time histories of force and pressures (H = 80 mm)

(a) 0 sec

(b) 1.0 sec

(c) 1.9 sec

(d) 2.3 sec

(e) 2.7 sec

(f) 3.0 sec

(g) 3.6 sec

(h) 4.0 sec
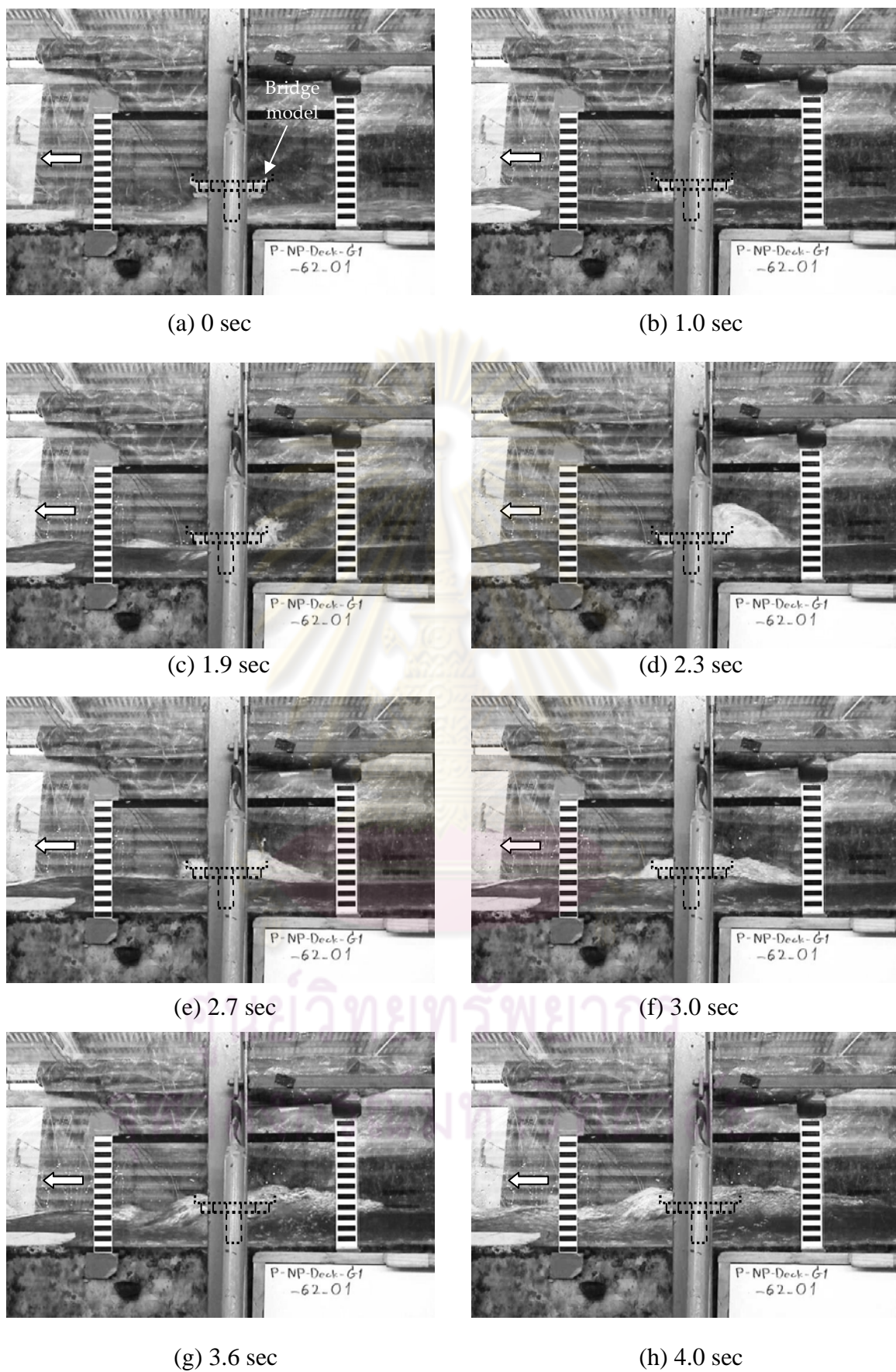
Figure 3.13 Sequences of the wave attack on the bridge model (H = 65 mm)

(a) 0.5 sec

(b) 1.0 sec

(c) 1.5 sec

(d) 1.8 sec

(e) 2.1 sec

(f) 2.4 sec

(g) 2.9 sec

(h) 3.4 sec
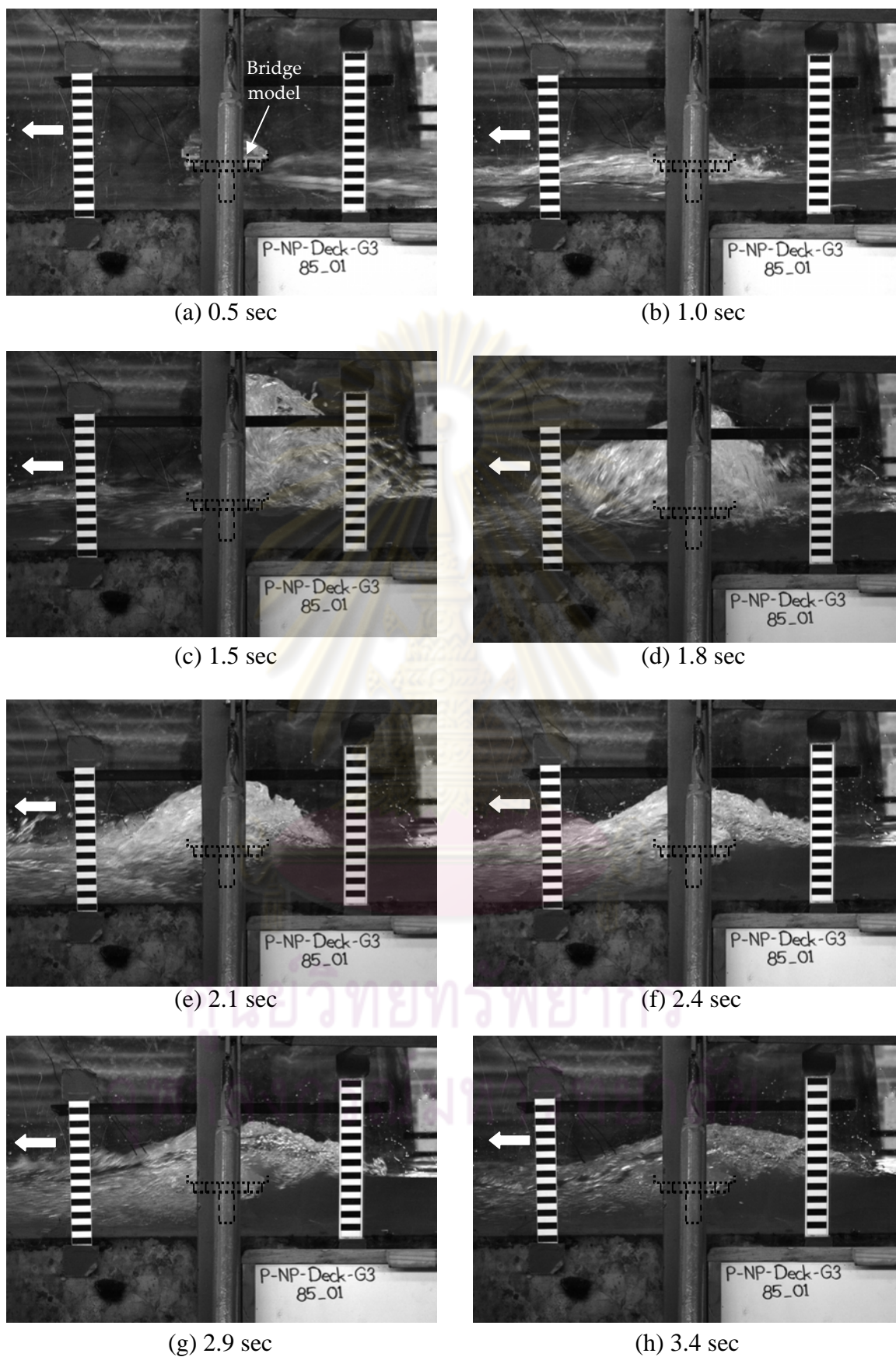
Figure 3.14 Sequences of the wave attack on the bridge model (H = 80 mm)

Table 3.4   Summary of experimental results and the ratio of the peak forces on the
bridge to the piers

Cases	Nominal wave height, H (mm)	Average maximum wave height at H1 (mm)	Average peak force on the piers, F_{pier} (N)	Average peak force on the entire bridge, F_{bridge} (N)	F_{bridge} / F_{pier}	Average F_{bridge} / F_{pier}
SO1_65	65	68	2.75	9.71	3.5	
SO2_65	65	66.6	3.34	10.99	3.3	
SO3_65	65	65.7	3.04	10.10	3.3	3.2
SO4_65	65	68.3	3.14	8.73	2.8	
SO5_65	65	67.2	3.24	10.59	3.3	
SO1_80	80	80.8	6.18	16.09	2.6	
SO2_80	80	80.8	5.69	16.68	2.9	
SO3_80	80	79.4	5.69	15.60	2.7	2.8
SO4_80	80	79.5	6.18	16.38	2.7	
SO5_80	80	80.6	5.89	16.48	2.8	

3.9.2 Horizontal Force Time Histories of Stand-Alone Piers Model

Experiments on the stand-alone piers models were conducted to obtain the force time histories on the bridge piers so that the force time histories on the bridge deck only can then be determined as discussed later. Three experimental runs of each nominal wave height were performed and the results are shown in Figure 3.15. When the wave hits the piers, the force increases drastically to the maximum value, sustains for about a second and reduces subsequently with time.

3.9.3 Tsunami Force on Bridge Piers

The difficulty of this subject is exacerbated by the complication of bridge configuration. Current practice addresses the two components of forces independently for simplicity, i.e. forces on the bridge pier are estimated from a stand-alone piers model such as in Arnason (2005) while forces on the bridge deck are determined from a deck model with the minimum influence from the pier (Kataoka et al., 2006; Iemura et al., 2007). It

should be noted that all these works essentially ignore the influence of the piers and deck on the flow condition around each individual component.

(a) $H = 65$ mm

(b) $H = 80$ mm
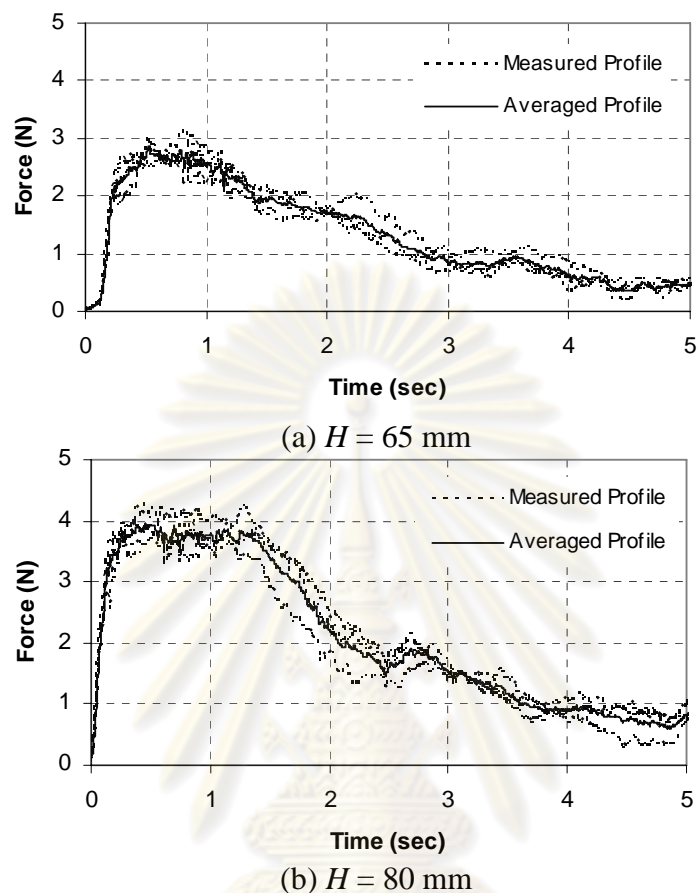
Figure 3.15 Horizontal force time histories on stand-alone piers model

The force acting on a structure by fluid flow in a steady state is widely known as hydrodynamic force or drag force. Present practice of estimating fluid forces on bridge piers is based on the standard drag formula. This formulation is stipulated in the Technical Standards and Commentaries of Port and Harbour Facilities of the Japan Port and Harbour Association (JPHA, 1999), Federal Emergency Management Agency Coastal Construction Manual (FEMA-55, 2000), City and County of Honolulu Building Code (CCH, 2000) and Guidelines for Design of Structures for Vertical Evacuation from Tsunamis (FEMA-P646, 2008). All these publications suggest the drag coefficient (C_d) of 2.0 for square- and rectangular-shape piers, which is based on the experimental studies on stand-alone pier models under a steady uniform flow without overtopping.

In Arnason's work, columns with sufficiently higher height than the run-up height on the structures were placed over a wet bed. Arnason's results confirm the well accepted

value of C_d for a square column at the nearly quasi-steady state flow. However, this scenario differs significantly from the real situation for an actual pier-deck structure when the piers have a limited height. Furthermore, the presence of deck obviously obstructs free overtopping of the wave once it strikes the piers and splashes upward. The influence of the decks on the flow condition around the piers has been ignored or assumed to be non-existing in previous investigations. This study explores this important issue using a more realistic model which included both the piers and decks in the actual proportion. The increase in the tsunami force exerted on the piers as a result of the presence of the deck is examined.

3.9.3.1 Comparison of Wave Attack on Stand-Alone and Complete Pier-Deck Models

The photographs in Figure 3.16 demonstrate the sequences of the wave striking the stand-alone piers and the complete pier-deck bridge models at 80 mm nominal wave height. The models are highlighted as dotted lines for clarity. As the leading edge of the wave strikes the piers, it surges up the piers (as shown in Figure 3.16a). Without the presence of the cross beams and the deck, the wave splashes over freely and it falls at the downstream side of the piers (Figure 3.16b to 3.16d). On the contrary, the flow in the complete pier-deck model exhibits a different scenario. The upward splash hits the soffit of the cross beams and deck which prevent free overtopping over the piers, resulting in accumulation of part of the incoming water as evident from the wave reflection in front of the piers (Figure 3.16) while the remaining part was diverted sideways around the piers.

3.9.3.2 Wave Forces on Bridge Pier Based on a Stand-Alone Piers Model

The force time histories on the stand-alone piers model at 65 mm and 80 mm wave heights are shown in Figures 3.17a and 3.17c. At the initial wave contact with the piers, the wave forces increase rapidly and then remain sustained for about 0.6 sec, after which the forces decrease gradually. It should be noted that the force at initial impact with high velocity does not attain a maximum value because of the extremely small flow depth at that moment, resulting in a small momentum flux. Moreover, the velocity head plays a much more significant role than the flow depth in contributing to the maximum force as it is clearly seen that the force attains a maximum value when the flow depth is still small (compared with the maximum flow depth) whereas the velocity is very high.

(a) t = 0 sec

(b) t = 0.25 sec

(c) t = 0.5 sec

(d) t = 0.75 sec
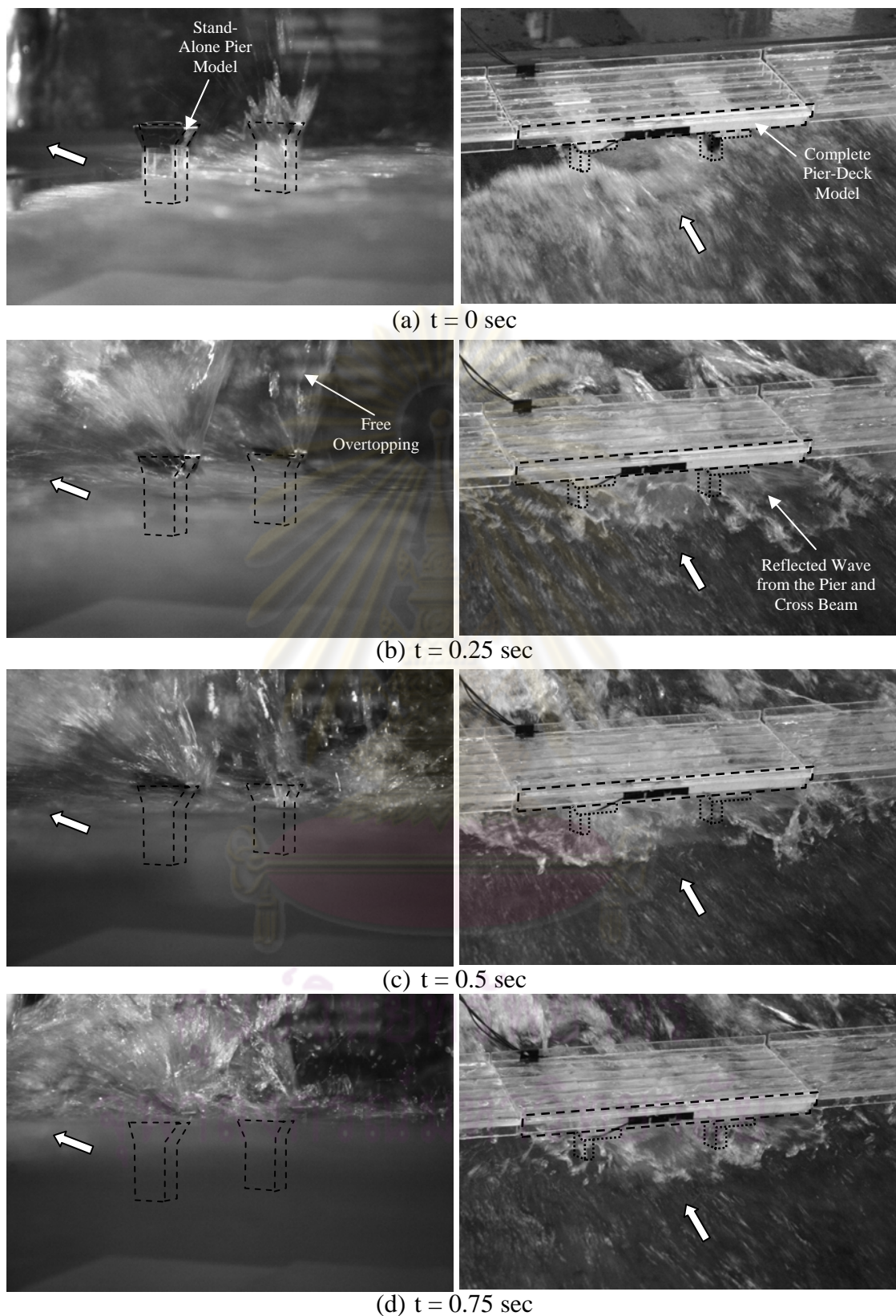
Figure 3.16 Sequences of the wave attack on the stand-alone piers model (left) and the

complete pier-deck bridge model (right) at 80 mm nominal wave height

(a) Stand-alone piers (H = 65 mm) (b) Complete pier-deck (H = 65 mm)

(c) Stand-alone piers (H = 80 mm) (d) Complete pier-deck (H = 80 mm)
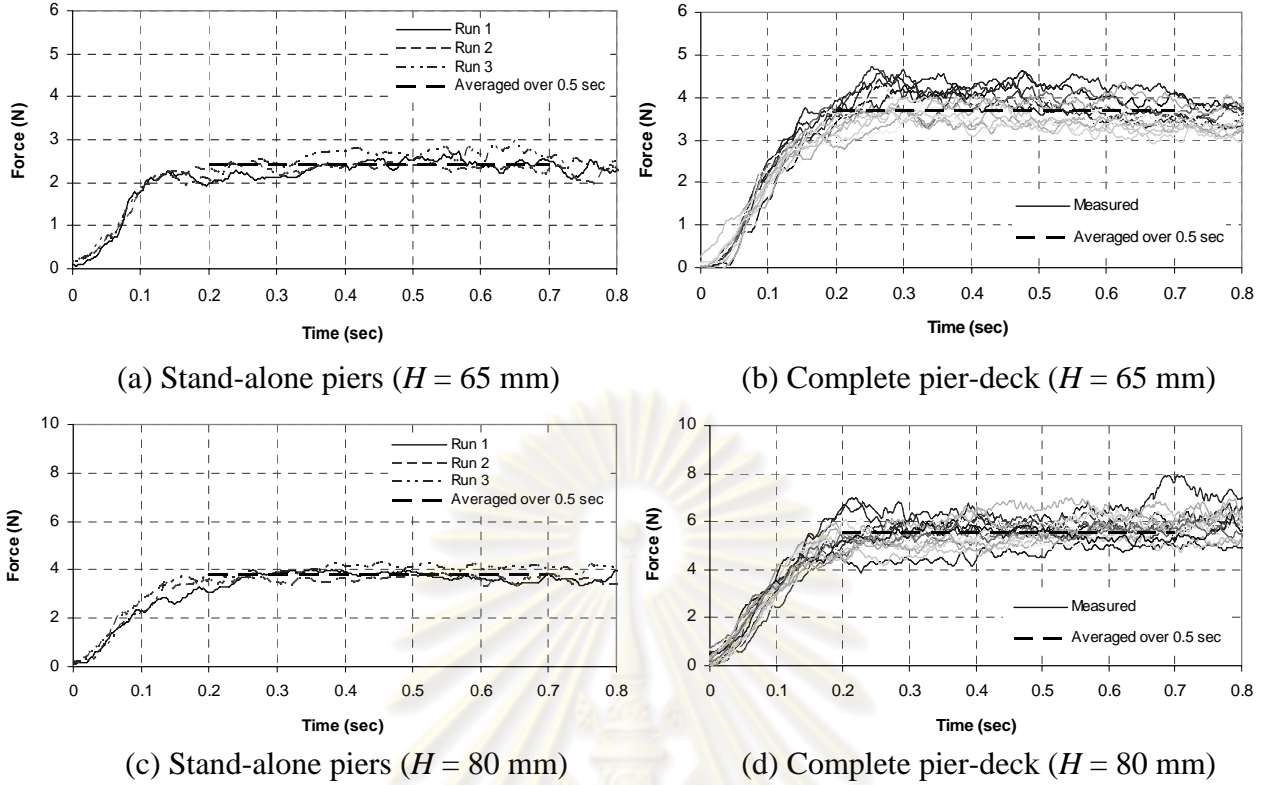
Figure 3.17 Total force time histories on the stand-alone piers model and the complete pier-deck model

The sustained forces of different experimental runs are averaged over an 0.5 seconds interval and their mean value is depicted as the dotted line in Figure 3.17. The mean values are nearly 2.4 N and 3.8 N for the nominal wave heights of 65 mm and 80 mm, respectively. Following the approach used by previous researchers (e.g. Arnason, 2005; Iemura et al., 2007) the flow condition in the time interval considered can be regarded as quasi-steady and the measured force identified as the hydrodynamic force.

The drag coefficient, C_d, associated with the structural geometry is back calculated from the standard drag force formula as follows,

$$F_d = 0.5 \, \rho \, C_d \, A \, v^2 \tag{3.2}$$

where F_d is the hydrodynamic force, ρ is the density of fluid, A is the vertical projected frontal area perpendicular to the flow and v is the flow velocity. The values of the drag coefficient are determined as 1.7 and 1.8 for the 65 mm and 80 mm nominal wave heights, respectively. The computation is based on the force and velocity which are averaged over the 0.5 seconds interval mentioned previously. That the C_d values determined should be

smaller than the widely accepted value of 2.0 (by about 12 % in this case) can be explained as follows. It should be noted that the commonly used C_d value of 2.0 is determined from experiments on rectangular piers with sufficient height so that no overtopping occurs. For the model investigated, significant overtopping takes place, resulting in less drag force exerted on the model than the case without overtopping. However, in design practice, it is customary to adopt the standard drag coefficient of 2.0, resulting in the drag forces of 2.8 N and 4.2 N acting on the piers at 65 mm and 80 mm nominal wave heights, respectively. Therefore, these values will be used instead for comparison with the case of a complete pier-deck model to be discussed next.

3.9.3.3 Wave Forces on Bridge Pier based on a Complete Pier-Deck Model

For the complete pier-deck model, the force time histories during the first one second (approximately) before the wave hits the deck exhibit similar trend of variation as in the case of the stand-alone piers model (see Figures 3.17b and 3.17d). Thereafter, once the wave strikes the bottom of the deck, an abrupt increase in the tsunami force of a much larger magnitude (see Figure B1, Appendix B) is measured. The initial forces (before the wave hits the deck) may thus be regarded as the wave forces on the piers only. As in the stand alone case, the sustained forces are averaged over 0.5 seconds intervals, and their mean values as represented by the dotted lines in the plots are 3.7 N and 5.6 N for the nominal wave heights of 65 mm and 80 mm, respectively. Comparing the hydrodynamic forces at initial wave attack on the piers for the complete pier-deck model as demonstrated in Figures 3.17b and 3.17d with those for the stand-alone piers model based on the C_d of 2.0 as mentioned in the earlier section, one observes a striking finding. The hydrodynamic force on the piers with the presence of the deck is significantly higher than that on the stand-alone piers by about 33 % for both nominal wave heights. This increase is attributed to the effect of upward splash of the incoming wave front hitting the piers, most of which is obstructed by the cross beams of the deck with the consequence of reflected wave in front of the piers on top of the incoming wave as evident from the snapshot of the flow at 0.3 seconds in Figure 3.18. Thus, an increase in pressure on the piers is created.
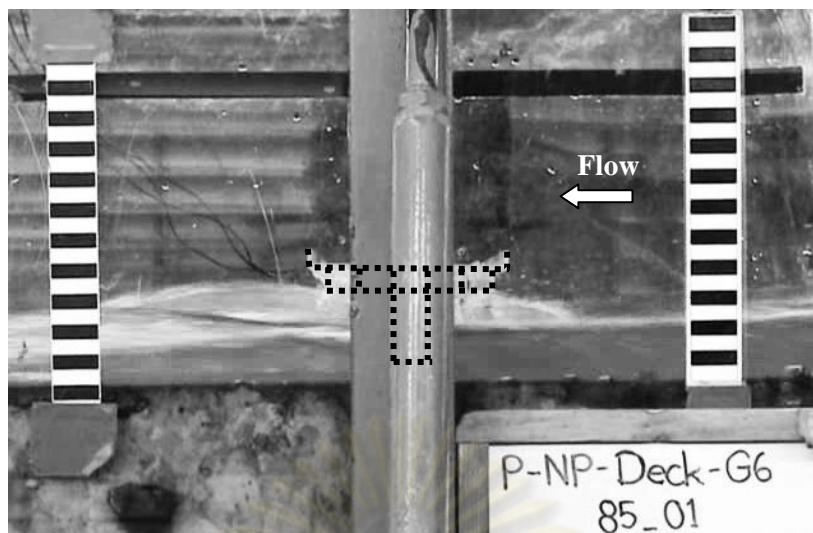
Figure 3.18 Snapshot of flow past the pier-deck model. Note the reflected wave in front of the piers (on top of the incoming wave) seen as lighter color flow

3.9.4 Pressure Time Histories at Front Girder of Perforated Bridge Decks

Figure 3.19 illustrates the typical time histories of pressures for all type of bridge models at both 65 mm and 80 mm nominal wave heights. The pressure shown in the figure is normalized by the hydrostatic pressure $\rho g H$, where ρ is the density of water; g is the gravitational acceleration; H is the nominal wave height or the maximum wave height. The time starts from zero when the wave hits the bridge pier. The pressures were recorded from pressure gauges at the base of the front face of the bridge pier (Pressure $P_{1,f}$) and the mid-span of the front girder (Pressure $P_{2,f}$ at the front face and Pressure $P_{2,b}$ at the back face) that was exposed to the direct wave attack. At the initial wave attack on the bridge pier, Pressure $P_{1,f}$ attains its maximum value while no pressure is measured at the girder. The maximum normalized pressure of $P_{1,f}$ is approximately 3.5 to 4.5 for all types of deck configuration. Pressures $P_{2,f}$ attains its peak normalized pressure from 2.5 to 3 when the wave splashes up and hits the deck. At this moment, the normalized pressure $P_{1,f}$ varies between 2 to 2.5. The normalized pressures become constant subsequently, which mark 1.5 to 2 and 1 to 1.5 for pressures of $P_{1,f}$ and $P_{2,f,}$ respectively. Pressure $P_{2,b}$ records relatively low pressure except at the initial wave attack on the deck, in which the normalized pressure ranges from 0.5 to 1. A negative pressure is obtained right after the first peak pressure with the normalized pressure less than 0.5.
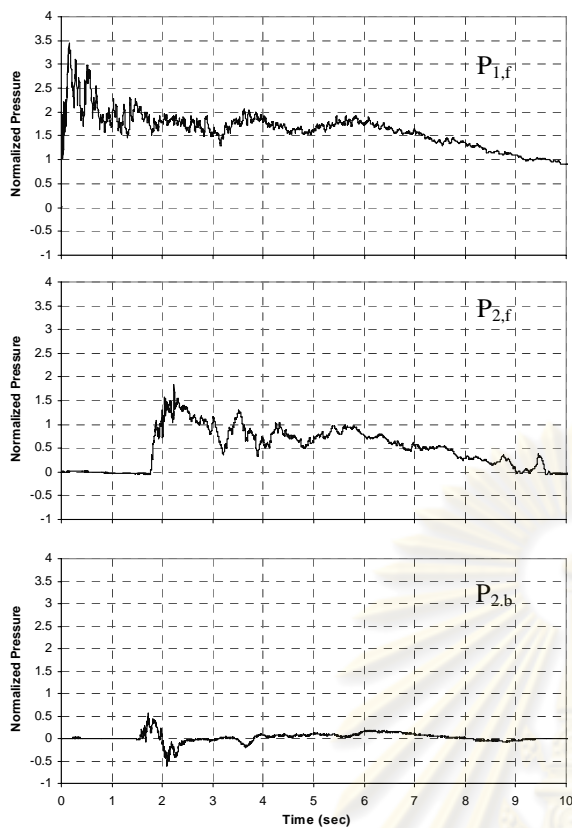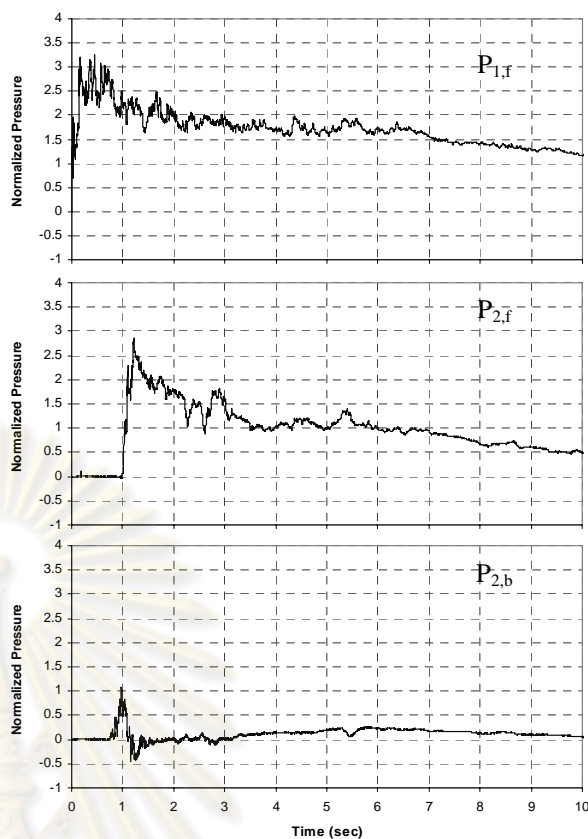
(a) G0+P0 (*H* = 65 mm)   (b) G0+P0 (*H* = 80 mm)
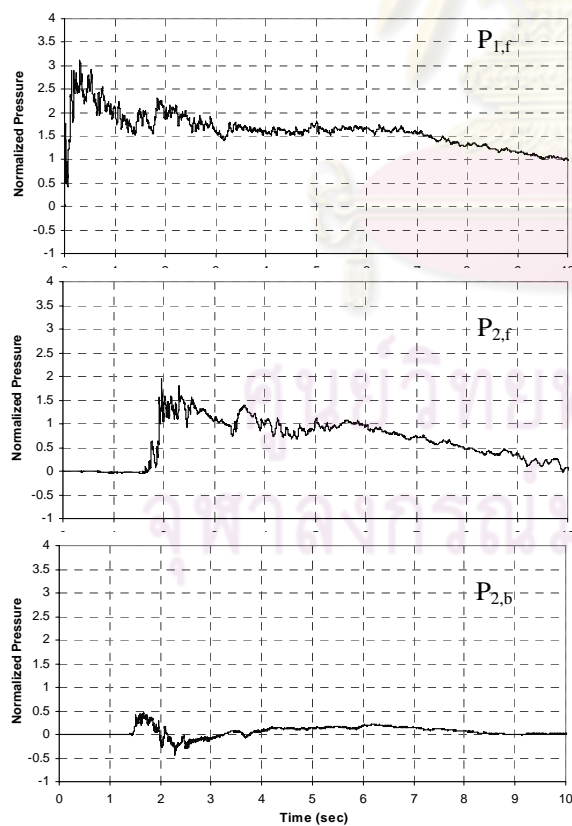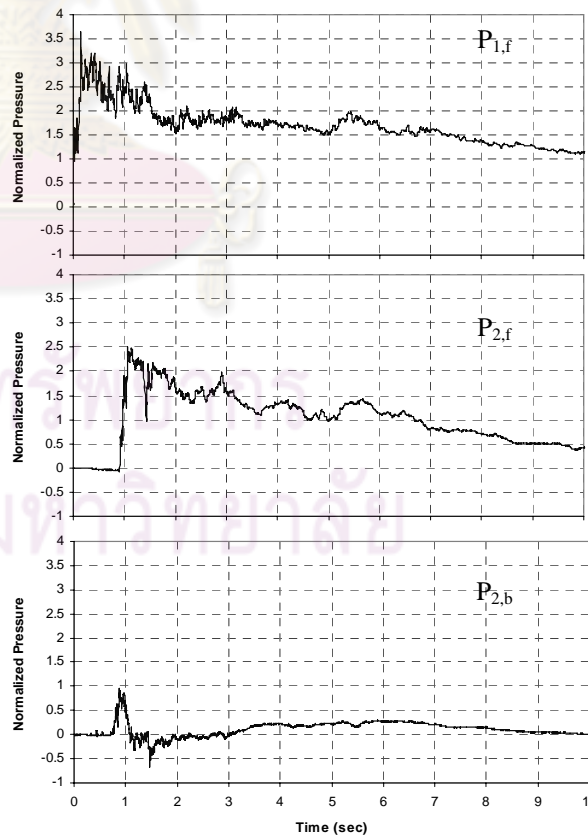
(c) G0+P60 (*H* = 65 mm)   (d) G0+P60 (*H* = 80 mm)

Figure 3.19 Pressure time histories at 65 mm and 80 mm nominal wave heights
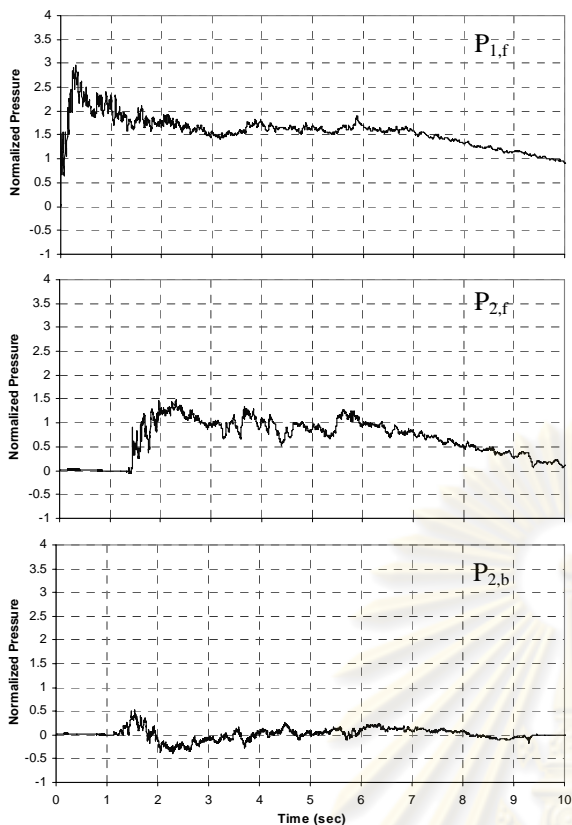
(e) G20+P0 (*H* = 65 mm)
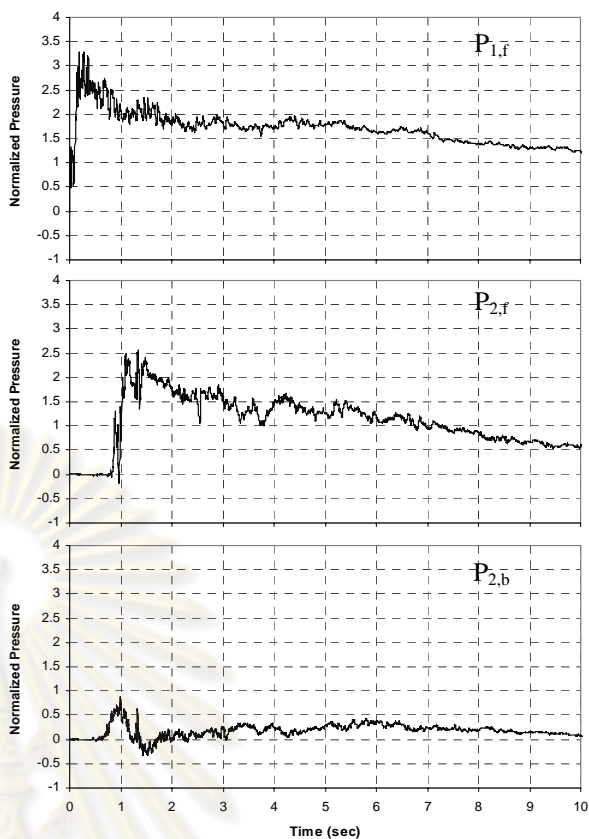
(f) G20+P0 (*H* = 80 mm)
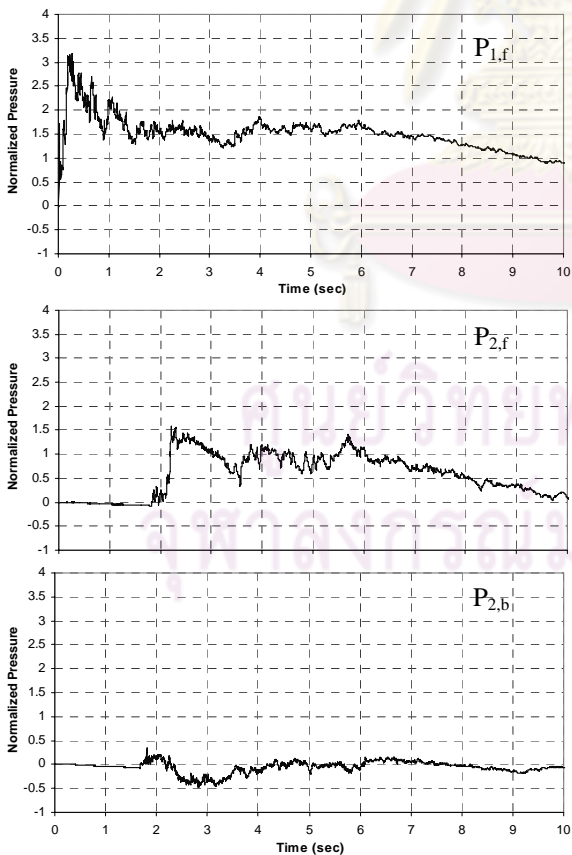
(g) G20+P20 (*H* = 65 mm)
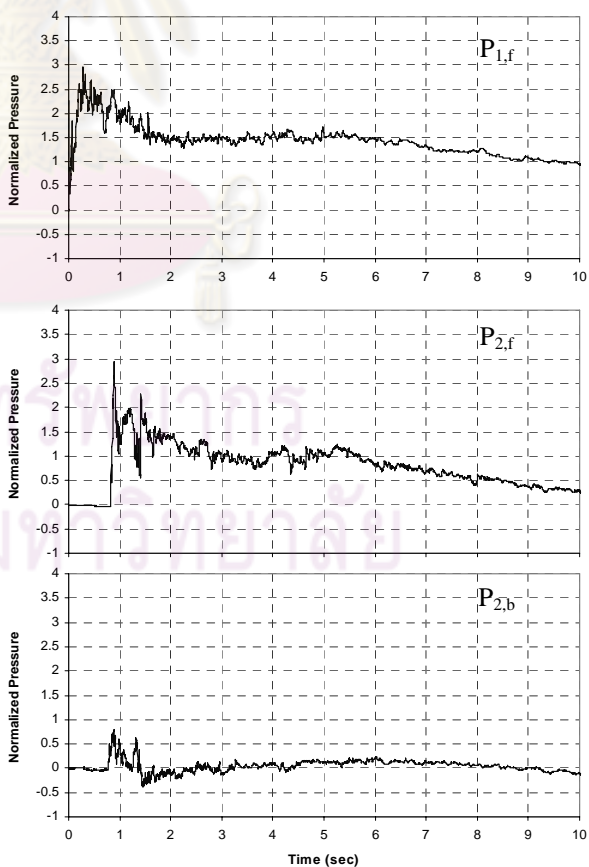
(h) G20+P20 (*H* = 80 mm)

Figure 3.19 (Cont'd)
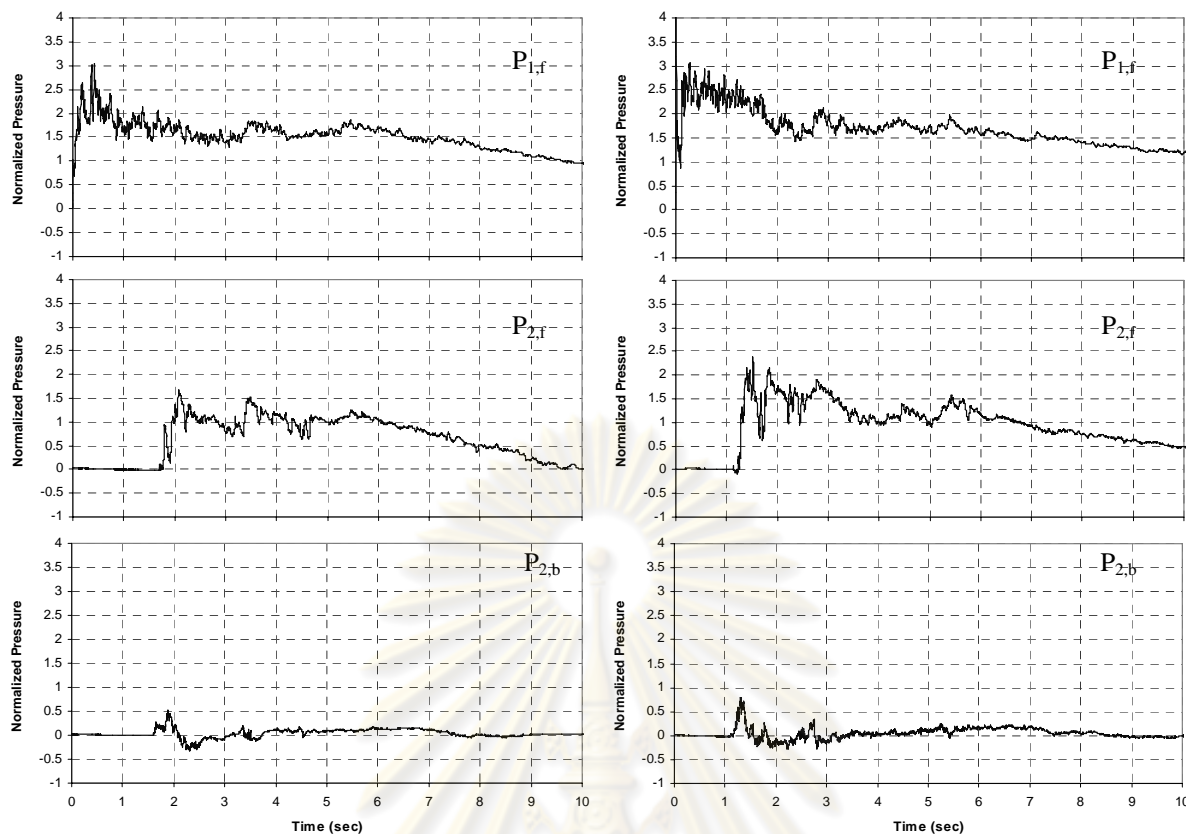
(i) G10+P60 (H = 65 mm)   (j) G10+P60 (H = 80 mm)

Figure 3.19 (Cont'd)

Due to the limited pressure gauges, the pressure at the mid-span of the first girder was only recorded. The effect of various deck configurations on the pressure distribution may not be studied in detail at the moment. From the time histories of the front face girder, there is no significant variation of the peak pressure among those deck configurations. Nevertheless, one of the significant observation in the recorded pressure time histories is that the pressure P_2 on the front girder fluctuates noticeably especially in the cases with larger perforation area.

CHAPTER IV

NUMERICAL MODELING

Numerical simulations were performed subsequently to further investigate tsunami flow around inland bridges. The state-of-the-art computational fluid dynamics (CFD) program, Flow-3D®, was used in this study to simulate the tsunami flow at I-girder bridge models and prototypes. To ensure the appropriateness of the numerical model in simulating tsunami flow, wave flume experiments (under free flow condition without the bridge model) as performed in the experiment during calibration was reproduced numerically using a two-dimensional (2D) model as the first step. It was then followed by a detailed investigation of tsunami flow around the bridge model using a three-dimensional (3D) numerical model. The 3D model is then extended to the prototype scale in order to simulate the real flow mechanics around the target bridge prototypes. Calculation results of various test combinations are presented. The issue of simplification on the bridge configurations is addressed at the end of this chapter. Discussion in this chapter is limited to the most severe scenario considered in this study, i.e., the case of 80 mm (in model) or 8 m (in prototype) nominal wave height.

4.1 Numerical Methodology

Flow-3D® employs the finite-volume-finite-difference method to solve the time-dependent Reynolds Averaged Navier-Stokes (RANS) equations of motion. It includes the nonlinear convective terms. In this program, pressure and velocity, instead of the stream function or vorticity, are used as the primary dependent variables. For each time step, the average values for flow variables are computed using a staggered grid technique. The program is developed based on the fractional volume of fluid (VOF) to track the free surface, employing a type of donor-acceptor flux approximation as discussed in Hirt and Nichols (1981). Under this method, a value of zero to one is assigned for each cell, representing the fraction of cell filled with fluid: the empty cells are defined with zero while fully filled cells with fluid are defined as one. For partially filled cells, the filled portion of the fluid is determined by an algorithm that uses the fluid information of the surrounding cells. This allows even the steep slope of the free surface to be tracked and it would be applicable to describe wave breaking in tsunami run-up zone.

On top of that, the flow obstacle is also defined using a porosity technique in rectangular cell meshes called the Fractional Area/Volume Obstacle Representation (FAVOR) method as outlined in Hirt and Sicilian (1985). The method applies the similar principal of VOF: a value of zero to one is assigned to define cell filled with the obstacle based on the fraction of the cell that is open. For cells without obstacle, the grid porosity is one whereas the grid porosity is zero for cells within obstacle. For cells that are partially filled with an obstacle, the grid porosity has a value between zero and one, and the surface of the obstacle within the cells can be defined based on the obstacle information of the surrounding cells.

The computational domain is defined in a fixed rectangular grid or structured system. For a two-dimensional case, the variable sizes in the x- and y-directions are represented by δx_i for the ith column and δy_j for the jth row as shown in Figure 4.1. Discrete values of the dependent variables of the pressure (p) and the fractional volume of fluid (Φ) are defined in the center of a cell, while the velocity variables (u and v) are defined in the middle of each mesh as shown in Figure 4.1.
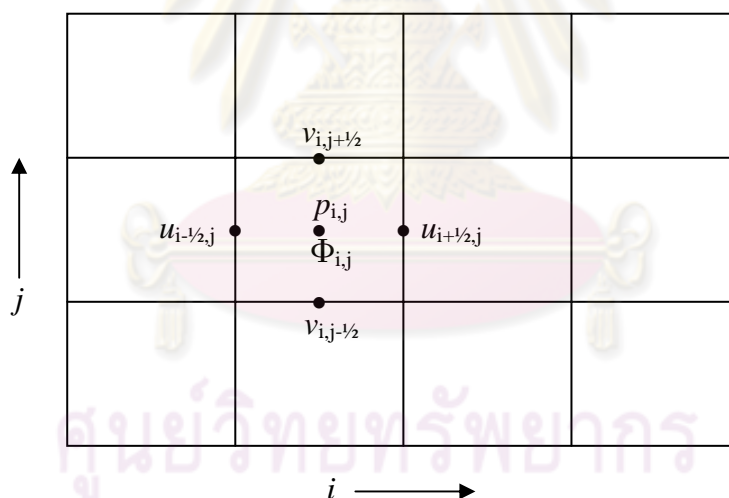
Figure 4.1 Schematic diagram of finite-difference mesh and location of variables

For this study, various assumptions have been made as follows:

1. The fluid is incompressible. The fluid density is constant and the propagation of acoustic pressure is neglected.

2. Newtonian fluid is used where the shear stress of the fluid is linearly proportional to the velocity gradient.

3. The inertia of the air adjacent to the fluid is neglected and the cell occupied by the air is represented by an empty cell.

4. The bed of the flume is frictionless.

5. The bridge model is a rigid body.

Based on the assumptions, the fluid momentum equations, Navier-Stokes equations, can be expressed as follows (Flow-3D, 2007),

$$\frac{\partial u}{\partial t} + \frac{1}{V_F}\left(uA_x\frac{\partial u}{\partial x} + vA_y\frac{\partial u}{\partial y} + wA_z\frac{\partial u}{\partial z}\right) = -\frac{1}{\rho}\frac{\partial p}{\partial x} + g_x + f_x$$

$$\frac{\partial v}{\partial t} + \frac{1}{V_F}\left(uA_x\frac{\partial v}{\partial x} + vA_y\frac{\partial v}{\partial y} + wA_z\frac{\partial v}{\partial z}\right) = -\frac{1}{\rho}\frac{\partial p}{\partial y} + g_y + f_y \qquad (4.1)$$

$$\frac{\partial w}{\partial t} + \frac{1}{V_F}\left(uA_x\frac{\partial w}{\partial x} + vA_y\frac{\partial w}{\partial y} + wA_z\frac{\partial w}{\partial z}\right) = -\frac{1}{\rho}\frac{\partial p}{\partial z} + g_z + f_z$$

where u, v and w are the velocities in the x-, y- and z-directions; V_F represents the volume fraction of fluid in each cell; A_x, A_y and A_z are the fractional areas open to flow in the x-, y- and z-directions; ρ is the fluid density; p is the fluid pressure; g_x, g_y and g_z are the body accelerations in the x-, y- and z-direction and f_x, f_y and f_z are the viscous accelerations in the x-, y- and z-direction for which a turbulence model is required for closure. For cells fully filled of fluid, V_F and A_j equal to one. The wall shear stress which is related to the surface roughness of the wall is incorporated into the viscous acceleration term in Eq. (4.1). The surface roughness, defined in a length dimension, is the average depth of imperfection on the surface of the wall.

For an incompressible fluid, the following condition (i.e. continuity equation) must hold:

$$\frac{\partial}{\partial x}(uA_x) + \frac{\partial}{\partial y}(vA_y) + \frac{\partial}{\partial z}(wA_z) = 0 \qquad (4.2)$$

Boundary conditions are categorized as symmetry, rigid-free or no-slip walls, continuative outflow, periodic and specific pressure boundaries. No flux is allowed to cross the symmetry and wall boundary; however, viscous shear stresses occur at the wall boundary only. Flow variables (velocity, pressure, etc) are constant across boundary (zero

gradient). A continuative boundary condition consists of zero normal derivatives at the boundary for all flow quantities; thus, there is no acceleration or deceleration of the flow as it crosses the boundary. Free slip is defined as zero normal velocity component with zero tangential velocity derivatives ($v = 0$ and $\partial u/\partial x = \partial w/\partial z = 0$). No slip is defined as zero tangential and normal velocities ($u = v = w = 0$).

Hydraulic forces that fluid flow exerts on the solid structures are calculated by integrating the pressure acting on these structures over the open surface. Hydraulic forces which comprise the pressure and viscous forces are defined as

$$F = \int p\bar{n}dA + \int \bar{\tau}dA \tag{4.3}$$

where p is the pressure, dA is the solid surface area in the cell, $\bar{n}$ is the unit vector normal to area dA and $\bar{\tau}$ is the shear stress vector.

4.1.1 2D Wave Flume Model

The computational domain was discretized into an orthogonal and staggered grid of variable-sized hexahedral meshes in a Cartesian coordinates. A single layer of fictitious cells is added to surround the fluid region so that the boundary conditions can be defined. Due to the complexity of the model, multi-block gridding with nested and linked grids were applied in order to reduce the computational cost while maintaining the accuracy of the results.

Numerical computational domain for a 2D wave flume model is defined to represent the similar layout in the experimental setup as shown in Figure 3.2. The details of the experimental setup are explained in Chapter III. Figure 4.2a illustrates the numerical layout of the 2D wave flume model. The total length of the flume was 40 m with the height of 1 m. The wave maker which consisted of about a 3 m high elevated water tank was included. The water in the elevated tank was set at 0.9 m for the case discussed in this chapter. Without the interaction with the bridge model, it was assumed that the flow in the flume remained two-dimensional even after the wave breaking took place. The model was constructed using three linked blocks with one nested block which contained the finest mesh density as listed in Table 4.1. Numerical input parameters are provided in Table 4.2. The total number of cells was 536,388. The origin of the

coordinate system is at the left boundary, with the *x*-axis directed toward the wave maker and the *z*-axis directed upward. The boundaries at the upstream and the downstream of the flume model were defined as wall and outflow, respectively. The bottom and upper boundaries of the flume were assigned as symmetry. Newtonian viscosity with two equation (*k*-*ε*) turbulence model was adopted. With the time interval of 0.05 sec and the running time of 25 sec, the computation was completed in 4 hours and 41.5 minutes, using the Intel® Core™ 2 Duo processor with a 3.16GHz and an 8GB RAM's computer.

(a) 2D wave flume model

Note: Mesh size is shown in parentheses ($\Delta x \times \Delta y \times \Delta z$)
Notations for boundary condition: S - symmetry; W - wall; C – continuative; V – velocity; O - outlet

(b) 3D bridge model
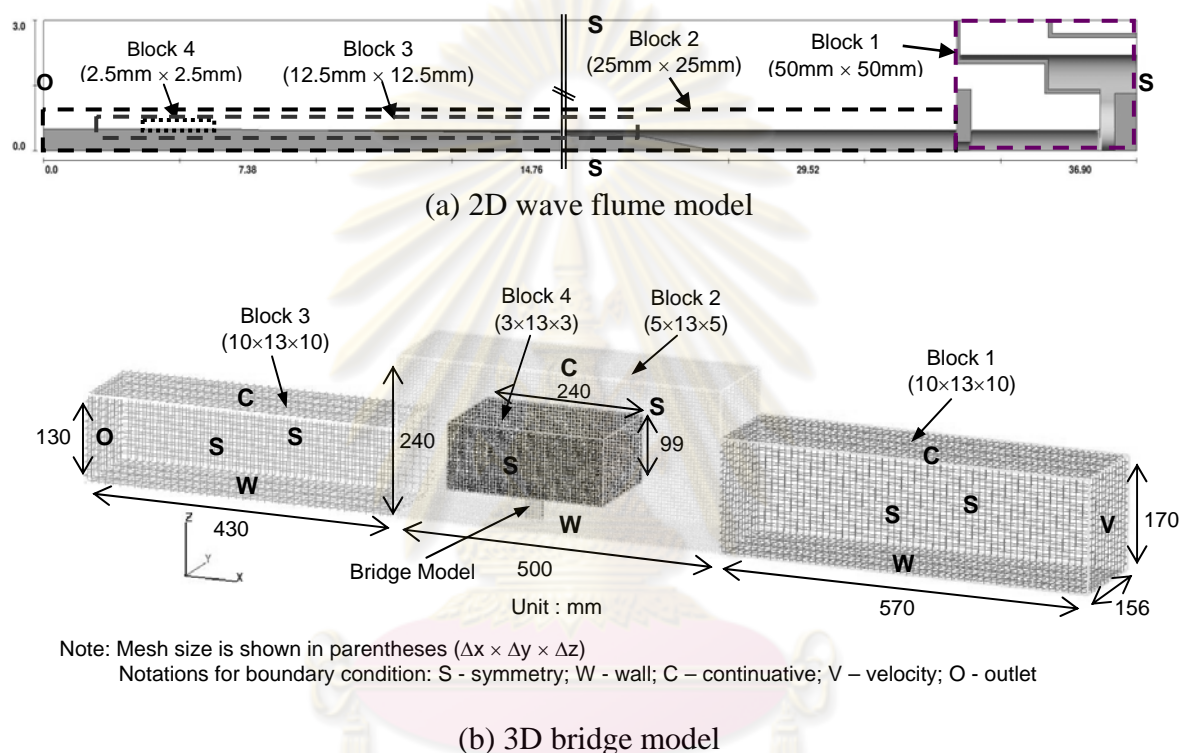
Figure 4.2 Numerical models

Table 4.1   Mesh properties for 2D wave flume model

Block	Type	Total Length (m)			Interval (mm)		
		x	y	z	Δx	Δy	Δz
1	Linked	4.9	0.5	3	50	500	50
2	Linked	31	0.5	0.9	25	500	25
3	Linked	20	0.5	0.4	12.5	500	12.5
4	Nested	2	0.5	0.2	2.5	500	2.5

Table 4.2   Numerical model parameters

Parameters	Quantities
Fluid Density	1000 kg/m^3
Air Density	1.225 kg/m^3
Fluid Viscosity	0.001 kg/m/s
Gravitational Acceleration	-9.81 m/s^2
Surface Roughness	0.0 mm

4.1.2 3D Bridge Model

Three-dimensional bridge models (Figure 4.3) were constructed individually in the latter stage due to the fact that the downscaled bridge model is comparatively small (nearly 1/12 in height and 1/290 in length) as compared to the whole flume model. The calculation of flow at the bridge model using the whole flume model for 3D flow would be too costly in computation and the flow mechanics cannot be clearly visualized at such a small scale model. Thus, a 3D bridge model in the computational domain of 1.5 m long by 0.25 m high (maximum) by 0.299 m width was used as shown in Figure 4.2b. The coordinate system is arbitrarily set with the origin located 1.5 m to the left boundary, with the y-axis and z-axis directed toward the right end (from front view) and upward, respectively. The simulation was first carried out for the case without bridge model and followed with the bridge model in the flat bed as performed in the experiment. Bridge and other auxiliary structures were constructed as rigid obstacles in the numerical model. The computational domain contained three linked blocks with a nested block of meshes as summarized in Table 4.3. Numerical input parameters are provided in Table 4.2. The bridge model was located in the middle block (Block 2) where the bridge deck was enclosed in the nested block (Block 4) with higher resolution (Table 4.3). The total number of cells was 141,996 and the required time to complete the running time of 5 sec at 0.05 sec interval in the same computer capacity as mentioned in the earlier section was 3 hours and 59 minutes.

For 3D models, six different boundaries of each block were defined. Sidewalls (y) were defined as free slip/symmetry, the bed (bottom z) was no slip/wall; the top was continuative; the upstream (right x) and downstream (left x) were velocity boundary and the outlet, respectively. Overlapping boundaries would be detected and recognized by the program. The surface of the bridge model was assumed smooth with no slip. The inflow

boundary condition (right boundary) was a time-dependent velocity boundary. The inflow properties were input at the upstream boundary with time-dependent velocity and height data, assuming these quantities were uniformly distributed along the width and the height of the flume at each time step. The input data (velocities and flow depths) were taken from the experimental results.

Unit : mm

Figure 4.3 Isometric view of a complete pier-deck bridge model

Table 4.3   Mesh properties for 3D bridge model

Block	Type	Total Length (m)			Interval (mm)		
		x	y	z	Δx	Δy	Δz
1	Linked	0.57	0.156	0.17	10	13	10
2	Linked	0.5	0.156	0.24	5	13	5
3	Linked	0.43	0.156	0.13	10	13	10
4	Nested	0.24	0.156	0.099	3	13	3

4.2 Model Validation

4.2.1 2D Wave Flume Model

Validation of the numerical model is one of the most crucial steps in the numerical simulation process especially when the model is used as a numerical tool for solving the complex flow condition. Without proper care in this step, the model may produce misleading results and cause undesirable consequences. Therefore, special considerations on the level of uncertainties associated with the input data, the appropriateness of solution approach and the result interpretation need to be taken into considerations (Ho et al., 2003). Because of the complexity of the problem and the scarcity of the knowledge in the

current research focus at this stage, the appropriateness of the simulation procedure is ensured by calibration with experimental data.

Figure 4.4 demonstrates the simulated free surface geometry, corresponding to those captured in the experimental as shown in Figure 3.3. Comparing these two figures, it shows that the simulation results agree qualitatively with experimental results though there has slight variation in the location of wave breaking which is estimated in the order of less than one meter.
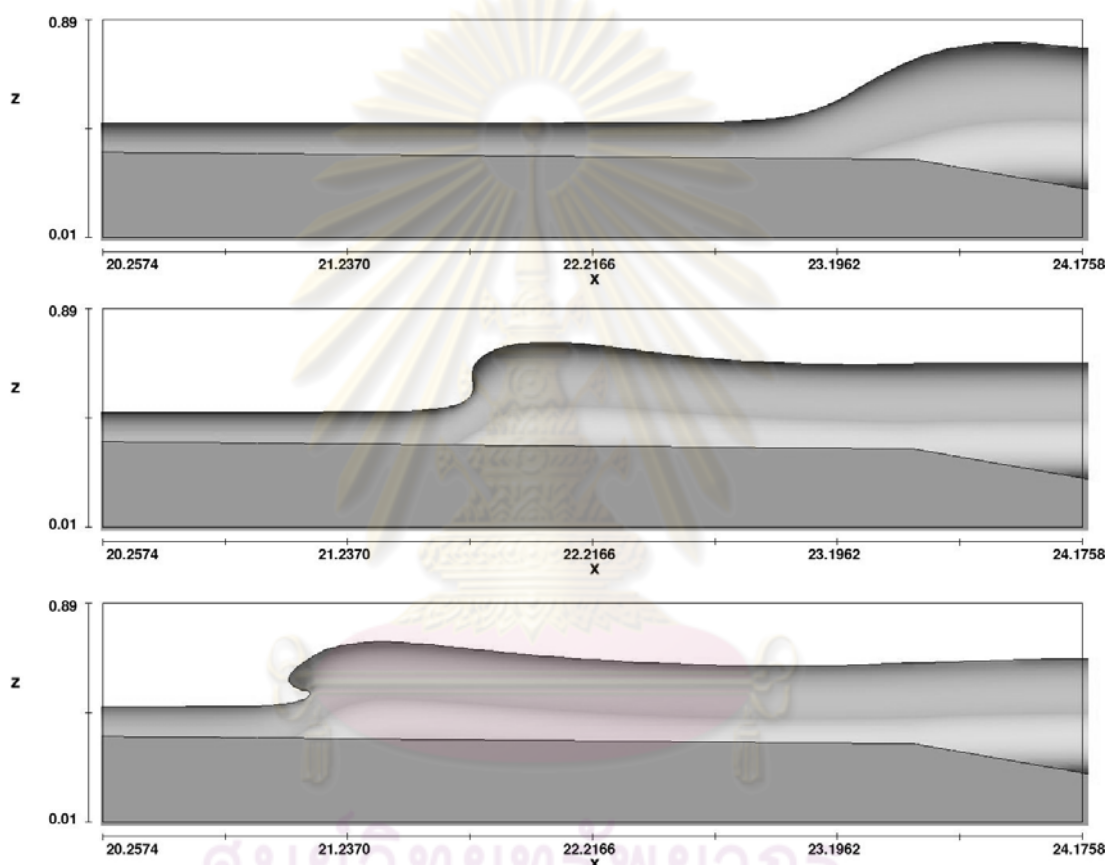
Figure 4.4 Simulated wave profiles

The measured and calculated wave heights and flow velocity at both offshore and onshore regions are compared in Figure 4.5. The measurement point at the onshore region is at the location of the bridge model. Generally, the results from the simulation are in good agreement with the experimental data in terms of the profile and the magnitude of the flow variables. However, the simulated arrival time at the location of the model is approximately 0.5 sec later, which may regarded as insignificant. Also observed is the smoother wave form in the simulated result than the recorded data. This may due to the simplification of the 2D model in modeling wave breaking process. In the actual

experiment the flow is not truly two dimensional, resulting in lateral disturbances in the flow. The arrival time for the velocity record in the experiment cannot be accurately traced due to the limitation in synchronization of the instruments in the experiment. It is assumed to be started at the same time with the arrival time of the flow depth. Therefore, the velocity record starts 0.5 sec earlier than the simulated one. However, for the purpose of comparison of the measured and simulated velocities, both velocities are plotted at the same starting time in the figure. In addition, the velocity recorded in the experiment is slightly lower than the simulated value in the first 0.5 sec due to the inertia and the finite size of the current meter rotor. Nonetheless, it may be concluded that this 2D numerical wave flume model can represent reasonably well the one in the physical model.

4.2.2 3D Bridge Model

The bridge model was next installed at the location of about 1 m from the designated right boundary. The similar wave condition was applied and several important flow parameters were obtained for validation purpose. These data are the forces acting on the entire bridge model and the pressures acting on the piers and girders. From the initial run by assuming the surface roughness of 0.00 mm, the simulated force was significantly lower than the measured force from the physical experiment. Therefore, the surface roughness of the pier was adjusted to 0.05 mm and the good agreement was obtained as presented in the following.

Figure 4.6 highlights the wave profile when the generated wave strikes the model at different time intervals. In general, the wave impingement phenomena are well simulated qualitatively by the numerical model as those observed in the experiments as illustrated in Figure 3.16. Due to the mesh size used in the calculation model, water particles of splashing wave that are more finer than the mesh size cannot be shown in the numerical results.

Wave pressures on the bridge model are measured in the front center face of the pier (at 5 mm above the bed) and the front and back face of girders (at mid-span of the girder and 63.5 mm high from the bed). For validation purpose, the pressure in the front face of the pier ($P_{1,f}$) and the front and back faces of the front girder ($P_{2,f}$ and $P_{2,b}$) are discussed. The pressure time histories obtained from the physical and numerical models are compared in Figure 4.7 while the time histories of the total horizontal drag force (pressure and viscous drag forces) acting on the entire bridge model are compared in

Figure 4.8. The results show close approximations of the simulated pressures and forces with the measured pressures and forces. Good agreement of the pressures and the forces throughout the considered time domain has evidently justified that this 3D numerical bridge model can reproduce the physical bridge model with high confidence. Consequently, this validated model is used in subsequent studies to simulate the bridge prototype as discussed in the following section.
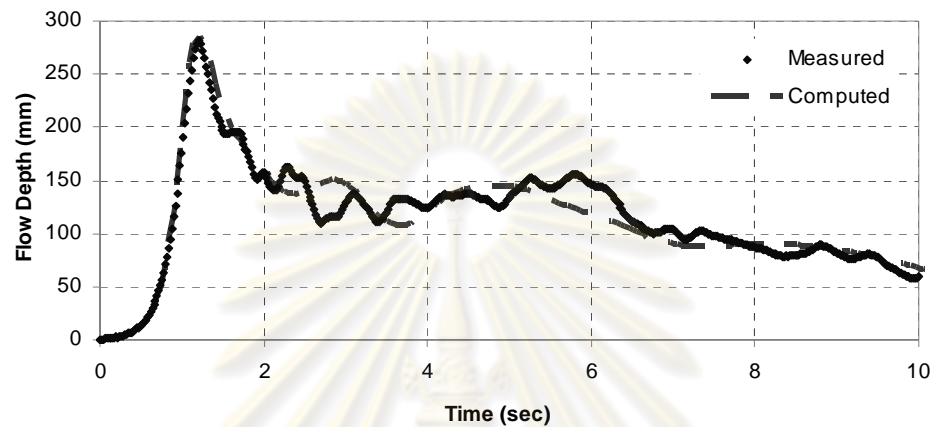
(a) Offshore flow depth (H2)
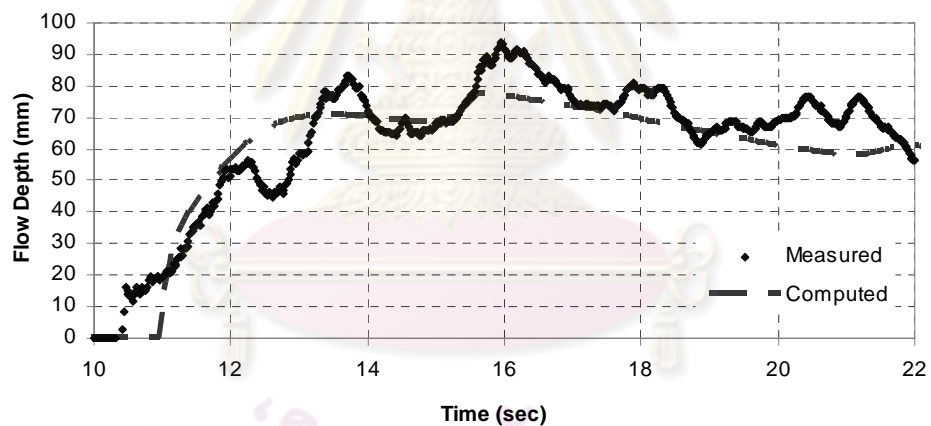
(b) Onshore flow depth (H1)
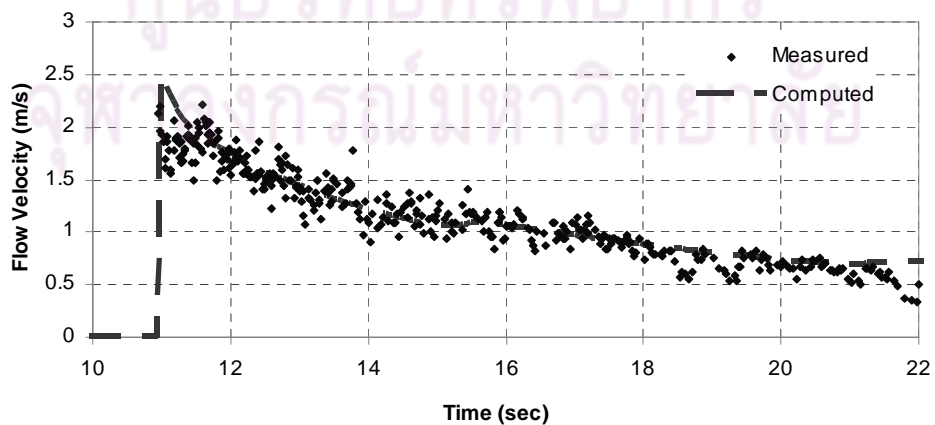
(c) Onshore flow velocity (V1)

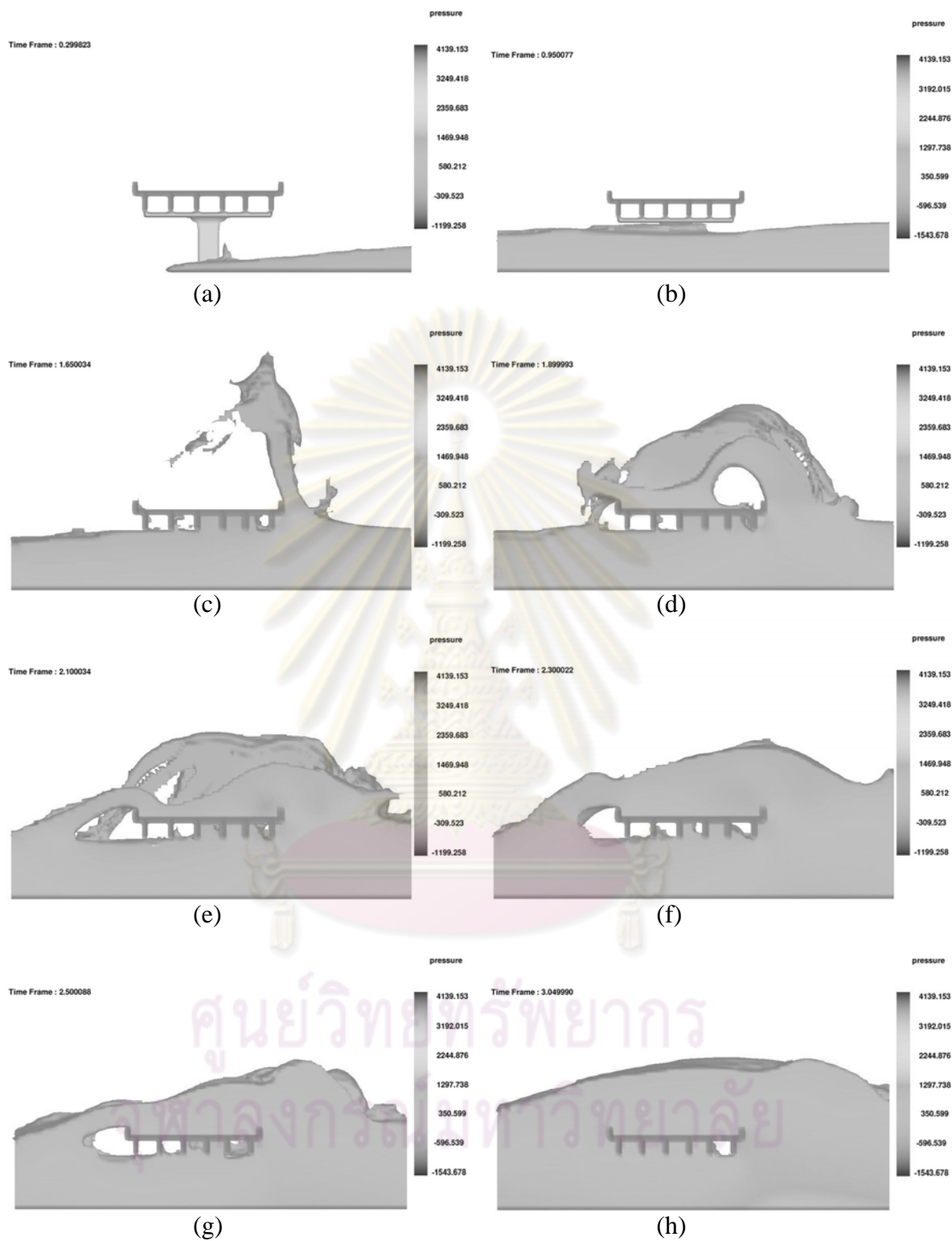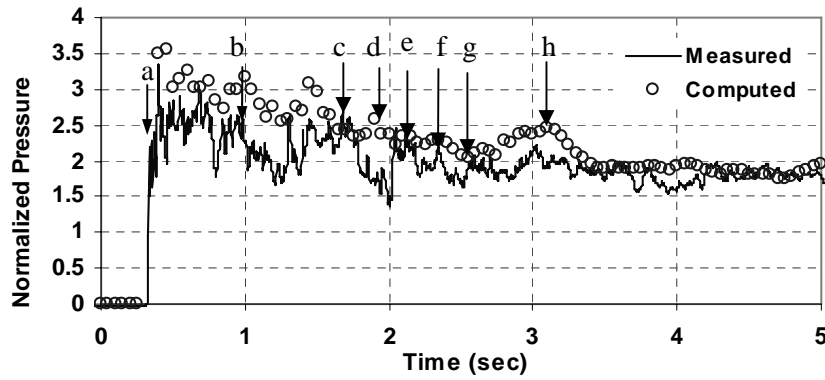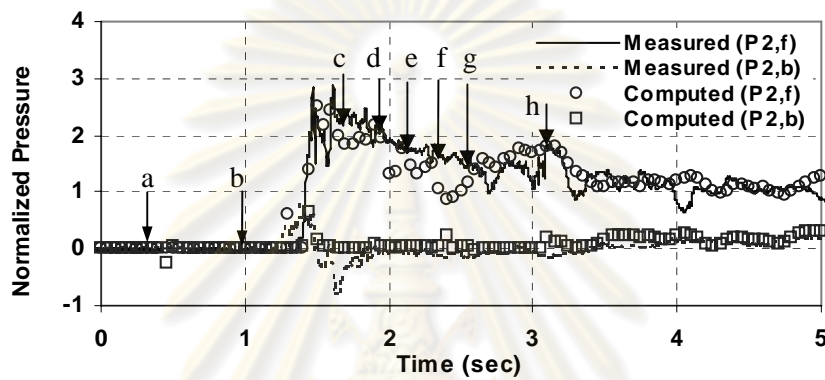Figure 4.5 Comparisons of undisturbed flow variables

Figure 4.6 Wave impingement on bridge deck from simulation model

(a) Front face of pier

(b) Front and back faces of front girder

Figure 4.7 Comparison of the measured and simulated pressure time histories of 3D
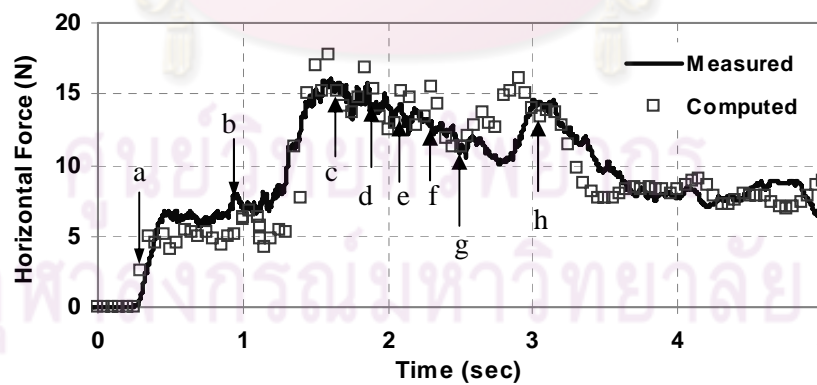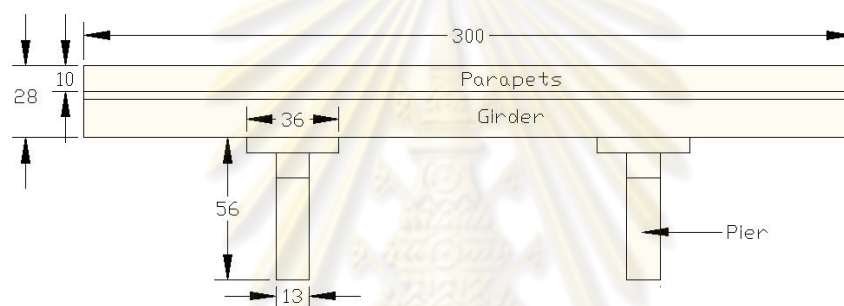
bridge model

Figure 4.8 Comparison of the measured and simulated force time histories of 3D bridge

model

4.3 Bridge Prototype Simulation

4.3.1 Modification of Bridge Pier Layout

In the hydraulic experiments, the actual distance (center to center) between the piers of 300 mm in the scaled model based on a typical bridge prototype had been shifted to a shorter distance of about 150 mm as illustrated in Figure 4.9 for the reason as mentioned in Section 3.5. It was assumed that this modified bridge model did not differ significantly from the original bridge layout as far as the force was concerned. This was based on the postulations that the area of the pier obstructing the flow was comparatively small. Therefore, the frontal area of the bridge which exposed to wave pressure remained almost the same as in the original layout.

(a) Modified layout in experiment

(b) Original layout as in prototype

Figure 4.9 Front views of the modified and original bridge models

To study the realistic flow characteristics around the bridge prototype, the validated bridge model as discussed in the earlier section was changed to its original layout where the piers were located at both ends of the deck span. The actual bridge model was then subjected to the equivalent wave condition as in the model (nominal wave height = 8 m).

Figure 4.10 depicts the comparison of the force time histories of the simulation calculation and the result derived from the model test. The experimental result of forces on the bridge model is scaled up to the forces on the prototype with the scale factor of 10^6 (see Table 3.1). The force acting on the piers of bridge prototype is considerably smaller in the simulation model than the one recorded in the experiment because the effective frontal area of the piers that obstructs the flow in the actual prototype layout is 50 % smaller. However, both the model and prototype predict similar peak forces. Similar trend in the force time histories is observed, except for some slight phase shift in the second peaks.
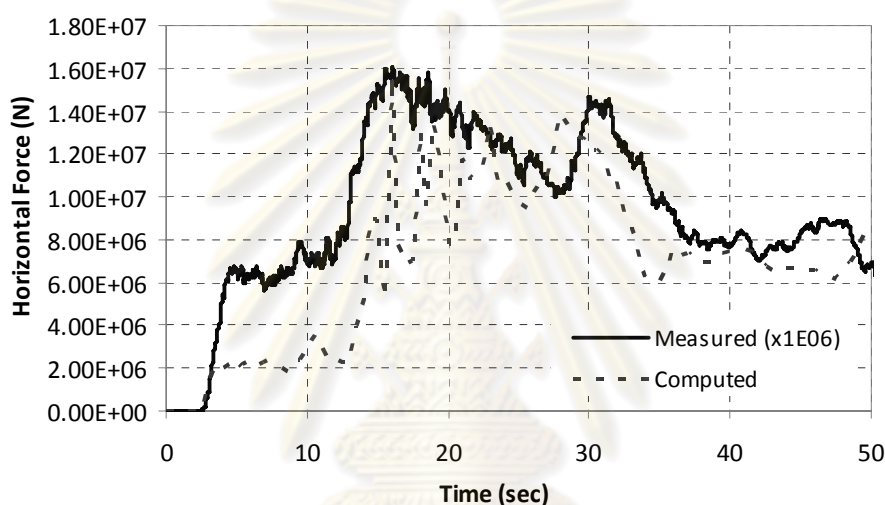

Figure 4.10 Comparison of force time histories of the scaled up experimental records and the simulated results

4.3.2 Bridge Deck Clearances

To investigate the influence of the bridge clearance, $h*$ (see Figure 4.9b), the bridge decks with various clearances were subjected to the same flow scenario, i.e. 8 m nominal wave height (H). Seven bridge prototypes, namely CR36, CR41, CR46, CR51, CR56, CR66 and CR76 which corresponded to deck clearance of 3.6 m, 4.1 m, 4.6 m, 5.1 m, 5.6 m, 6.6 m and 7.6 m, respectively, were investigated. The ratio of the deck clearance to the nominal flow depth ($h*/H$) ranges from 0.45 to 0.95.

4.3.2.1 Flow Field

Pressure intensity (shown in color tones) and velocity vectors at the end- (y = 45 m) and mid-span (y = 60 m) cross-section of the deck are presented. The results are

different due to the fact that the flow around the bridge prototype is completely three dimensional, which is caused mainly by the piers as will be elaborated further in the latter section. Hence, the results reflect the wave action at the locations near to and far from the pier, respectively. Figures 4.11 and 4.12 illustrate the flow field of one of the cases (i.e. CR56) in the study. The other cases are compiled in Appendix D. The simulated results are consistent with the expected wave phenomena: shorter time is needed for the wave to hit the bridge deck of smaller clearance. The wave pressure on the deck at the initial wave attack is inversely proportional to the deck clearance. In addition, the height of the upward splashing, the trajectory of the collapsing water column and the flow characteristics around bridge deck are also clearly shown.

When the wave approaches the bridge structure, a small portion of the leading wave front with shallow flow depth hits the pier with a high velocity. The wave in front of the pier is obstructed and it surges up the pier. This causes the incoming incident wave to override the preceding wave and hit the bridge deck although the incident flow depth is less than the deck clearance. It is demonstrated in Figure 4.12 where the wave only exists at the end span near the pier (y = 45 m). The wave splashes upward after hitting the deck and the height of the upward splashing is closely related to the deck clearance. The smaller the deck clearance is, the earlier and the higher the upward splashing are observed. This is caused by larger momentum contained at the leading wave. As a result, the water jet is pushed upward and collapses beyond the deck as shown in the cases of CR36, CR41 and CR46, where the deck clearance is lower than 58 % of the wave height. Once the flow drops beyond the deck, it collides on the wave and reflects to the back face of the deck. Large air pocket trapped around the deck is shown.

The frontal face of the deck, especially the area close to the protruded floor slab, is subjected to the highest wave pressure throughout the wave attacks. The wave impinges on the front face of the front girder with the highest magnitude of pressure at the initial wave attack on the deck. For intermediate girders, the wave hits the front face of the intermediate girders and it circulates to the back faces (in clockwise direction in the figure) of the girders in front of them at different rates. The pressures exerted on the intermediate girders are relatively small except at the initial wave attack. The wave then splashes vertically upward and this imposes a standing wave pressure on the parapets. At this instant of time, large air entrapment under the deck is observed. After that, the upward splash collapses, drops on the other end of the deck and flows on the deck in all directions. When the upward splash collapses on the floor slab, higher wave pressure exerts on the

area near to the back parapet. The wave fills the compartment formed by intermediate girders and exerts almost similar pressure to every face of each compartment. Generally, the incoming wave that propagates horizontally towards the deck is separated by the deck and merged at some distances behind the deck. At the confluence point at the back of the deck, the flow reverses and attacks the back face of the deck after some time and forms vortex. Large amount of the wave overtops the deck and imposes large additional gravity force on it.

4.3.2.2 Pressure Distribution

Figure 4.13 presents the vertical distribution of the horizontal pressures on the frontal face of the bridge deck (girder and parapet) for various deck clearances. The distributions shown are the distributions at the end-span near to the pier and at the mid-span of the deck. As the unique configuration of the I-beam girder deck where the parapets are protruded from the girders, the pressure distribution discontinues at the slab level ($z/H = 0.8875$ for CR56). Horizontal distributions of the horizontal pressures along the mid heights of the front girder and parapet are plotted on the left and right of Figure 4.14. The pressures are normalized with the hydrostatic pressure at 8 m nominal wave height. Due to the symmetrical orientation of the deck, the pressure distribution of one half of the deck with the pier located on the left side is shown.

As anticipated, the higher the deck, the smaller the maximum pressure is attained. The maximum normalized pressure of larger than 4 is observed for CR36 and CR41 while the normalized pressure for CR66 is below 2. At the initial wave attack, only the front face of the front girder is subjected to almost uniform pressure. Thereafter, the wave flows through the deck and it exerts uniform pressure over the height of the front face of the front girder and the front parapet (except near to the free ends at the top and bottom of the deck) especially when the wave becomes nearly steady (about second 40). The horizontal distribution of the horizontal pressures along the mid height of the girder is not uniform at the initial wave impingement for higher deck heights. Higher wave pressure at the deck portion near to the bridge pier is recorded due to the upward splash from the pier at the earlier stage of wave attack. This indicates that the flow around the bridge model is highly three dimensional at that instant of time.
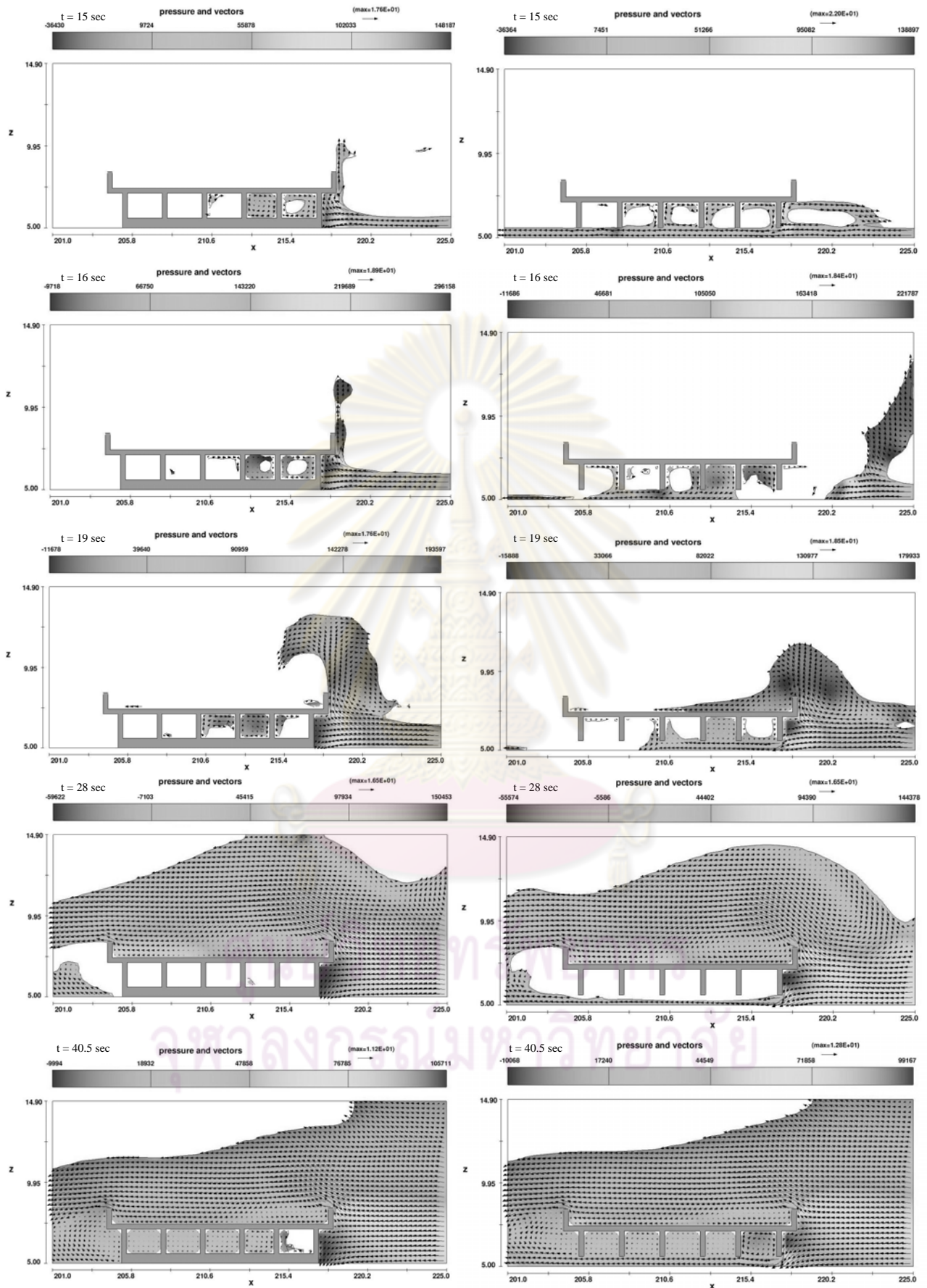
Figure 4.11 Pressure (color) and flow velocity (vector) for CR56 at the (left) end-span
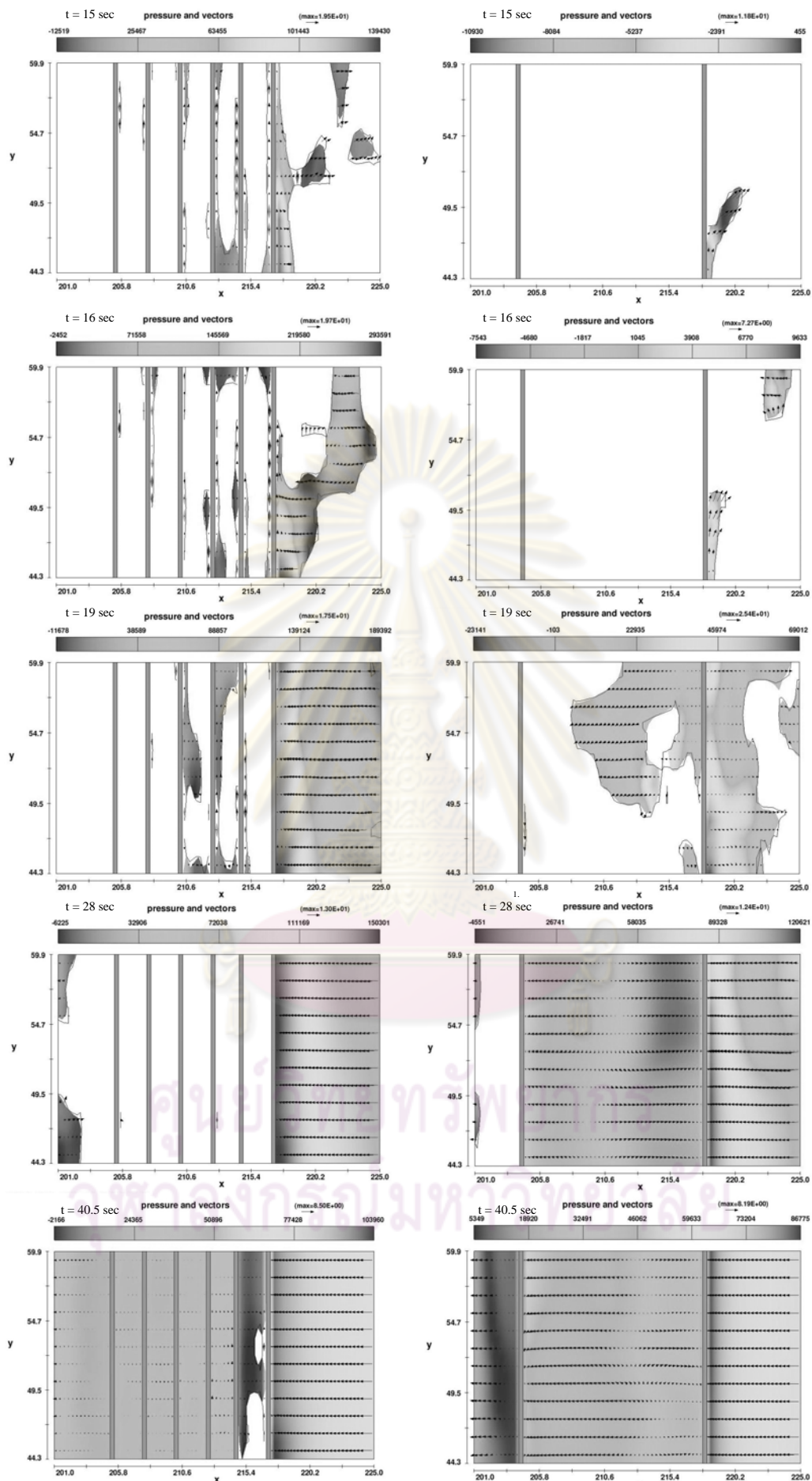and (right) mid-span

Figure 4.12 Pressure (color) and flow velocity (vector) of CR56 along the mid-height of the (left) front girder and (right) front parapet
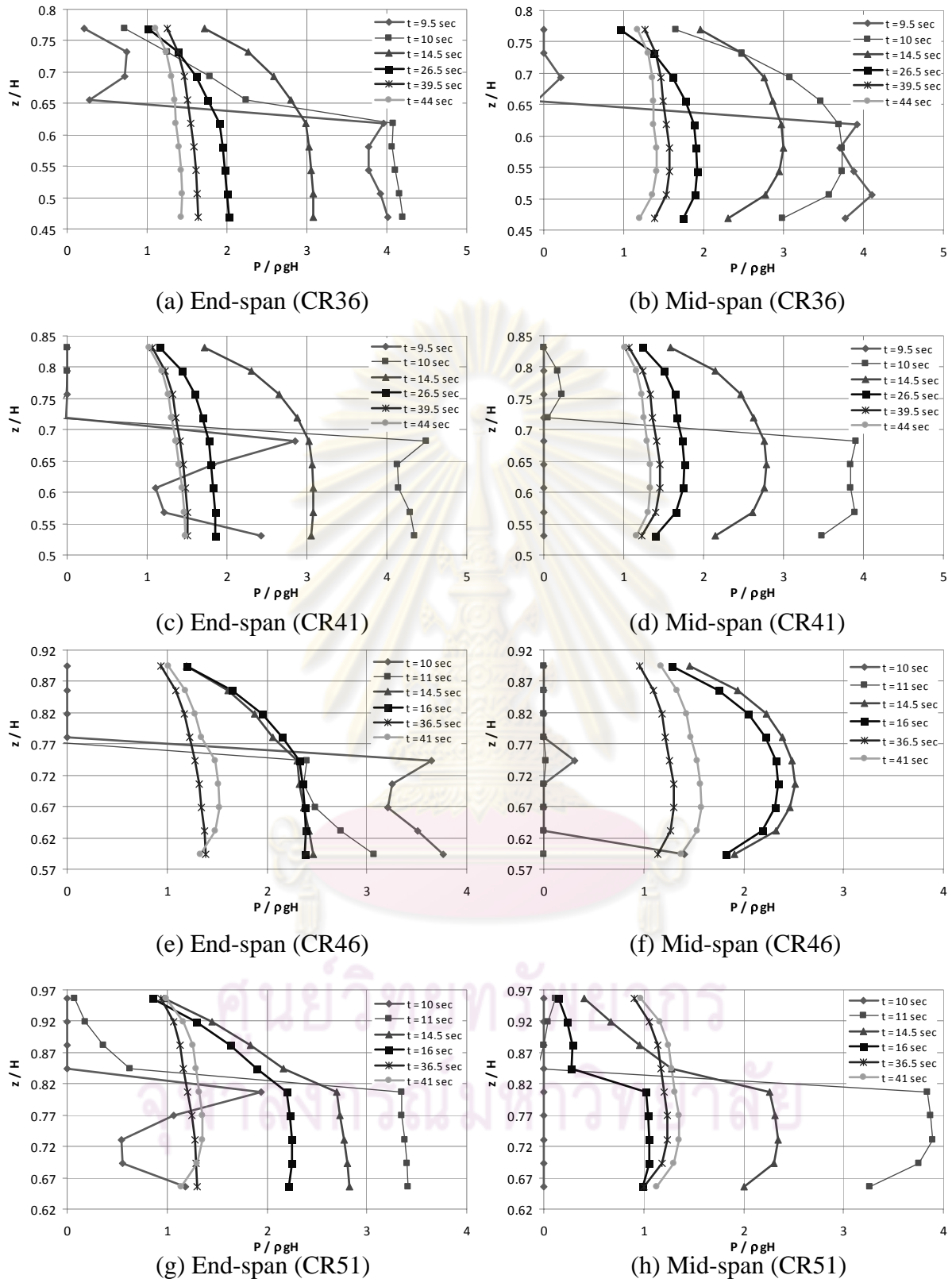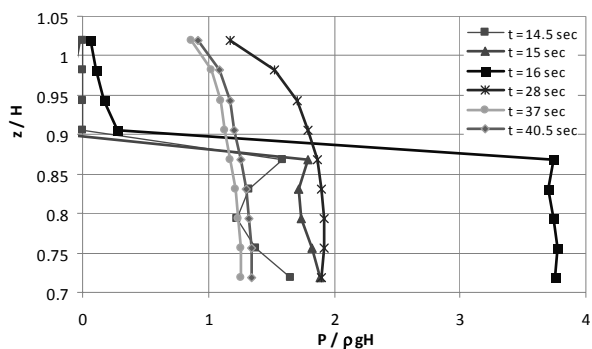
(a) End-span (CR36)

(b) Mid-span (CR36)

(c) End-span (CR41)

(d) Mid-span (CR41)

(e) End-span (CR46)

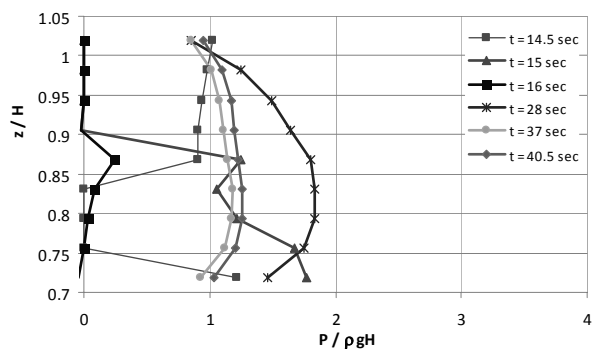(f) Mid-span (CR46)
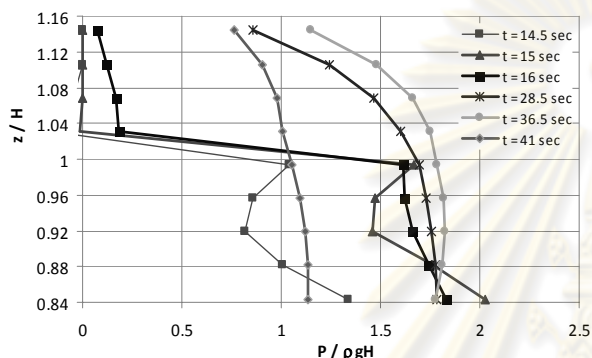
(g) End-span (CR51)

(h) Mid-span (CR51)

Figure 4.13 Vertical distribution of the horizontal pressures on frontal face of deck at the end-span and the mid-span of the deck for different deck clearances
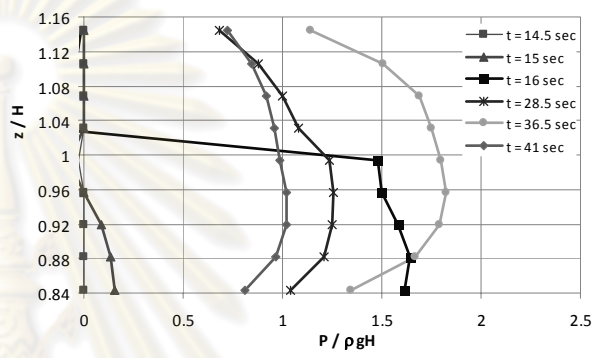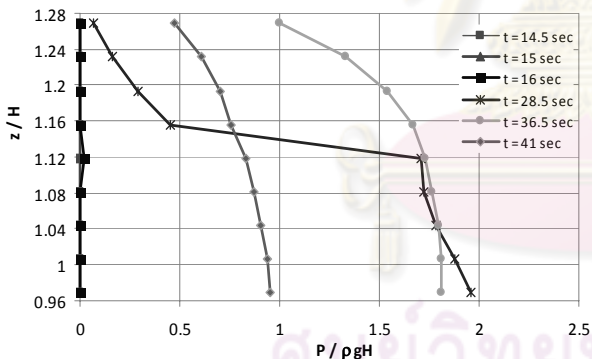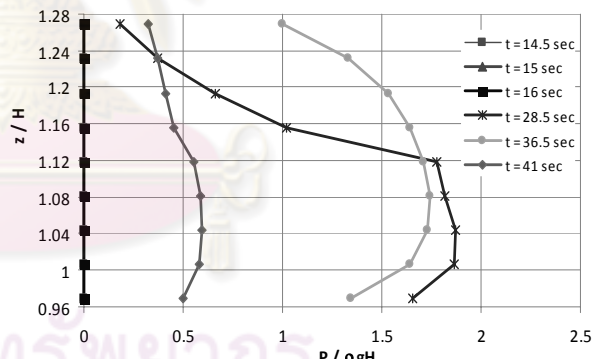
(i) End-span (CR56)
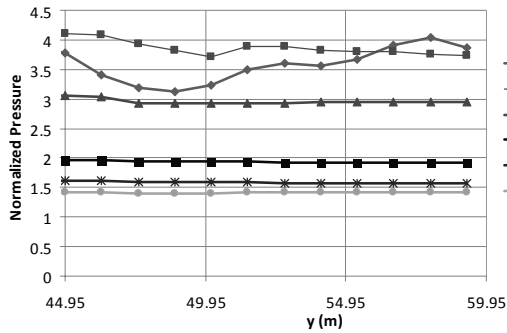
(j) Mid-span (CR56)

(k) End-span (CR66)

(l) Mid-span (CR66)

(m) End-span (CR76)

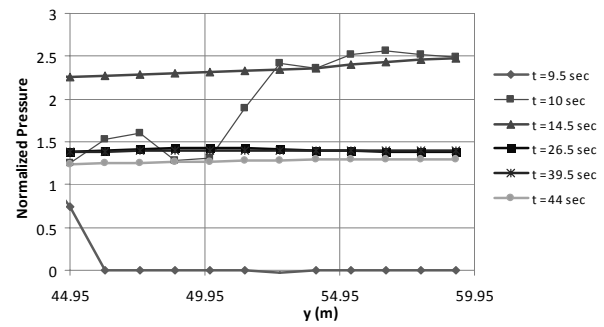(n) Mid-span (CR76)
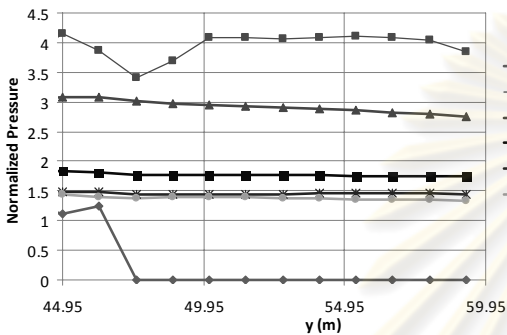
Figure 4.13 (Cont'd)

(a) Front girder (CR36)

(b) Front parapet (CR36)

(c) Front girder (CR41)

(d) Front parapet (CR41)

(e) Front girder (CR46)

(f) Front parapet (CR46)

(g) Front girder (CR51)

(h) Front parapet (CR51)

Figure 4.14 Horizontal distribution of the horizontal pressures on frontal face of deck
along the mid-height of the front girder and the front parapet

(i) Front girder (CR56)

(j) Front parapet (CR56)
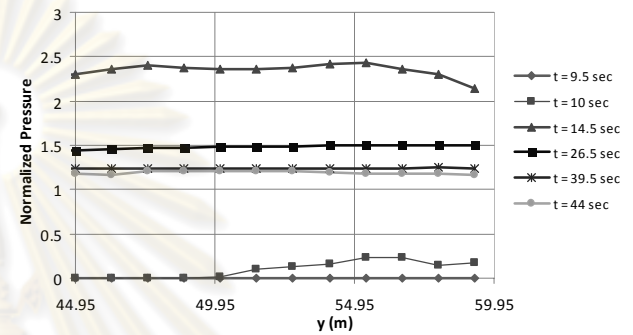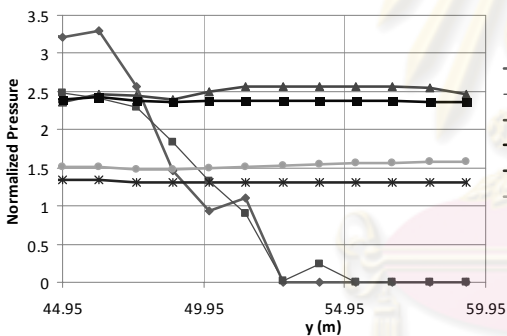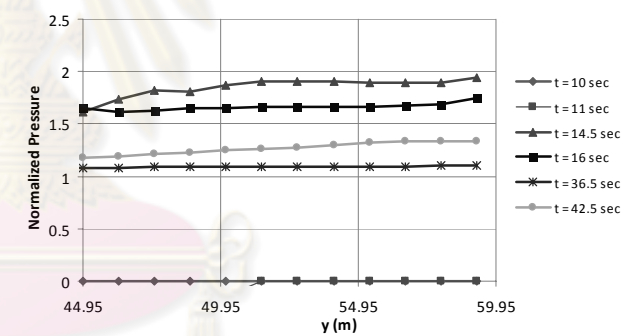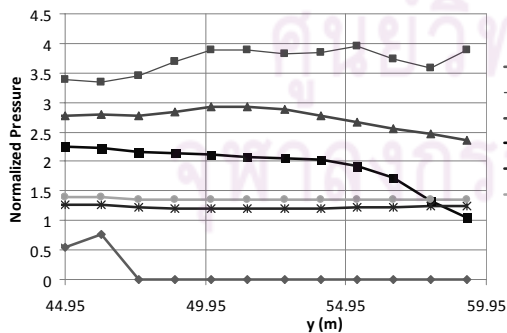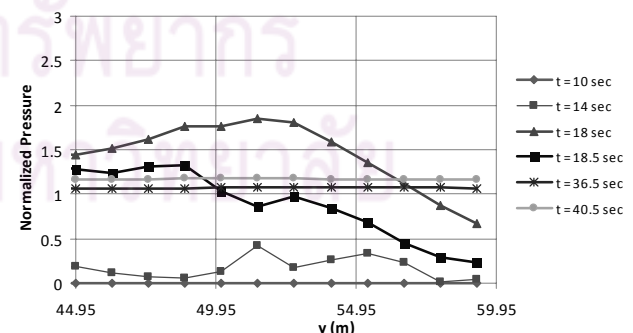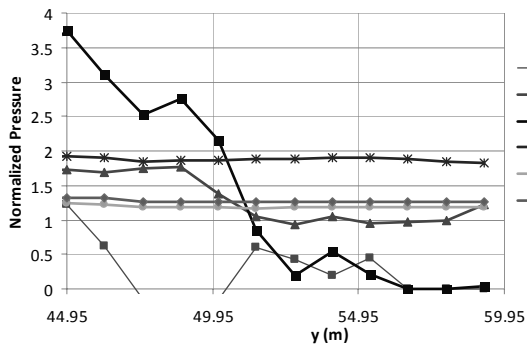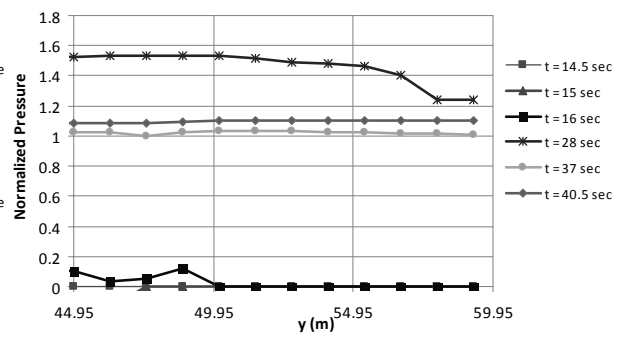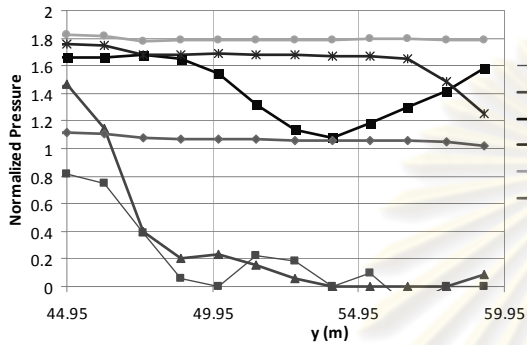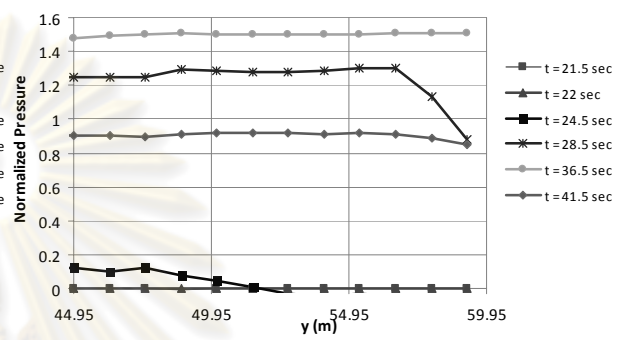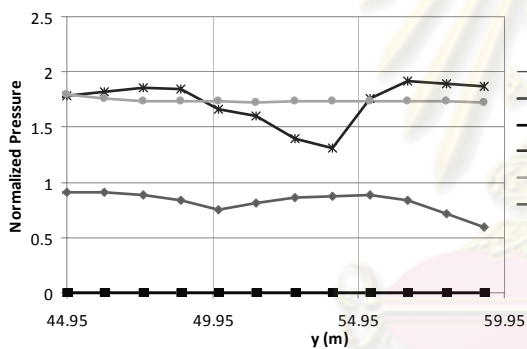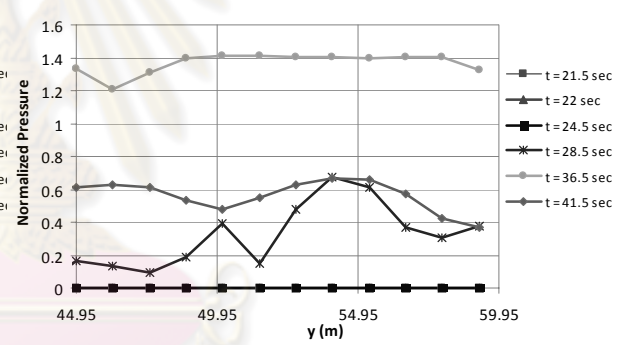

(k) Front girder (CR66)

(l) Front parapet (CR66)

(m) Front girder (CR76)

(n) Front parapet (CR76)

Figure 4.14 (Cont'd)

4.3.2.3 Forces

Time histories of total horizontal and vertical forces at 8 m nominal wave height are presented in Figure 4.15. The positive sign in the horizontal force refers to the force in the flow direction while the positive and negative signs in the vertical force represent the vertical uplift and the additional gravity force, respectively. The horizontal force can be generally characterized into two types, i.e. peak force and slow-varying force; the latter is adopted from Douglass et al. (2006) as depicted in Figure 4.16. The force is first recorded for CR36, followed by CR41, CR46, CR51, CR56, CR66 and CR76. The peak horizontal forces vary substantially from case to case up to second 20 except the cases of CR66 and CR76 where practically no horizontal forces are recorded in the first 20 seconds. The peak horizontal forces obtained for CR36 (second 10), CR41 (second 14.5), CR46 (second 14.5), CR51 (second 16) and CR56 (second 16) mark approximately 2 to 3 times the slowly-varying forces (Table 4.4). As opposed to the peak forces, all the cases (except CR76) experience similar horizontal slowly-varying forces regardless the deck clearance after second 35, i.e. about 7 MN.

Vertical force time histories exhibit different trends. The vertical uplift force (F_{v+}) is first exerted on the deck and it is followed by the additional gravity force (F_{v-}) when the wave falls on the deck. The uplift force is denoted as positive value whereas the additional gravity force is denoted as negative value in the computation. CR36 and CR46 show longer period of vertical uplift force action up to second 34. This is due to the water jet (that is pushed upward) drops beyond the deck. For the case of CR41, the water jet is pushed almost uprightly and it drops on the deck soon after. The maximum vertical uplift forces attained are 3.8 MN (CR66) to 18.5 MN (CR46) as listed in Table 4.4. CR66 and CR76 experience relatively smaller vertical uplift force as their clearances are larger than the other cases. As exhibited in the horizontal force, the variation of the vertical force is not significant after second 35, where the wave with much higher flow depth flows through the bridge deck at nearly steady state. The maximum additional gravity force marks about 21 MN which is 3 times the horizontal slowly-varying force.
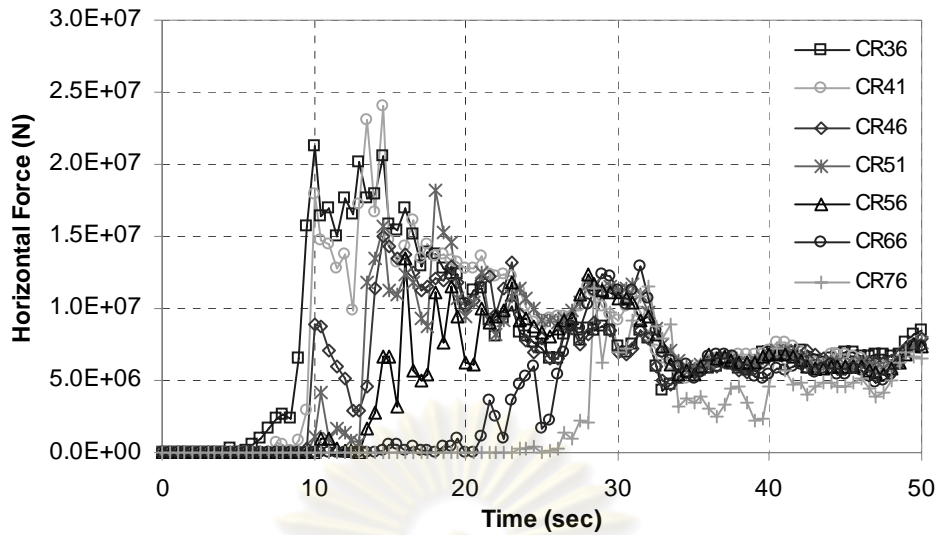
(a) Horizontal force
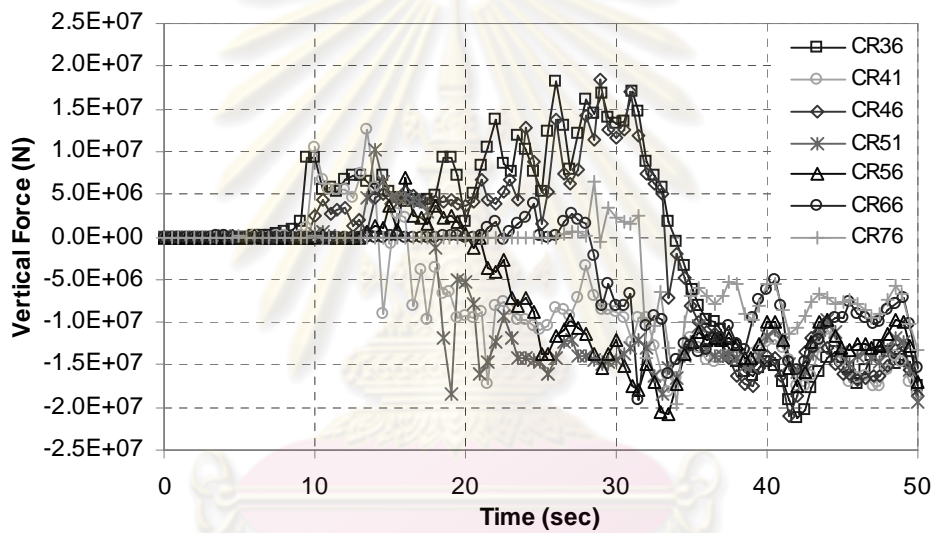
(b) Vertical force

Figure 4.15 Total deck force time histories of the horizontal and vertical force

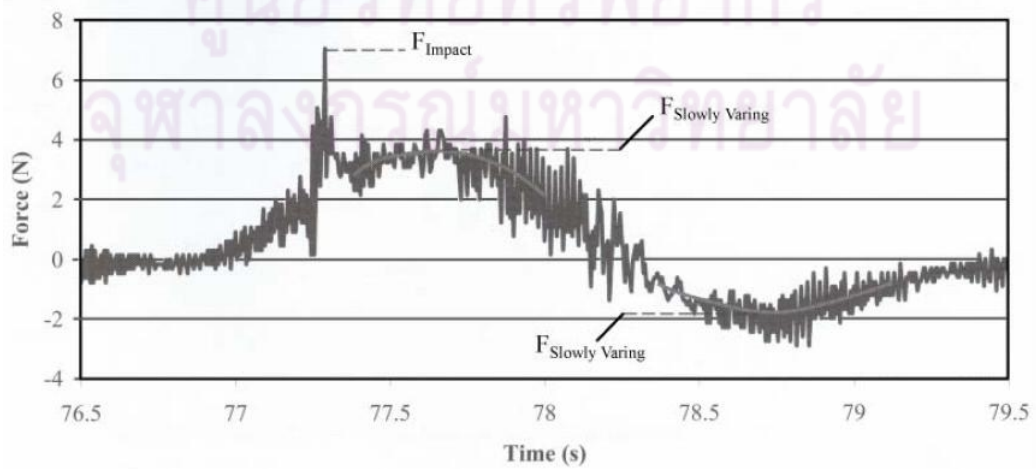components at 8 m nominal wave height

Figure 4.16 Definition of the slowly-varying force (Douglass et al., 2006)

Table 4.4   Summary of the maximum horizontal and vertical forces

Cases	Deck Clearance (m)	Horizontal Force				Vertical Force			
		Time (sec)	Peak Force (MN)	Time (sec)	Slowly-Varying Force (MN)	Time (sec)	Uplift Force (MN)	Time (sec)	Additional Gravity Force (MN)
CR36	3.6	10	21.3	39.5	6.9	26	18.1	42	21.3
CR41	4.1	14.5	24	40.5	7.6	13.5	12.5	33.5	18.3
CR46	4.6	14.5	15	42.5	7.1	29	18.5	41.5	20.9
CR51	5.1	16	12.3	40.5	7.0	14	13.5	33	18.5
CR56	5.6	16	13.5	40.5	6.8	16	6.9	33.5	20.7
CR66	6.6	31.5	12.9	41.5	5.9	24.5	3.8	31.5	19.1
CR76	7.6	32	11.6	43	4.6	28.5	6.5	34	19.6

4.3.3 Simplification of Bridge Deck Configurations

In previous studies, bridge decks comprising complex configurations such as I-beam girder decks were usually simplified to a regular form in order to make them feasible in the construction of the physical models. These have been done in Kataoka et al. (2006), Shoji and Mori (2006) and Ikari and Gotoh (2007) in which 3D rectangular box type bridge girders, with and without opening at the bottom, were used. Furthermore, Kataoka et al. (2006) and Iemura et al. (2007) excluded the piers in their physical modeling while Nimmala et al. (2006) adopted a 2D rectangular box type bridge deck without the piers.

It is interested to know how these simplified bridge decks behave under tsunami wave attacks and how accurate are the results as compared to the actual prototype. Thus, three types of simplified bridge prototypes (Figure 4.17) are considered for the bridge configuration used in this study, i.e. rectangular solid box type bridge deck, 3D I girder deck without piers and 2D I girder deck without piers. They are respectively denoted as Box, 3D Deck and 2D Deck hereafter. For the purpose of comparison, all these bridge deck configurations have the same projected areas with the actual target bridge prototype in the vertical and horizontal planes. The results are discussed in the following sections.

(a) 3D Box model

(with piers, half span is shown)

(b) 3D Deck model

(without piers, half span is shown)

(c) 2D Deck model (without piers)
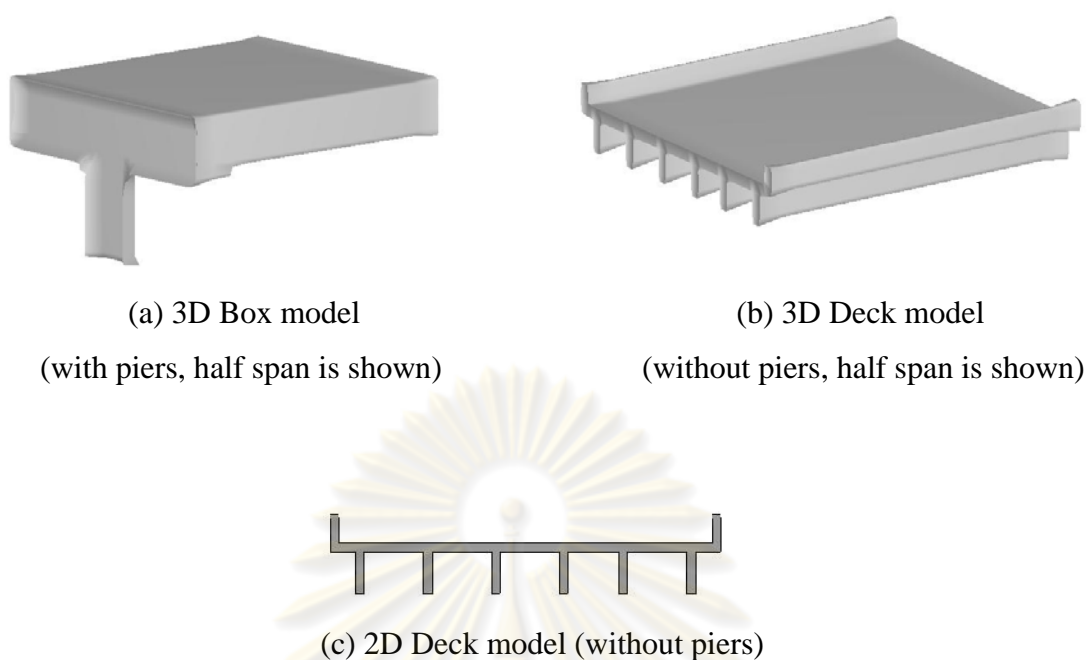
Figure 4.17 Simplified bridge prototype configurations

4.3.3.1 Flow Field

Figures 4.18 to 4.22 compare the pressure and velocity vector of various bridge prototypes at selected time domains. The cross-sectional views at the end- and mid-span sections of the deck are illustrated. Because the flow is not uniformly distributed throughout the width of the deck, these two sectional views are shown to represent the wave action at the locations near to and far from the piers, respectively. The pier is located at y = 45 m in the computational model.

Comparing the simulated results of the simplified deck configurations (Figure 4.18 to 4.22) with the one of the original layout, CR56 (Figure 4.11), the bridge prototype with the original layout demonstrates high wave pressure at the front girder at second 15 with substantial upward splashing of the wave. Also displayed is the wave impingement on the intermediate girders at that instant of time. All the simplified configurations of the bridge deck (Figures 4.18 to 4.22) are practically not able to predict these phenomena. This indicates that the initial wave attack on the deck is closely related to the upward splashing of the wave after hitting the pier. Except for the bridge deck with the box girder, the wave conditions for the actual and simplified bridge deck configurations do not differ significantly after second 20.
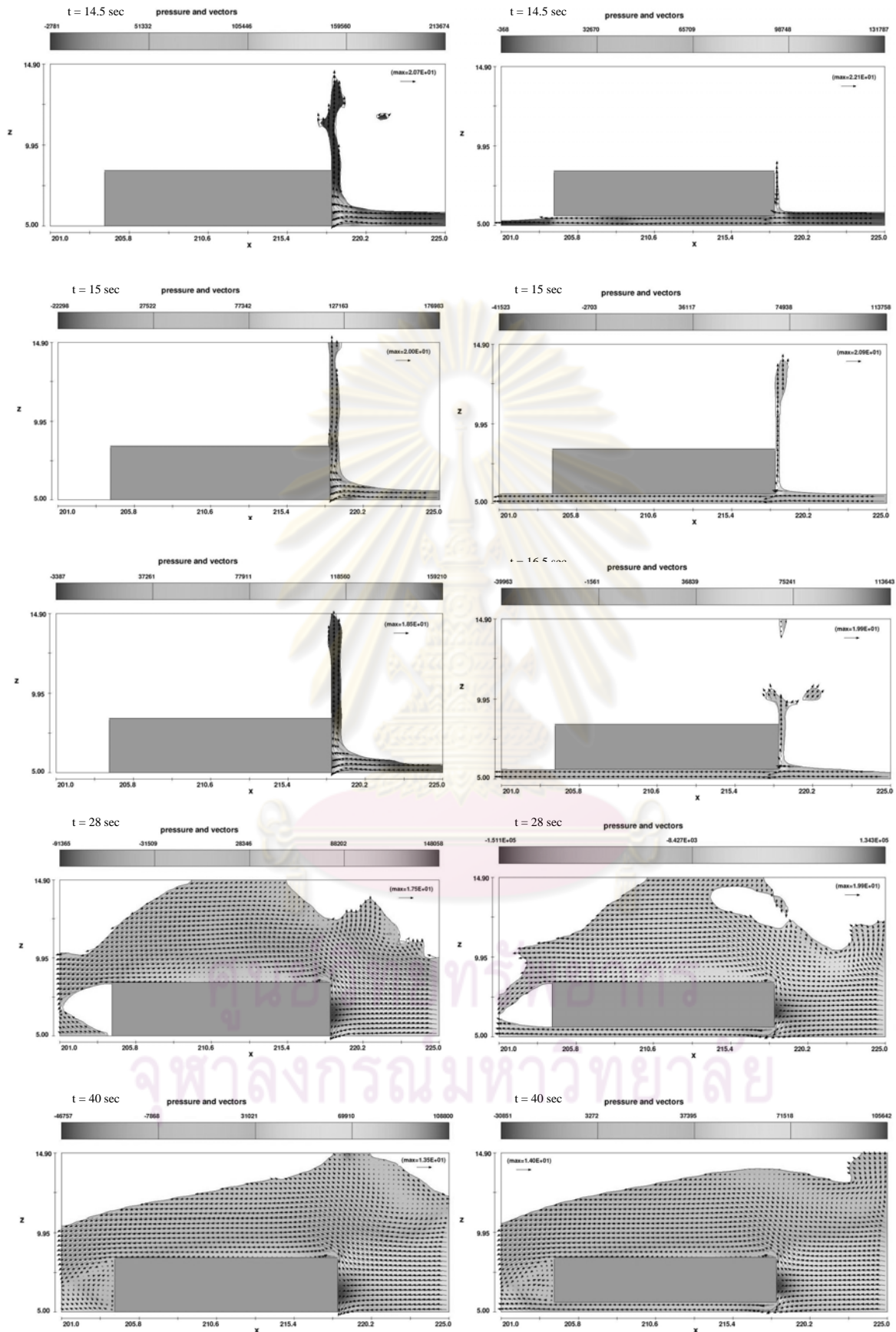
Figure 4.18 Pressure (color) and flow velocity (vector) of the prototype with Box
configuration at the (left) end-span and (right) mid-span
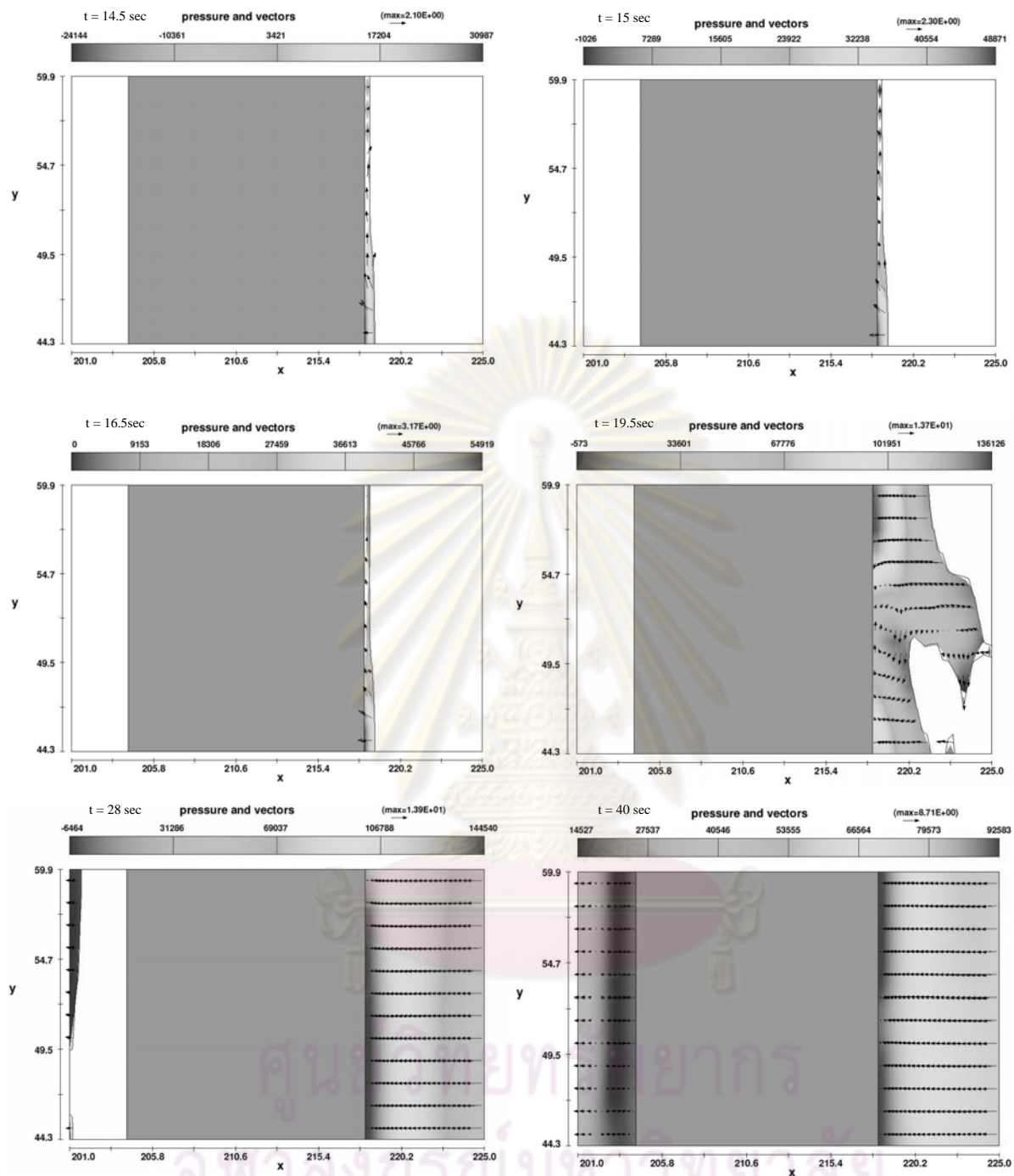
Figure 4.19 Pressure (color) and flow velocity (vector) of the prototype with Box configuration along the mid-height of the deck
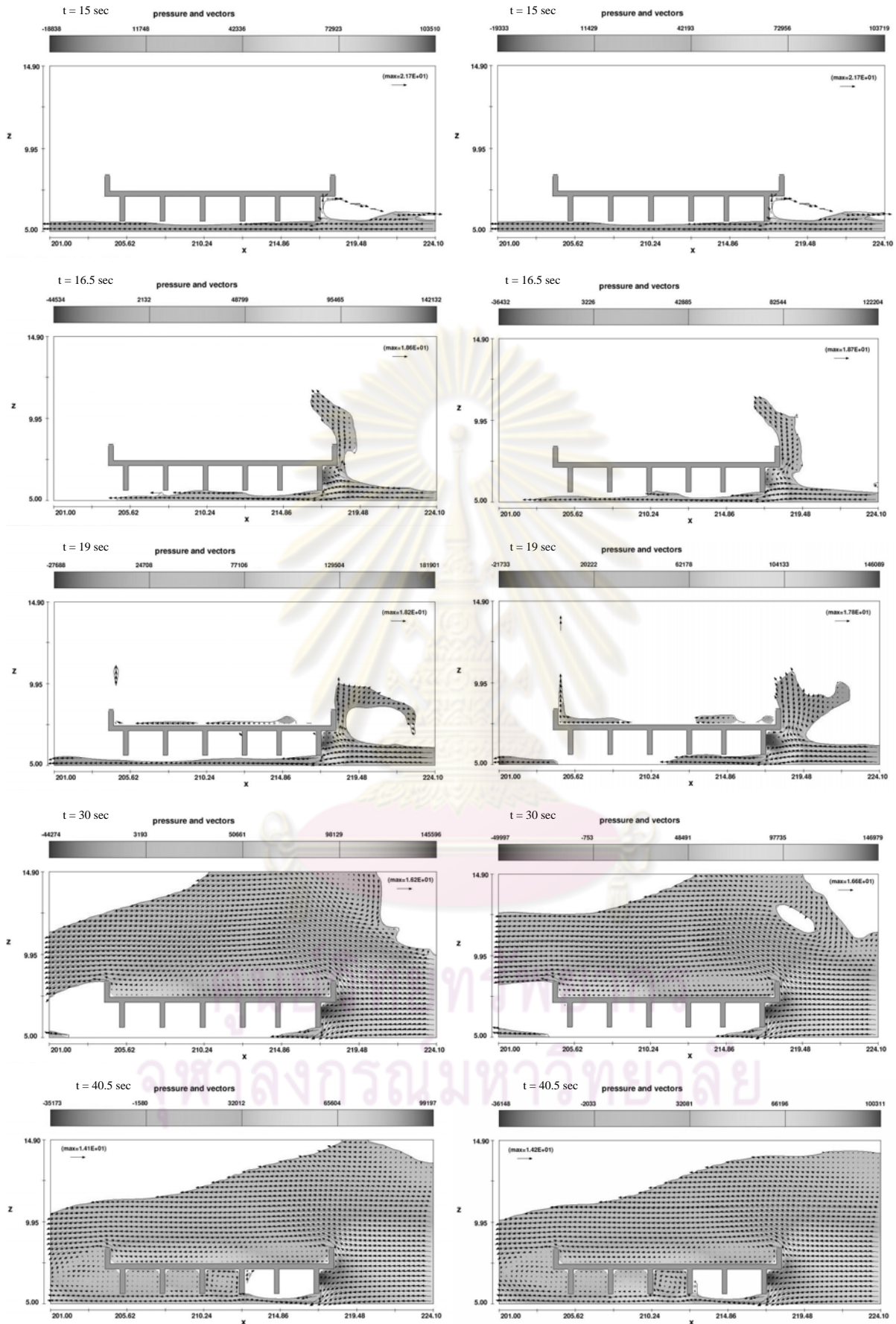
Figure 4.20 Pressure (color) and flow velocity (vector) of the prototype with 3D Deck

configuration at the (left) end-span and (right) mid-span
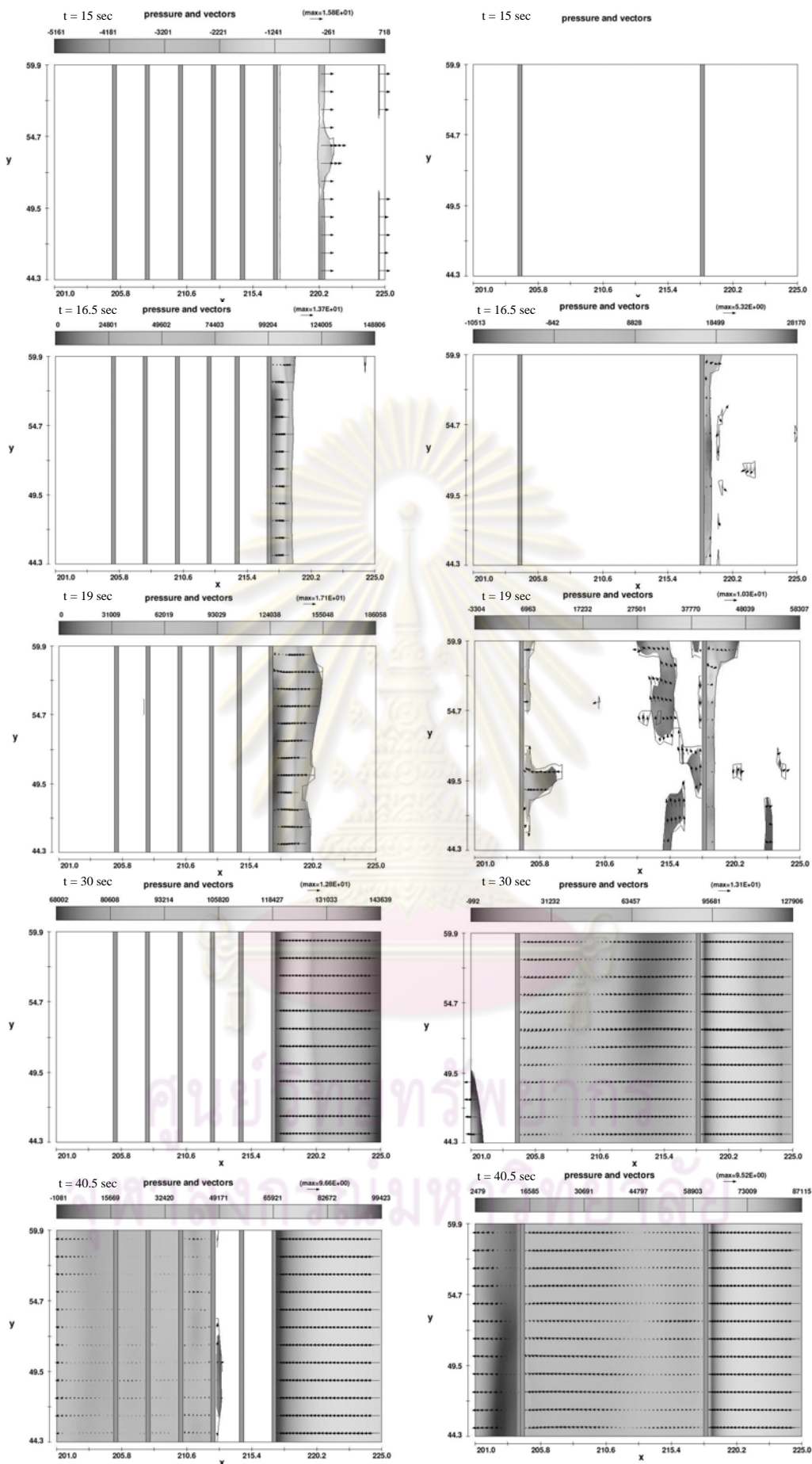
Figure 4.21 Pressure (color) and flow velocity (vector) of the prototype with 3D Deck

configuration along the mid-height of the (left) front girder and (right) front parapet
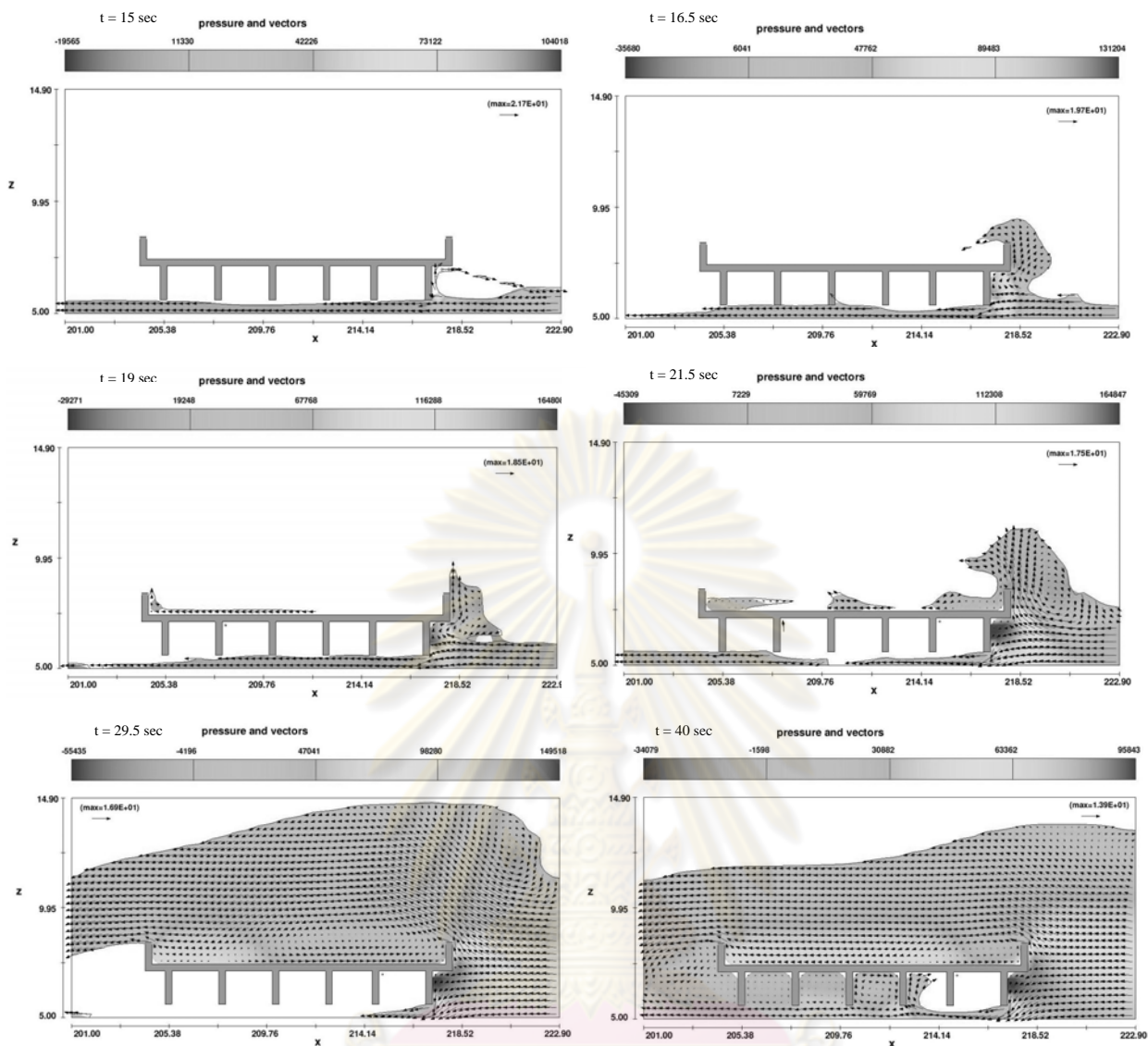
Figure 4.22 Pressure (color) and flow velocity (vector) of the prototype with 2D Deck configuration

4.3.3.2 Pressure Distribution

The vertical distributions of the horizontal pressures along the height at various time steps are plotted in Figure 4.23. The vertical distributions at the end- and mid-span of the decks are shown in the left and right of the figure. In the figure, the wave pressure is normalized with the hydrostatic pressure at the nominal flow depth of 8 m. Discontinuity of the pressure distribution is observed at $z/H = 0.8875$, where the front parapet is out of the front girder plane.

At the initial wave impingement on the deck, the front girder is exerted with higher wave pressure as compared to the wave pressure at the front parapets. The results reveal that the simplified deck configurations underestimate the pressure on the front

girder. The normalized pressure of about 4 is predicted for the deck with the original layout (Figure 4.13) whereas all the simplified deck configurations estimate the normalized pressure less than 2.5.

The distributions of horizontal pressures along the mid-height of the front girder (3D Deck) and front deck (for Box) are presented in Figure 4.24.

(a) End-span (Box)

(b) Mid-span (Box)

(c) End-span (3D Deck)

(d) Mid-span (3D Deck)

(e) 2D Deck
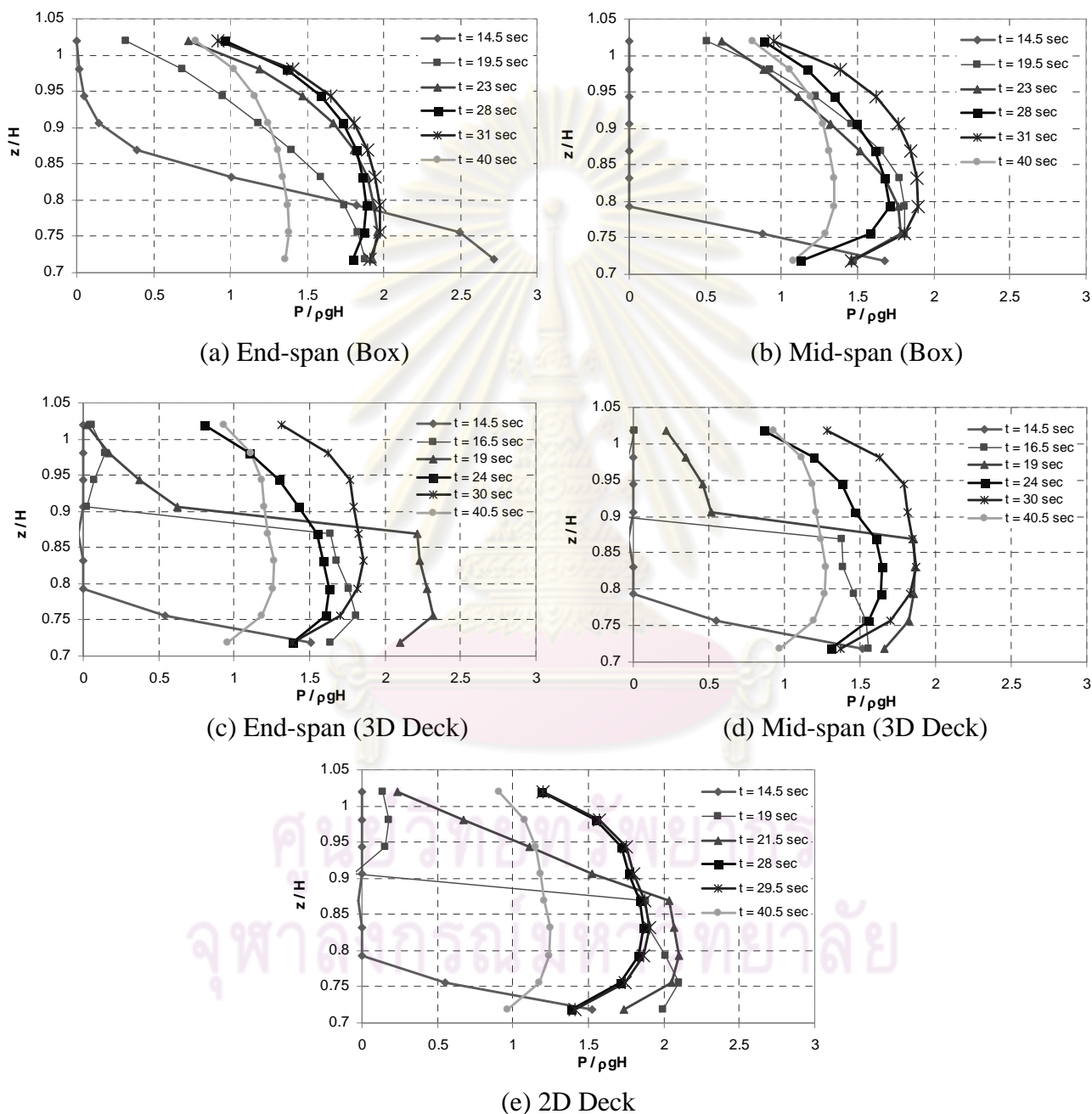
Figure 4.23 Vertical distributions of horizontal pressures at the end-span and mid-span of the deck frontal face
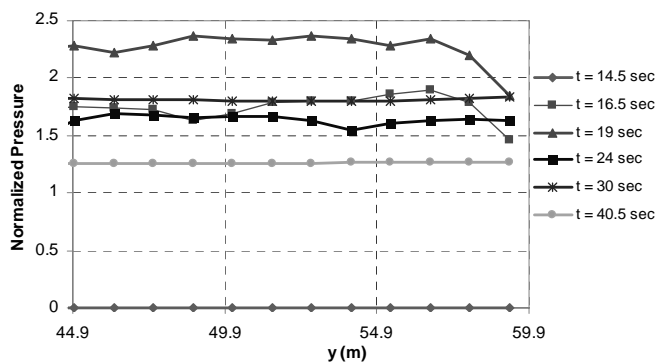
(a) Mid-height of the deck (Box)
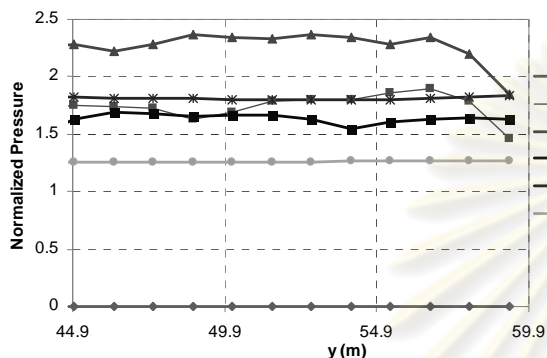
(b) Mid-height of the front girder
(3D Deck)
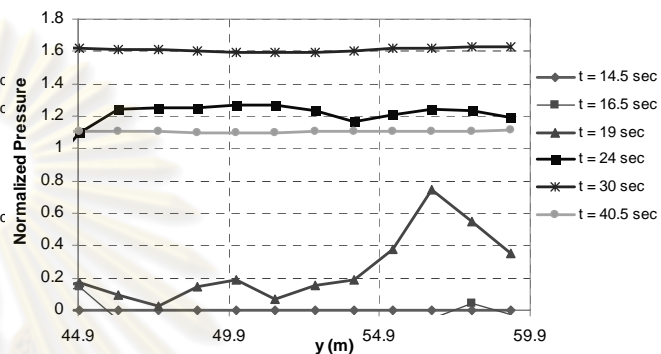
(c) Mid-height of the front parapet
(3D Deck)

Figure 4.24 Horizontal pressure distributions on the frontal face of deck

4.3.3.3 Forces

Figure 4.25 shows the simulated results of the total horizontal and vertical forces on the deck. As mentioned in earlier sections, the forces are categorized into peak and slowly-varying forces. Under the similar wave scenarios on various bridge deck configurations, the maximum peak forces in horizontal force component vary in the range of 4 MN to 13.5 MN. It is noticed that none of the simplified bridge prototypes can predict the peak forces accurately at the initial wave attack (up to second 20). After second 20, the variation of the total horizontal forces is not significant for all the cases. The vertical uplift is exerted on the deck at the initial wave attack and it is followed by the additional gravity force where the wave overtops the deck. The maximum vertical uplift and additional gravity forces predicted by CR56 are about 7 MN and 20 MN, respectively. Similar to the total horizontal force, the simplified bridge prototypes can not predict well the vertical uplift forces of the actual bridge prototype. Though the additional gravity forces do not start at the same time, all the bridge deck configurations estimate almost the similar magnitude of this load.

Comparing 3D Deck and 2D Deck models where the piers are neglected, there is no significant difference of the forces acting on the deck in both horizontal and vertical components. If the piers are taken into consideration in the model but the I-beam girder bridge deck is simplified as a box-shape deck, much lower peak force at the initial wave impingement in which the flow is highly unsteady (less than second 20) is obtained. Much lower vertical uplift force is also observed. This can be explained by the reduction of the horizontal force contributed from the intermediate girders and the reduction of the vertical uplift force contributed from the protruded slab. Table 4.5 summarizes the comparison of the force for the actual and the simplified bridge models.
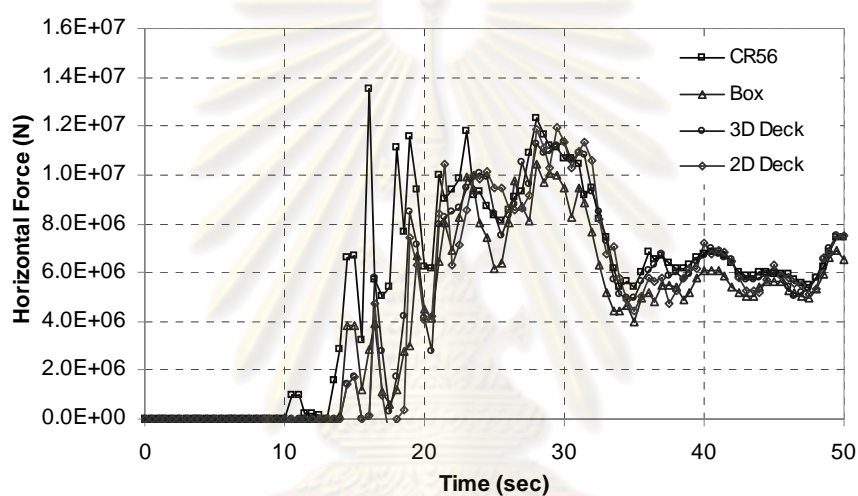
(a) Horizontal force
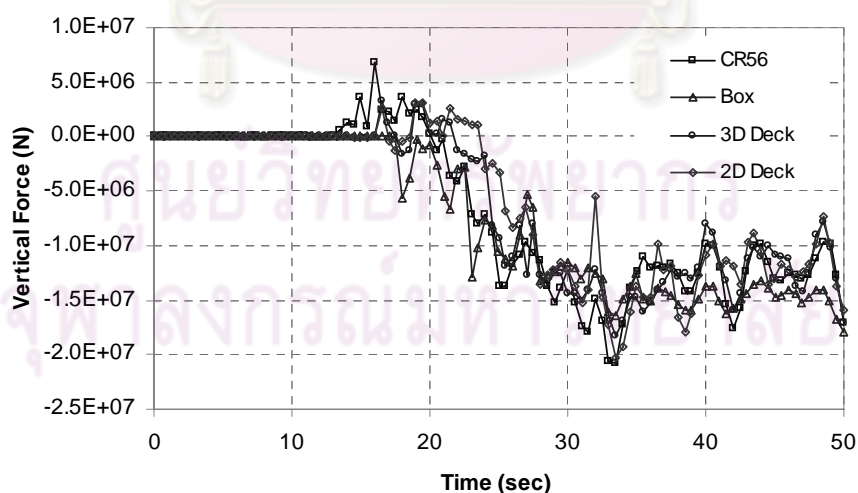
(b) Vertical force

Figure 4.25 Total force time histories of the horizontal and vertical force components

Table 4.5   Comparison of the peak horizontal and vertical uplift forces for the actual and simplified models

Cases	Peak Horizontal Force			Vertical Uplift Force		
	Time (sec)	Peak Force, F_h (MN)	$F_h/F_{h,CR56}$	Time (sec)	Uplift Force, F_{v+} (MN)	$F_{v+}/F_{v+,CR56}$
CR56	16	13.5	1.00	16	6.9	1.00
3D Box	28	10.4	0.77	14.5	0.05	0.01
3D Deck	30	11.4	0.84	16.5	3.2	0.46
2D Deck	29.5	12	0.89	19	3.2	0.46

4.3.3.4 Summary

Different deck configurations exhibit distinct characteristics of the flow around the bridge deck especially at the initial wave impingement. For the considered cases, none of the simplified configurations can predict the peak horizontal force and the maximum vertical uplift force up to the accurate level. The simulated peak values of the simplified configurations are less than the one predicted in the actual prototype layout. This indicates a complete pier-deck configuration of the I-beam girder bridge deck should be considered in order to accurately predict the peak horizontal force and the vertical uplift force at the initial wave attack on the deck.

CHAPTER V

ESTIMATION OF TSUNAMI FORCES ON BRIDGE DECKS

This chapter discusses tsunami forces on bridge decks estimated from the results of numerical simulation for bridge prototypes with seven different deck clearances. A method for estimating tsunami forces is proposed. The effects of perforated bridge deck in reducing tsunami forces are discussed in the last section.

5.1 Wave Forces on Bridge Deck

Due to the fact that bridge damage may be caused by a partial or complete wash-away of the decks from the bridge abutments as witnessed in the 2004 Indian Ocean tsunami, an accurate prediction of the tsunami drag force on the deck is crucial for the structural design of the components of the deck system against such failure. Both horizontal and vertical forces are computed in the numerical analysis. Horizontal forces are categorized into peak and slowly-varying forces whereas vertical forces are categorized into uplift and additional gravity forces.

5.1.1 Horizontal Slowly-Varying Forces

One of the important observations shown in the force time-histories is the independency of the slowly-varying forces from the deck clearance as shown in Figure 4.16. This argument holds if h^*/H is below 0.95 where the deck clearance is less than 7.6 m. The horizontal pressure distributions of the slowly-varying forces on bridge decks under 8 m nominal wave heights are presented in Figures 5.1 for all the seven clearances studied. At the moment the slowly-varying force acts on the front face of the deck, the back face of the deck is subjected to the wave as well. Front and back face pressure distributions are presented. The mean values are determined from the linear least squares regression. Also plotted are the values of mean plus 1 standard deviation (mean + 1SD) and mean plus 2 standard deviations (mean + 2SD) corresponding to 68 % and 95 % percentiles, respectively. The mean pressure distribution on the front face of the deck (Figure 5.1a) marks $2.48\rho gH$ at the ground level and decreases linearly to zero at $1.64H$. The mean pressure distribution of the wave at the back face of the deck is shown in

Figure 5.1b where the triangular distribution of $0.96\rho gH$ at the ground level and zero at $1.12H$ are obtained. It is interesting to note that the wave pressure at the back face of the deck is almost similar to the hydrostatic pressure. By subtracting the back face pressure from the front face pressure, the net dimensionless horizontal pressure acting on the bridge deck (Figures 5.1c) is determined. The net horizontal pressure (p) at any height of the point of interest that is measured from the ground level (z) can be expressed in the bilinear relationships as follows,

For mean,

$$p = \rho gH (2.3246 - z/H) / 1.5302, \qquad 0.4 \le z/H \le 1.12 \qquad \text{(5.1a)}$$
$$p = \rho gH (1.642 - z/H) / 0.6626, \qquad 1.12 \le z/H \le 1.3 \qquad \text{(5.1b)}$$

For mean + 1SD,

$$p = \rho gH (2.4168 - z/H) / 1.5302, \qquad 0.4 \le z/H \le 1.16 \qquad \text{(5.1c)}$$
$$p = \rho gH (1.7024 - z/H) / 0.6626, \qquad 1.16 \le z/H \le 1.3 \qquad \text{(5.1d)}$$

For mean + 2SD,

$$p = \rho gH (2.5093 - z/H) / 1.5302, \qquad 0.4 \le z/H \le 1.19 \qquad \text{(5.1e)}$$
$$p = \rho gH (1.7628 - z/H) / 0.6626, \qquad 1.19 \le z/H \le 1.3 \qquad \text{(5.1f)}$$

Eq. (5.1a) to Eq. (5.1f) are used to calculate the forces acting on the bridge decks with various clearances. The estimated forces are then compared with the numerical simulation results as shown in Table 5.1. Also shown are the estimation errors of the predicted forces by Eq. (5.1) as compared to the simulated forces. The positive value of the error denotes the prediction overestimates the simulation result and vice versa. Except for the cases which the decks are placed at extreme low and high positions (CR36 and CR76), the results indicate that the mean + 2SD pressure distribution can serve as the upper bound for the slowly-varying forces.

The correlation between the slowly-varying forces and the ratios of the wave height above the deck soffit to the nominal wave height (h_{max}-h^*/H) at slowly-varying force region are shown in Figure 5.2. The definition of (h_{max}-h^*) is illustrated in Figure 5.3. A linear relation with very gentle slope is obtained.
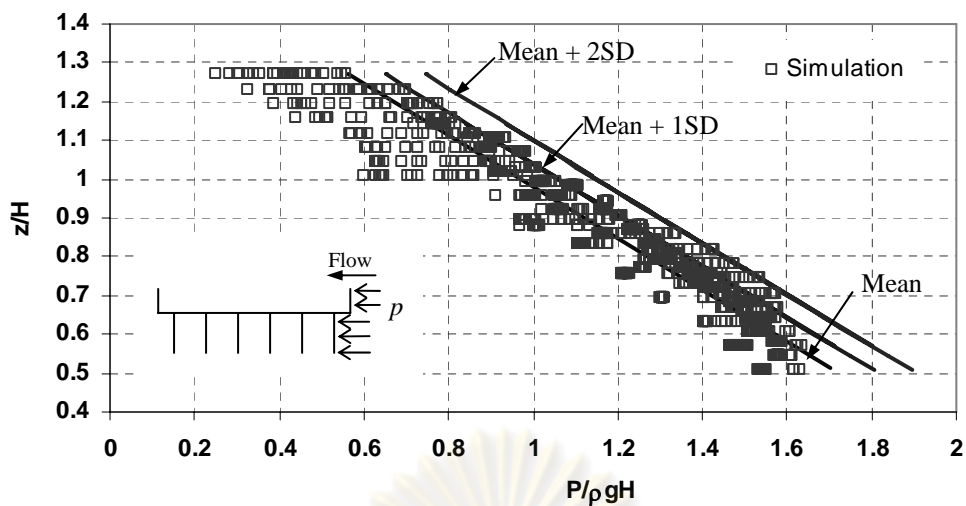
(a) Front face horizontal pressure on bridge deck
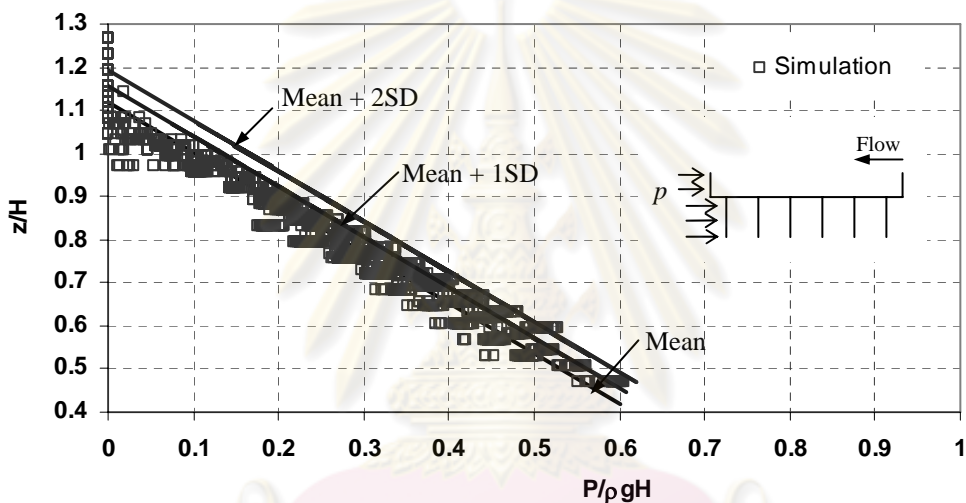
(b) Back face horizontal pressure on bridge deck
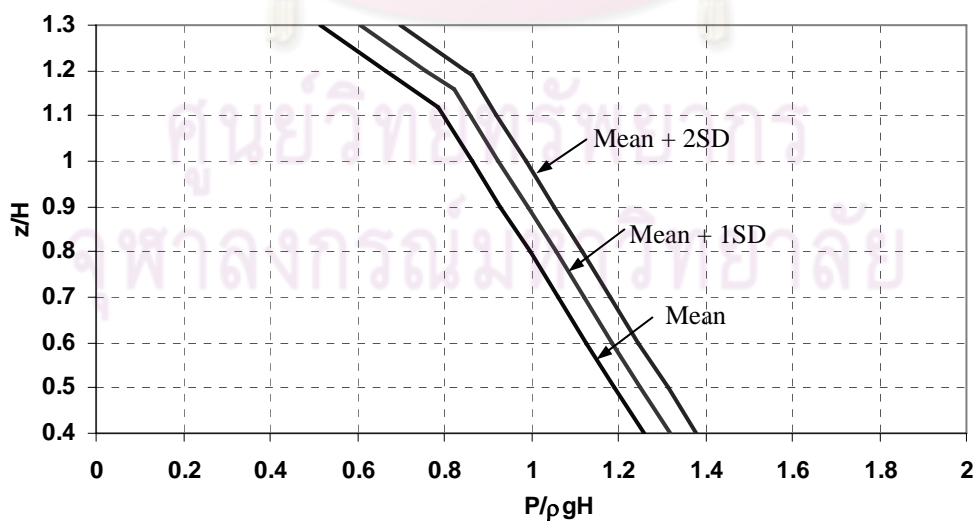
(c) Net horizontal pressure on bridge deck

Figure 5.1 Slowly-varying pressure distributions at 8 m nominal wave height

Table 5.1   Summary of the estimation error for slowly-varying forces using Eq. (5.1)

Cases	Simulated Force (MN)	Mean		Mean + 1SD		Mean +2SD	
		Force (MN)	Error (%)	Force (MN)	Error (%)	Force (MN)	Error (%)
CR36	6.9	7.3	6.5	7.7	12.3	8.1	18.0
CR41	7.6	7.1	-7.2	7.5	-2.0	7.8	3.3
CR46	7.1	6.8	-4.4	7.2	1.3	7.6	6.9
CR51	7.0	6.5	-7.6	6.9	-1.9	7.3	3.7
CR56	6.8	6.2	-8.7	6.6	-2.9	7.0	2.9
CR66	5.9	5.7	-3.9	6.1	3.2	6.5	10.0
CR76	4.6	4.9	6.4	5.4	17.2	5.9	27.3
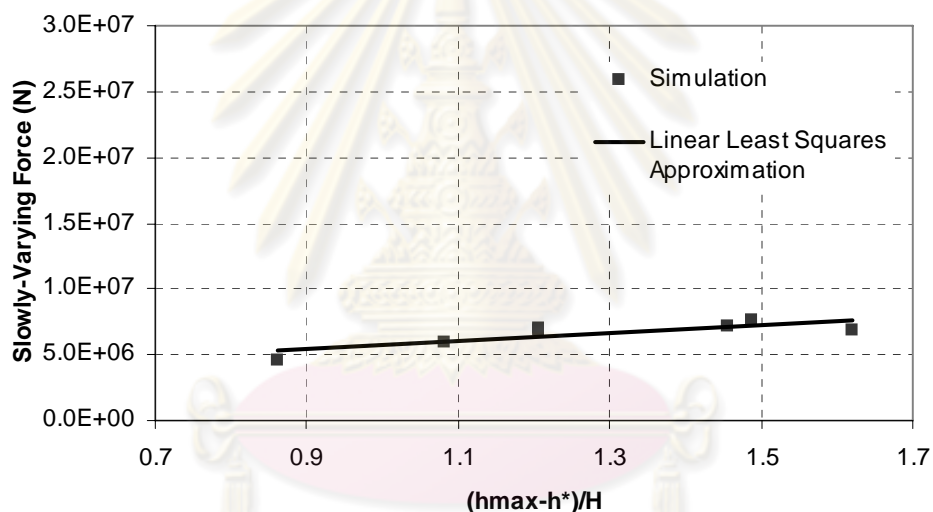
Figure 5.2 Correlation between the simulated slowly-varying force and $(h_{max}-h^*)/H$
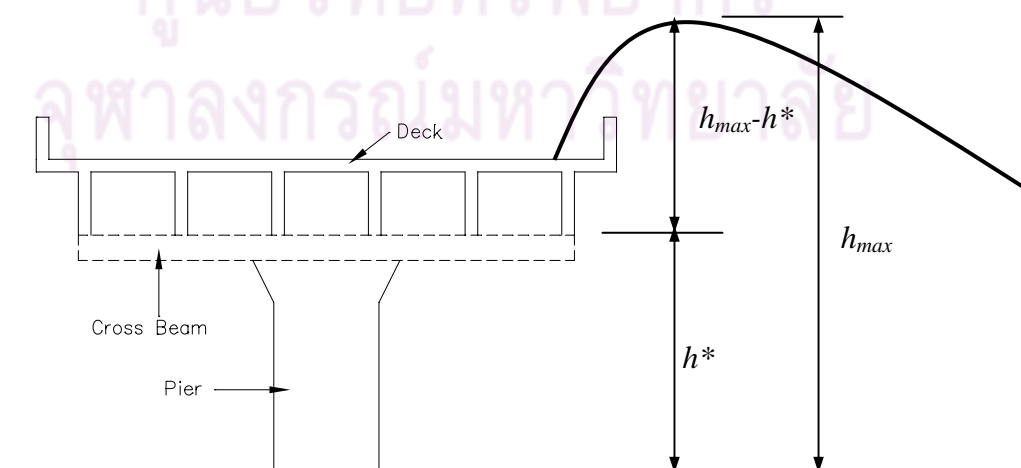
Figure 5.3 Definition of $(h_{max}-h^*)$

Different components (girders and parapets) contribute different proportions of wave force to the entire bridge deck for the seven deck clearances studied. Figure 5.4 illustrates the forces on the bridge deck components for the slowly-varying force component. The bridge components are categorized into the front girder, girders except the front one, front parapet and back parapet. The results show that 51 to 55 % and 45 to 49 % of the total forces on the bridge deck are contributed from girders and parapets, respectively. The forces on the girders other than the front girder are not significant. For parapets, the front parapet marks 25 % to 31 % of the total force.
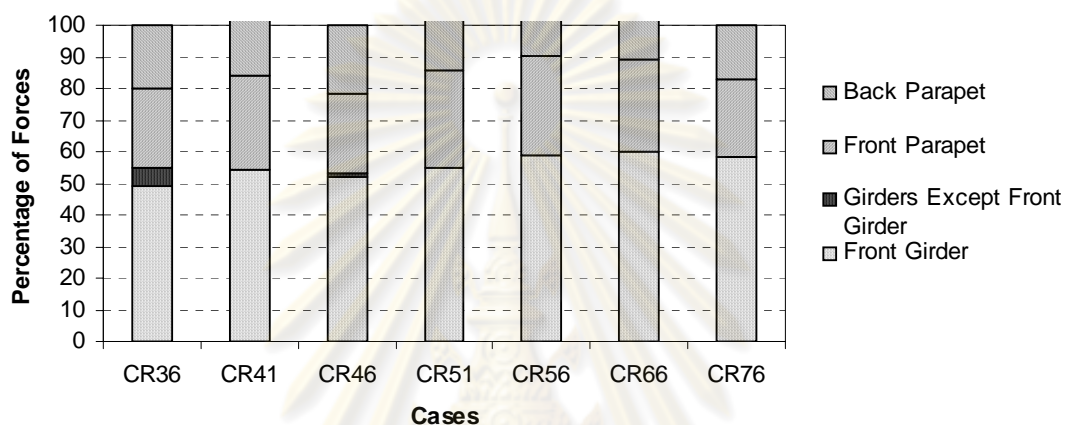
Figure 5.4 Percentage of the simulated horizontal slowly-varying forces on bridge components

5.1.2 Peak Horizontal Forces

As opposed to the slowly-varying forces, the simulated peak horizontal forces vary with deck clearance. Bridge deck with different clearances attains the peak horizontal force at different stages of wave attacks. In general, the peak horizontal force decreases when the deck clearance increases as shown in Figure 5.5. When the deck clearance is smaller than 65 % of the maximum flow depth, the peak horizontal force exceeds 2 times the slowly-varying force.

Figure 5.6 presents the correlation between the simulated peak horizontal and slowly-varying force component. The peak forces are in the range of 1.75 to 3.15 times their slowly-varying forces. The highest peak force is gained for CR41. A linear relation between the peak forces and (h_{max}-$h*/H$) is shown in Figure 5.7.
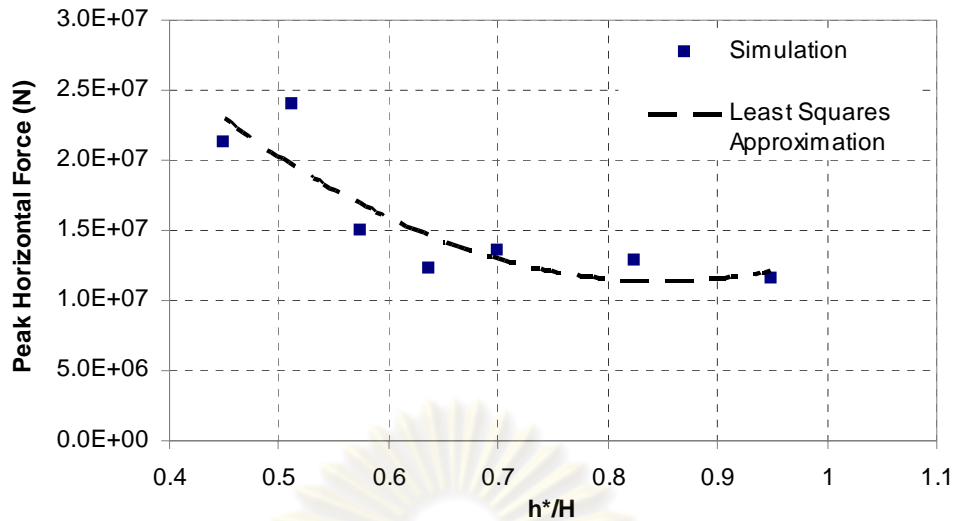
Figure 5.5 Correlations between the simulated peak horizontal forces and *h*/H*

Figure 5.6 Correlation between the simulated peak horizontal and slowly-varying forces
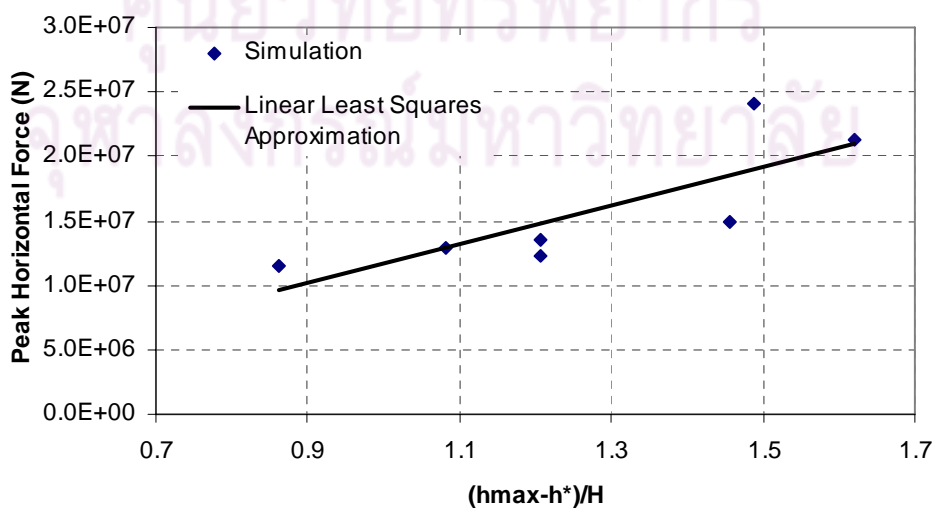
Figure 5.7 Correlation between the simulated peak horizontal force and $(h_{max}-h^*)/H$

Figure 5.8 illustrates the proportion of the peak forces contributed by individual bridge components. At the peak horizontal force, the contribution of all girders to the force is about 60 % or more, except for the two cases with larger clearances in which the contribution is only 40 – 50 %. Note that at least 40 % of the total force is exerted on the front girder. The contribution of the interior girders varies from 6 - 60 %. This indicates that the forces on the interior girders should not be neglected.
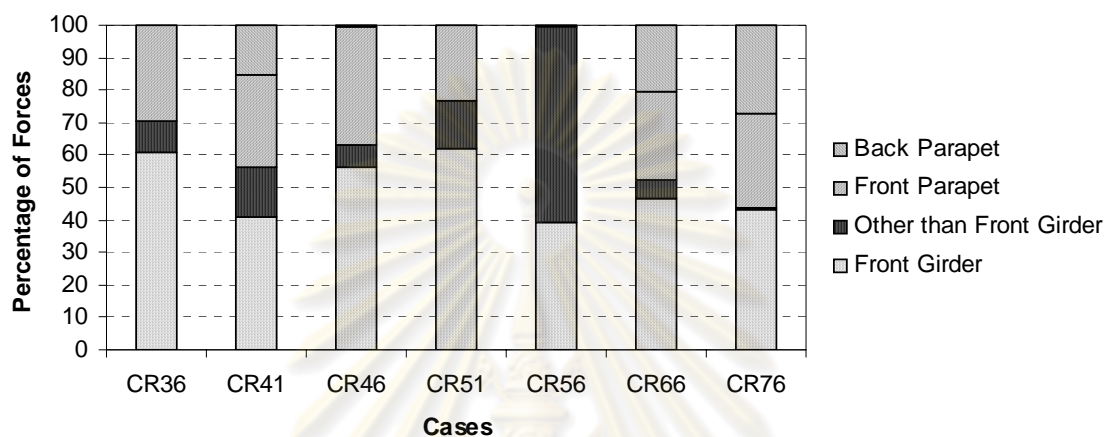
Figure 5.8 Percentage of the simulated peak horizontal forces on bridge components

5.1.3 Vertical Uplift Forces

Vertical uplift force occurs when the flow first hits the front girder and splashes upward to the protruded slab. Vertical uplift forces on the bridge decks for various $h*/H$ are shown in Figure 5.9. In general, vertical uplift force increases inverse proportionally with the deck clearances. The maximum and the minimum uplift forces of 18.5 MN and 3.8 MN are predicted, respectively. In general, the vertical uplift force is higher than the slowly-varying force, except for the case of CR66. As compared to the horizontal slowly-varying forces, the maximum vertical uplift forces are about 1 to 2.65 times the horizontal slowly-varying forces (Figure 5.10).

Figure 5.11 demonstrates the correlation between the maximum uplift forces and $(h_{max}-h*/H)$. The result shows that the maximum uplift force is related to the height of the wave above the bridge deck in a linear relation.
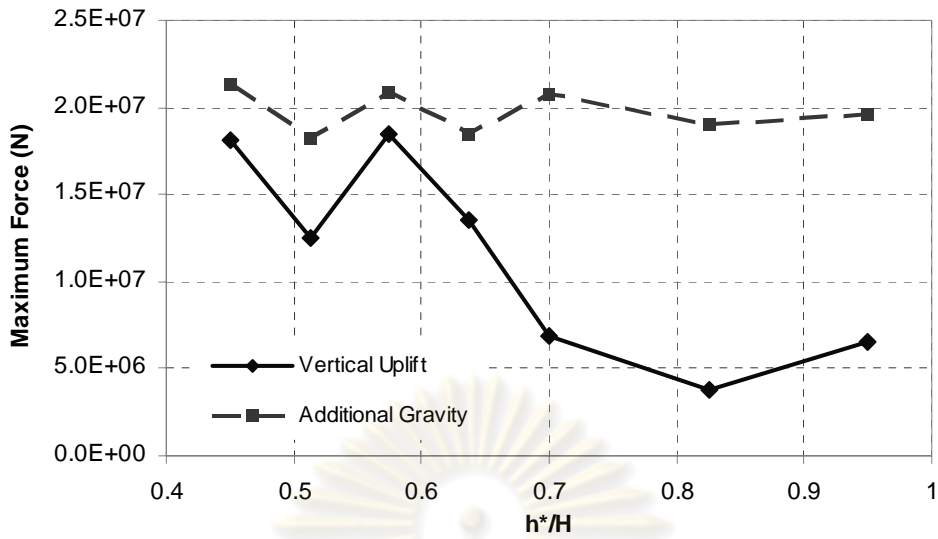
Figure 5.9 Correlations between the simulated maximum vertical forces and *h*/H*
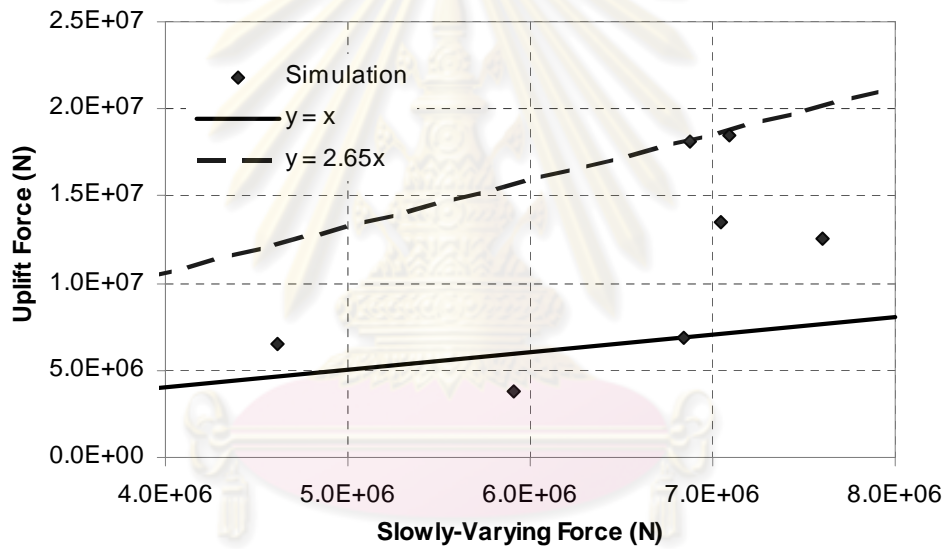
Figure 5.10 Correlation between the simulated maximum uplift and slowly-varying forces
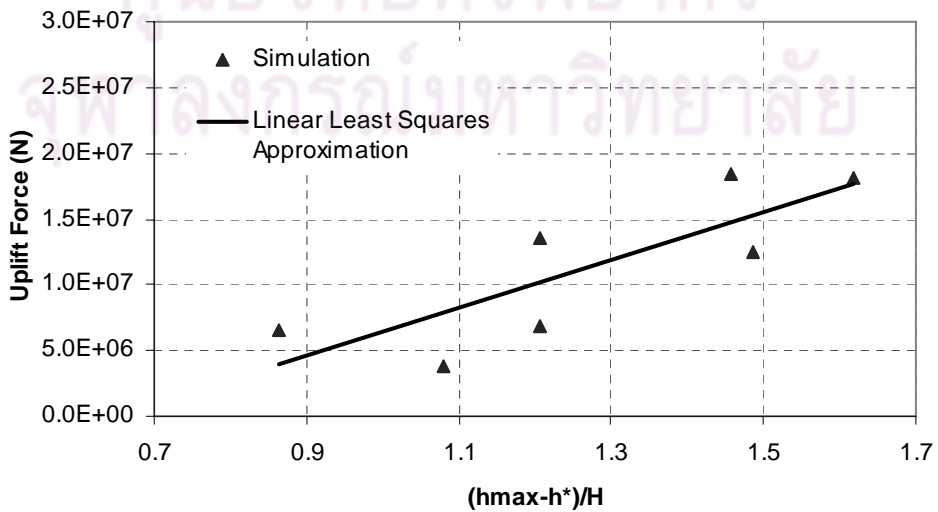
Figure 5.11 Correlation between the simulated maximum uplift force and $(h_{max}-h^*)/H$

5.1.4 Additional Gravity Forces

Additional gravity force is another type of vertical force that is not to be overlooked for submerged bridges during tsunami attacks. This force occurs later than the vertical uplift force, caused by the flow that overtops bridge deck. From the simulation results as presented in Figures 5.12 and 5.13, the maximum additional gravity forces do not vary substantially with the deck height and the slowly-varying force. However, they are generally larger than vertical uplift forces (Figure 5.9). Therefore, the additional gravity forces are essentially vital to be taken into consideration in the design of bridges subjected to tsunamis.
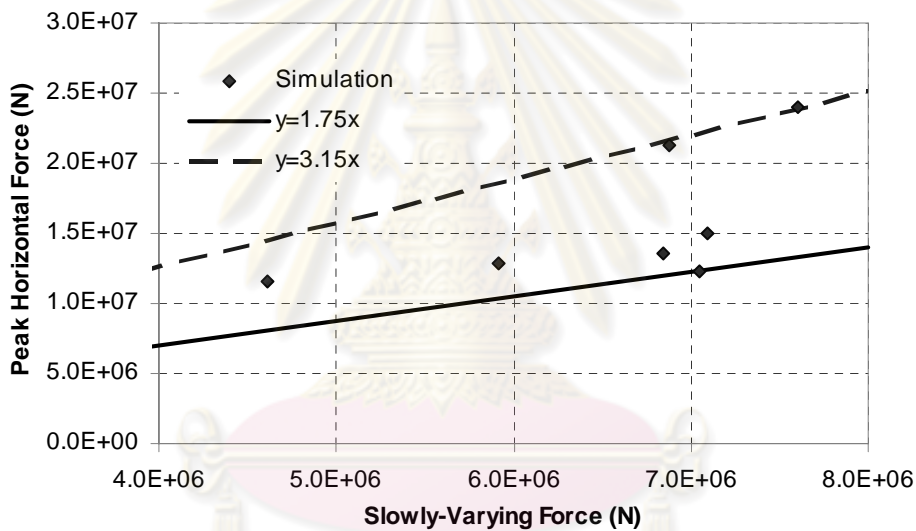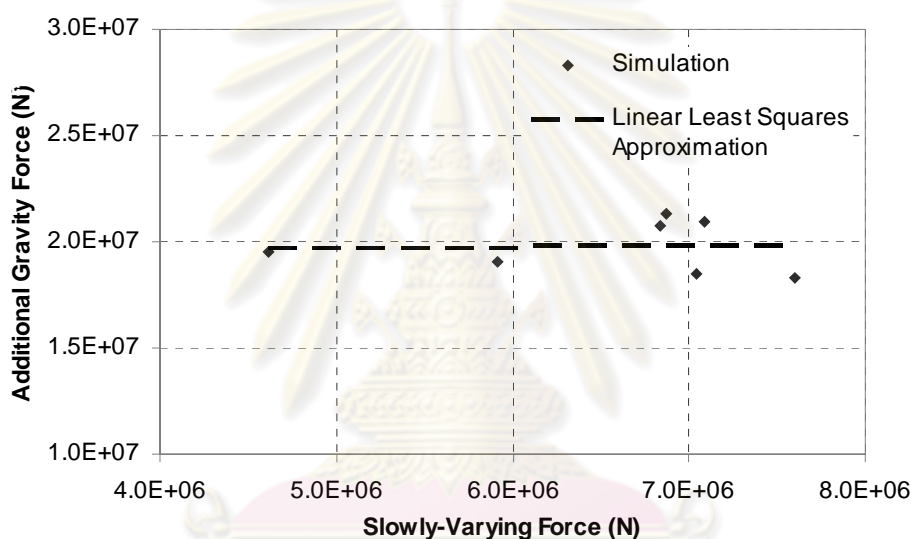

Figure 5.12 Correlation between the simulated additional gravity and slowly-varying forces
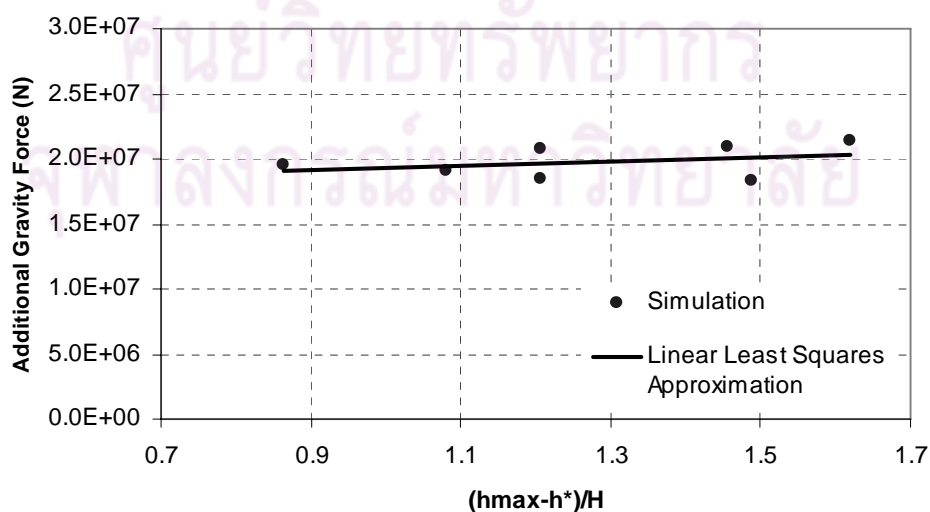
Figure 5.13 Correlation between the simulated additional gravity force and $(h_{max}-h^*)/H$

5.1.5 Design Considerations for Bridge Decks

As witnessed in the 2004 Indian Ocean tsunami, bridges suffered damage from significantly displaced to completely washed away of bridge decks from their abutments. These scenarios could happen if the lateral wave forces acting on the decks are larger than the lateral resisting forces of the decks or the vertical wave force exceed the self weight of the deck. In addition, the lateral resisting forces on the decks, in particular friction forces, could be reduced significantly when the decks are partially or fully submerged in the water due to the buoyancy of the decks (Iemura et al., 2005). Apart from the horizontal forces, vertical uplift and additional gravity forces can also cause damage to bridges.

Since it is quite a common practice in developing countries to rely on friction at the abutment bearings for resisting lateral loads, the decks are assumed to be placed on their abutments without any specific lateral or vertical control devises at this stage of study. It is of interest to compare the tsunami induced force on the deck to the lateral load resistance due to friction at the abutment bearings. In the investigation by Iemura et al. (2005), they predicted the water drag force to be four times the friction force.

As for this study, the forces obtained from the model test are converted to the forces in the prototype through the Froude number similarity rules. The bridge prototype is a reinforced concrete bridge with a unit weight of 24.5 kN/m^3. The self weight (*W*) of the bridge prototype with the dimensions shown in Figure 3.4 is 5.5 MN. Assuming an extreme value of the coefficient of friction of 0.6 at the ultimate state and the effective density or weight of the deck under submergence case is 60 % of the one under dry condition, the lateral resisting force due to the friction is then estimated from its vertical load as 3.3 MN and 2 MN for the decks in dry and wet conditions. The value of the tsunami force is found to range from 1.7 to 2.3 and 3.0 to 3.4 times the horizontal resisting force due to friction for the nominal wave heights of 6.5 m and 8 m, respectively (see Table 5.2). Thus, the estimated tsunami force is extremely high and it can easily wash away the bridge deck if no proper resisting element such as stopper or restrainer is provided.

Table 5.3 lists the simulated maximum horizontal forces and their ratios to the friction force for various deck clearances subjected to 8 m wave height. The calculation results show that the peak horizontal and the slowly-varying forces on bridge decks in the worst case exceed the lateral resisting forces by up to 630% and 130%, respectively, even under consideration of friction in the dry condition.

Table 5.2   Summary of the peak horizontal force on the bridge deck to friction force
            ratio in the prototype based on model tests

Cases	Average peak force on the deck in the prototype, $F_{deck,p} = F_{deck,m} \times 10^6$ (MN)	$F_{deck,p} / F_f*$	Average $F_{deck,p} / F_f*$
SO1_65	7.0	2.1	
SO2_65	7.6	2.3	
SO3_65	7.1	2.2	2.1
SO4_65	5.6	1.7	
SO5_65	7.4	2.2	
SO1_80	9.9	3.0	
SO2_80	11.0	3.4	
SO3_80	9.9	3.0	3.1
SO4_80	10.2	3.1	
SO5_80	10.0	3.0	

Note: *Friction force, F_f = 0.6 × vertical loading (self-weight of the deck) = 3.3 MN

Table 5.3   Summary of the peak horizontal forces on the bridge deck to friction force
            ratio in the prototype at various deck clearances based on numerical
            simulation (H = 8 m)

Cases	Peak horizontal force, F_{max} (MN)	Slowly-varying force, F_{sv} (MN)	F_{max} / F_f	F_{sv} / F_f
CR36	21.3	6.9	6.5	2.1
CR41	24	7.6	7.3	2.3
CR46	15	7.1	4.6	2.2
CR51	12.3	7.0	3.8	2.1
CR56	13.5	6.8	4.1	2.1
CR66	6	5.9	1.8	1.8
CR76	0.43	4.6	0.13	1.4

The simulation result demonstrates that the vertical uplift force and the additional gravity force occur at different times. The vertical uplift force is higher than the self weight of the deck except for the case of CR66 (Table 5.4). The ratios of the maximum uplift force to the self weight range from 0.7 to 3.4. On the contrary, the additional gravity force does not vary significantly for the deck with various clearances. The simulated additional gravity forces are between 3.3 to 3.9 times the self-weight of the deck. This indicates that the vertical uplift force and the additional gravity force on the bridge deck should be taken into consideration separately in the design of bridge structures.

Table 5.4   Summary of the maximum vertical forces on the bridge deck to self weight ratio in the prototype based on numerical simulation

Cases	Maximum uplift force, F_{v+} (MN)	Maximum additional gravity force, F_{v-} (MN)	F_{v+} / W	F_{v-} / W
CR36	18.1	21.3	3.3	3.9
CR41	12.5	18.3	2.3	3.3
CR46	18.5	20.9	3.4	3.8
CR51	13.5	18.5	2.5	3.4
CR56	6.9	20.7	1.3	3.8
CR66	3.8	19.1	0.7	3.5
CR76	6.5	19.6	1.2	3.6

In order to withstand tsunami force, structural integrity and stability of bridges need to be investigated. The lateral and vertical movements of the deck have to be accessed. Bridge deck should be equipped with lateral movement devices that could resist the peak horizontal force and the vertical uplift force. Moreover, the additional gravity force should also be taken into account for the design of the slab member of the deck.

5.2 Proposed Method for Estimating Tsunami Forces on Bridge Decks

As mentioned in the literature review in Chapter II, generally previous studies on bridges subjected to tsunamis did not come out with any formulation that could estimate the maximum peak horizontal or vertical uplift forces. Iemura et al. (2007) proposed the drag formula to estimate the peak horizontal force. The drag coefficient was determined from the highly transient flow condition which is different from the original definition of the drag coefficient under the steady uniform flow. As a result, the appropriate velocity to be used in determining tsunami forces is not easily selected. Kataoka et al. (2006) suggested the Goda's pressure distribution, which is formulated for offshore breakwaters, can sufficiently estimate the slowly varying force.

To make the prediction of tsunami forces possible, a method that is based on the proposed approach for wave forces on bridge decks by Douglass et al. (2006) is suggested. The details of this method can be found in Douglass et al. (2006) or Douglass and Krolak (2008). The recommended equations to estimate the horizontal slowly-varying force, F_{sv}, and the horizontal impact force, F_{im}, on the bridge deck in Douglass et al. (2006) are as follows:

$$F_{sv} = [1 + c_r(N-1)]\, c_{va\text{-}h}\, F_{ref} \tag{5.2}$$

$$F_{im} = \{[1 + c_r\,(N-1)]\, c_{va\text{-}h} + c_{im\text{-}h}\}\, F_{ref} \tag{5.3}$$

where F_{ref} is a reference horizontal force defined by Eq. (5.3), c_r is a force reduction coefficient for the internal girders due to the shielding effect of the front girder, N is the number of girders, $c_{va\text{-}h}$ is an empirical coefficient for the horizontal slowly-varying force and $c_{im\text{-}h}$ is an empirical coefficient for the horizontal impact force.

The reference force, F_{ref}, is given by

$$F_{ref} = \gamma\,(\Delta z_h)\, A_h \tag{5.4}$$

where γ is the unit weight of water, A_h is the vertical projection area of the bridge deck and Δz_h is the level of submergence measured from the maximum wave crest elevation to the centroid of A_h (Figure 5.14).
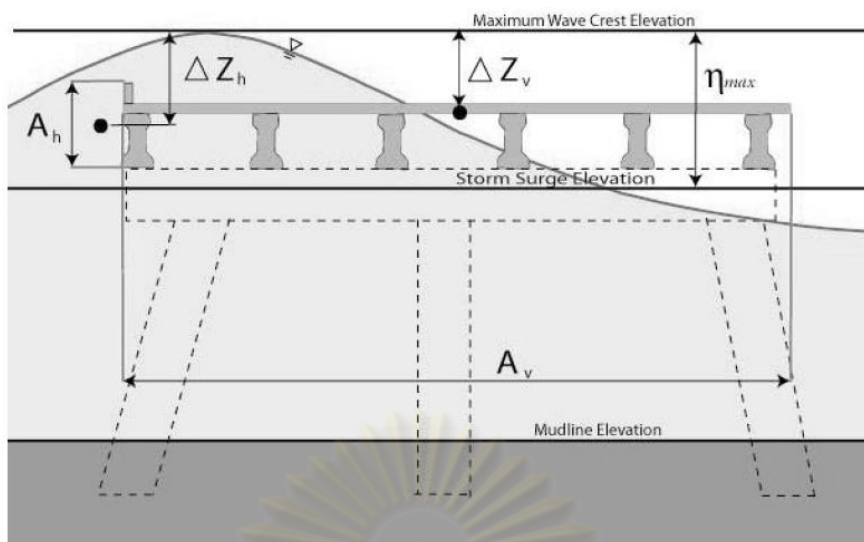
Figure 5.14 Definition for parameters in the proposed wave load estimation method by
Douglass et al. (2006)

However, the reference force in Douglass et al. (2006) which is based on the level
of submergence is not applicable for broken waves (tsunami bores or surges) because the
crest of the wave is not easily predicted using the current knowledge. Therefore, the
reference forces based on the pressure distribution derived for the estimation of slowly-
varying forces (in subsection 5.1.1) are proposed for tsunami cases. For this case, the
reference forces are associated to the height of the deck and the nominal wave heights
which are known values for the force estimation. The reference force, F_{ref}, is expressed as

$$F_{ref} = pA \tag{5.5}$$

where p = the mean pressure acting on the deck that can be estimated from Eq. (5.1), and
A = the vertical projected area of the deck.

The maximum forces acting on bridge decks, i.e. horizontal slowly-varying, peak
horizontal, vertical uplift and additional gravity forces are estimated from the following
expressions:

Horizontal slowly-varying force, $(F_{sv})_{max} = c_{sv} F_{ref}$ (5.6a)

Peak horizontal force, $(F_h)_{max} = (1 + c_p) F_{ref}$ (5.6b)

Vertical uplift force, $(F_{uplift})_{max} = (1 + c_u) F_{ref}$ (5.6c)

Additional gravity force, $(F_{ag})_{max} = (1 + c_a) F_{ref}$ (5.6d)

where c_{sv} = an empirical coefficient for the maximum horizontal slowly-varying force,

c_p = an empirical coefficient for the peak horizontal force,

c_u = an empirical coefficient for the vertical uplift force, and

c_a = an empirical coefficient for the additional gravity force.

The empirical coefficients in Eq. (5.6) are determined from the numerical simulation results. It is noted from the previous section that the slowly-varying force and the additional gravity force are almost independent of the deck clearance while the peak horizontal force and the vertical uplift force are related to the deck clearance. Therefore, the coefficients of c_{sv} and c_a are defined as constants while the coefficients of c_p and c_u are defined as a function of the deck clearance. Figures 5.15a and 5.15b show the determination of the coefficients of c_p and c_u, respectively. The coefficients of c_p and c_u, which are represented by the vertical axis in the figures, are determined from regression as follows:

$$c_p = 18.21 \, (h^*/H)^2 - 27.14 \, (h^*/H) + 11.13 \qquad (5.7a)$$

$$c_u = 9.9 \, (h^*/H)^2 - 17.21 \, (h^*/H) + 7.67 \qquad (5.7b)$$

By using the pressure distribution based on the mean value and the empirical coefficients of $c_{sv} = 1.05$, $c_a = 2$, c_p and c_u from Eqs. (5.7a and 5.7b), the predicted forces calculated from the proposed empirical formulae are compared with the simulated forces from the numerical simulation as shown in Figure 5.16. It is found that the peak horizontal force could be predicted with an error of -12 % to 25 % of the simulation result. The discrepancy is -25 % to 35 % for the uplift force, and -10 % to 10 % for other force components.

It should be emphasized that the cases considered are limited to seven different deck clearances subjected to the most severe wave scenario, and the maximum flow velocity is about 2.4 $\sqrt{(gH)}$ as characterized in Section 3.9.1. Obviously, these empirical coefficients should be refined by adequate data from experimental and analytical simulations for other flow conditions and deck configurations.
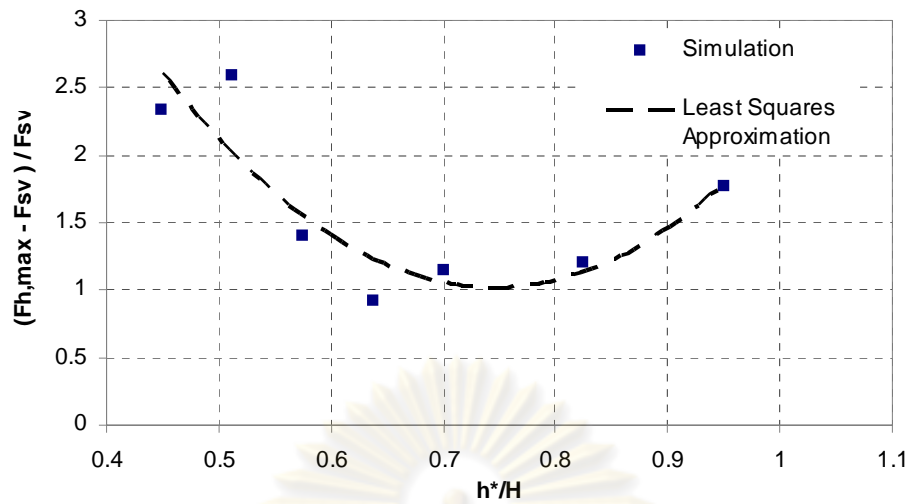
(a) $c_p = (F_{h,max} - F_{sv}) / F_{sv}$
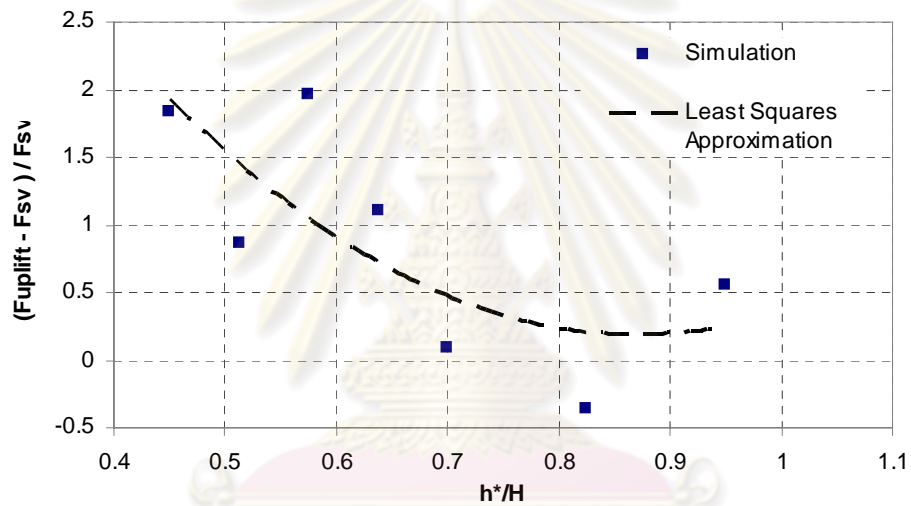
(b) $c_u = (F_{uplift} - F_{sv}) / F_{sv}$

Figure 5.15 Determination of c_p and c_u
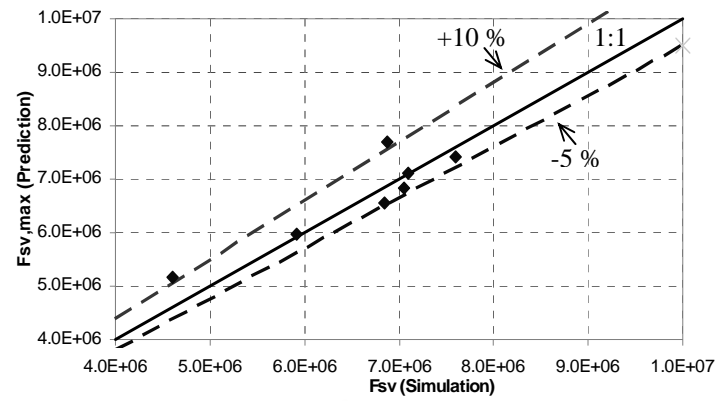
(a) Horizontal slowly-varying force
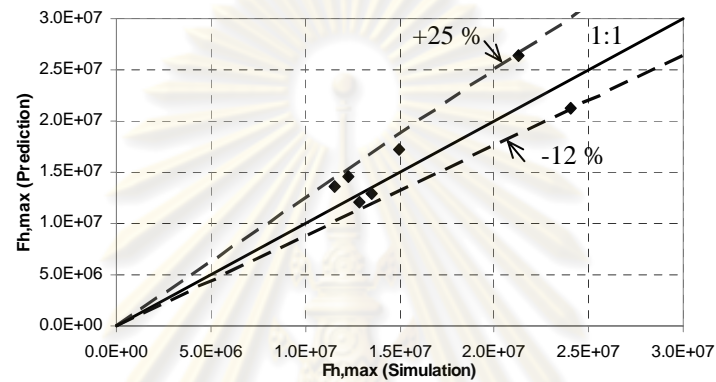
(b) Peak horizontal force
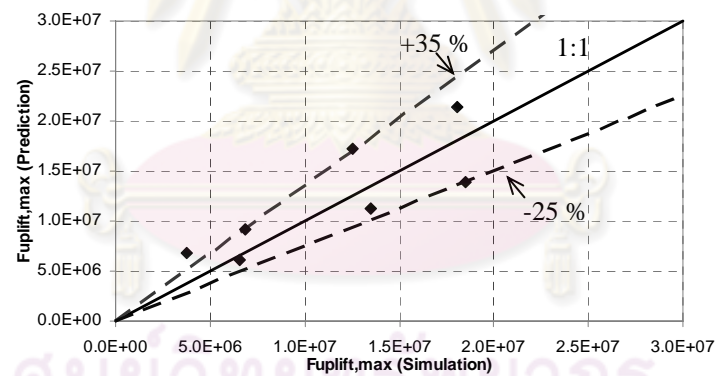
(c) Vertical uplift force
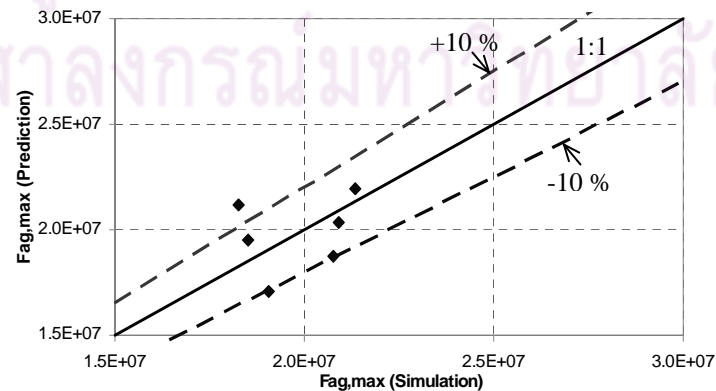
(d) Additional gravity force

Figure 5.16 Comparisons of the predicted and the simulated forces

5.3 Effects of Perforation in Deck Frontal Area in Reducing Tsunami Force

It should be noted that the load cell in the experimental setup as presented in Chapter III measured wave forces exerted on the entire bridge model (both the piers and the deck in the horizontal direction). In order to obtain the forces on the deck only, it is necessary to measure the force on the piers. Therefore, experiments on a stand-alone piers model were conducted. Force time histories of the stand-alone piers model at various nominal wave heights were obtained. By subtracting the force on the piers from the force on the entire bridge, the wave force acting on the bridge deck was then determined. This has been made based on assumptions which will be elaborated next.

With the foregoing reasoning as discussed in Section 3.9.3.3, the time history of the wave force acting on the piers of the entire bridge model can be approximated from that on the stand-alone piers scaled up so that the initial peak in its time history reaches the first peak in the force time history of the entire bridge as shown in Figure 5.17. This is justified that the force on the deck is zero at the initial wave attack while the flow depth is small to hit the deck. The force time history for the bridge deck is then determined from the subtraction of the scaled force time history of the stand-alone piers model from the recorded force time history of the entire bridge (Figure 5.17). Figure 5.18 highlights the typical force time histories of the bridge deck of various bridge models while Appendices B and C compile all the force time histories of the bridge deck. The time scale in Figure 5.18 is set in the manner so that the second 0 indicates the instance of the wave starts to splash up to the girders.
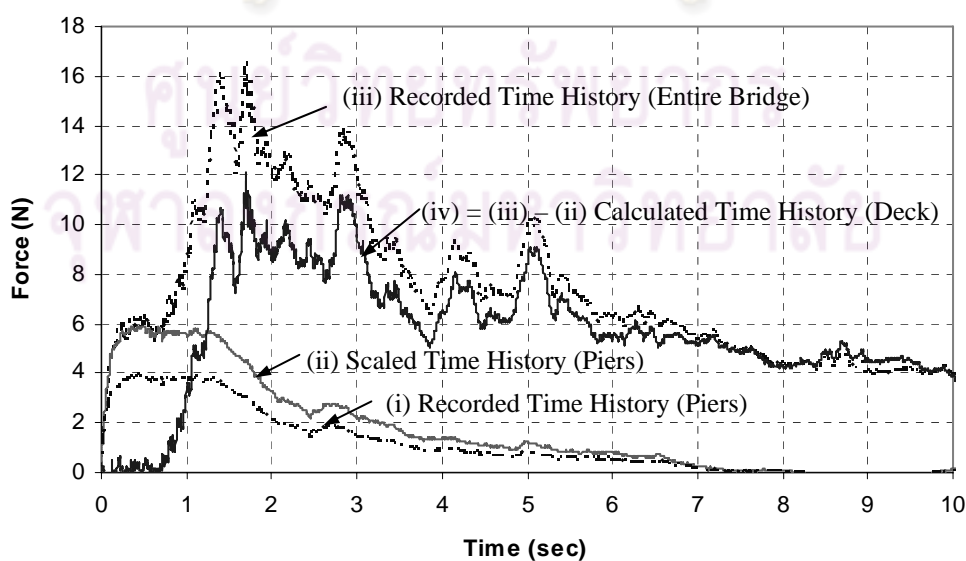
Figure 5.17 Determination of force time histories of the bridge deck

(a) G0+P0 (*H* = 65 mm)

(b) G0+P0 (*H* = 80 mm)

(c) G20+P0 (*H* = 65 mm)

(d) G20+P0 (*H* = 80 mm)

(e) G20+P20 (*H* = 65 mm)

(f) G20+P20 (*H* = 80 mm)

(g) G0+P60 (*H* = 65 mm)

(h) G0+P60 (*H* = 80 mm)

(i) G10+P60 (*H* = 65 mm)

(j) G10+P60 (*H* = 80 mm)

Figure 5.18 Deck force time histories at 65 mm and 80 mm nominal wave heights

5.3.1 Quantitative Assessment on Horizontal Force Reduction

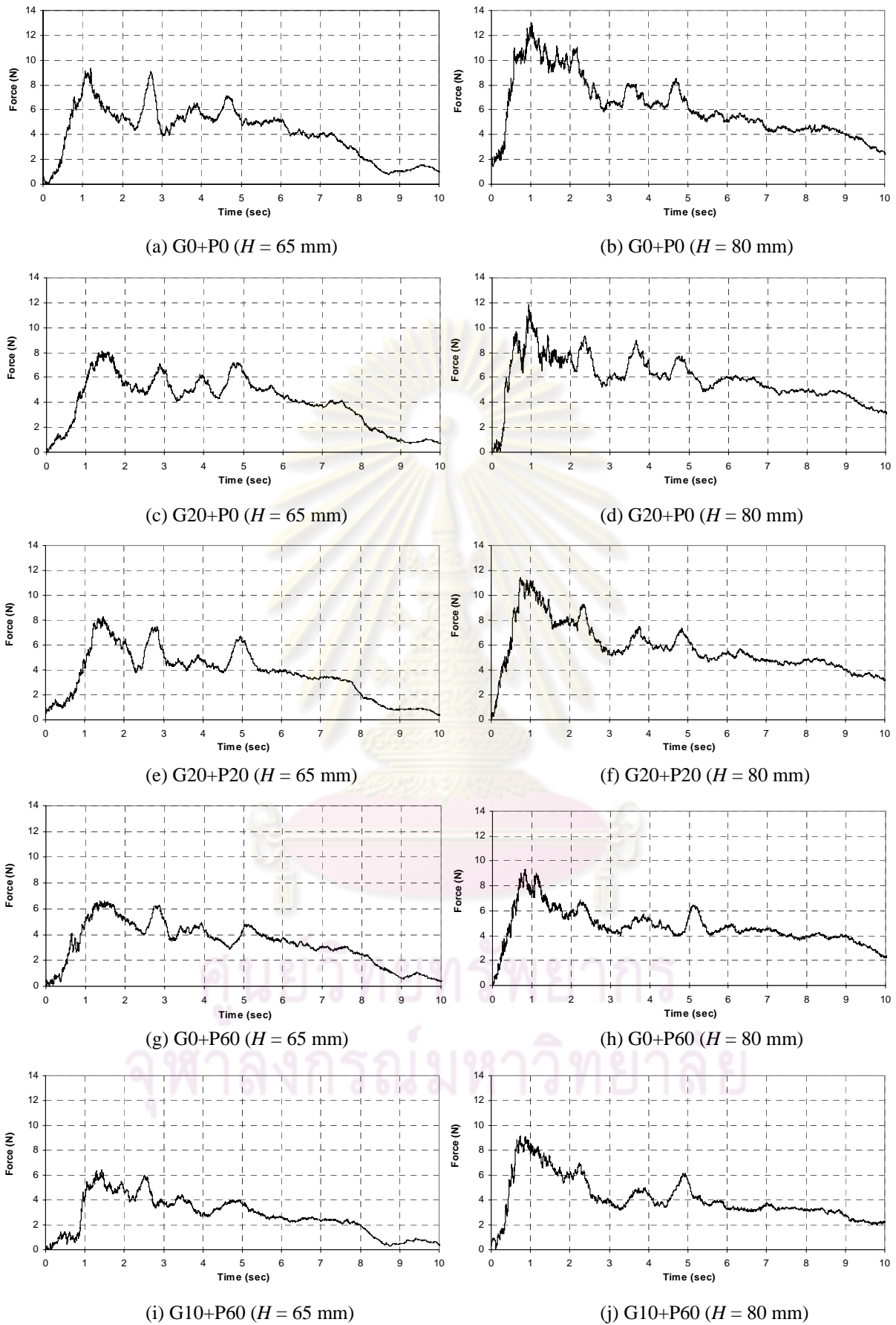Tsunami forces acting on bridge decks are reduced to various extents when there are perforations in the girders or parapets. In general, reduction of forces is not restricted to the maximum force but the forces throughout the whole time history. Based on the typical force time history for tsunami force acting on various bridge deck models as shown in Figure 5.18, the maximum horizontal forces at 80 mm wave height (Figures 5.18b, 5.18d, 5.18f, 5.18h and 5.18j) are higher than those at 65 mm wave height (Figures 5.18a, 5.18c, 5.18e, 5.18g and 5.18i), ranging from nearly 40 % to 50 %. Figure 5.19 displays the relation of the peak force reduction with the perforation area. Generally, peak forces decrease with the increase of the perforation areas in the deck as shown in Figure 5.19a; however, the trend of reduction seems not to be in a linear function. Figure 5.19b shows the percentage of force and total deck frontal area reductions for all deck configurations. Also plotted in a dotted straight line is the line with the slope of 1-to-1. The reduction percentage in the peak horizontal force varies in the rate close to the deck frontal area reduction, especially when the deck frontal area is rather small. Note that peak force reduction is slightly greater than the frontal deck area reduction when the latter is 20 % or more.

5.3.2 Qualitative Assessment on Vertical Force Reduction

Vertical uplift force on bridge deck subjected to tsunami may contain the impulsive, drag and buoyant forces which act in the vertical direction. In this experimental study, vertical force could not be measured by the load cell due to its limitation; thus, the quantitative discussion of vertical force reduction for various bridge deck models is not possible at this stage. However, considerable vertical uplift force reduction is anticipated for the perforated I-beam girder bridge decks. Therefore, the qualitative discussion is made here based on the observation of the flow mechanics in the numerical analysis.

Vertical impulsive and drag force on the bridge deck are caused by the vertical movement of the flow in a relatively short and long durations, respectively, when the flow splashes upward or its height exceeds the soffit of the girders. To the best of the author's knowledge, no clear correlation of the forces in vertical and horizontal directions has been established so far. Nonetheless, the ratio of the maximum vertical uplift force to the maximum horizontal force can reach as high as 2 to 3 based on various independent

experimental studies on different bridge configurations by Nimmala et al. (2006), Kataoka et al. (2006), and Sugimoto and Unjoh (2007). Based on the computation results in Section 4.3.2.3, the maximum vertical uplift force is of 51 % to 153 % of the maximum horizontal force. Thus it is postulated that the deck configuration should also affect the magnitude of the vertical uplift forces.
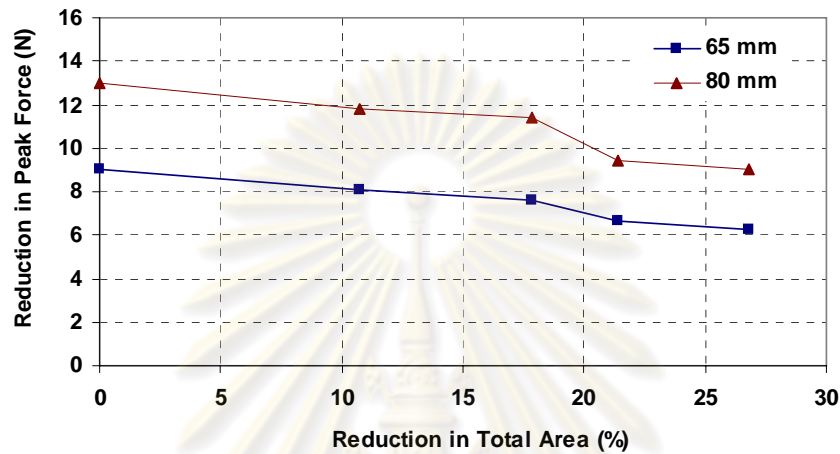
(a) Force reduction in Newton
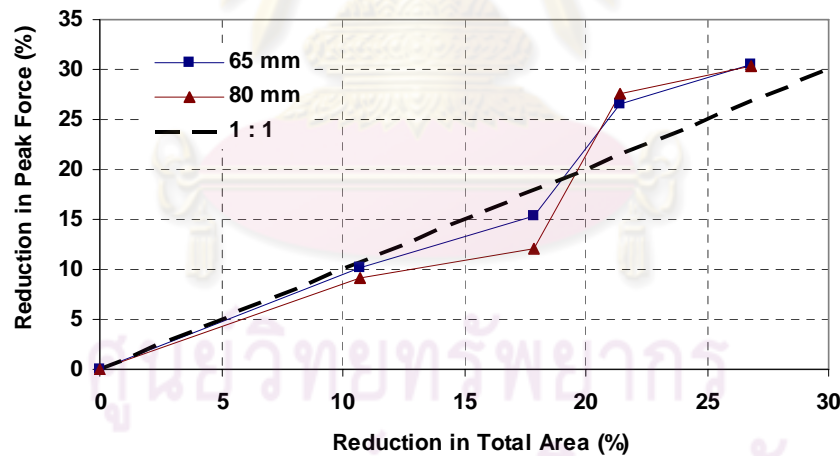
(b) Force reduction in percentage

Figure 5.19 Correlation between peak force reduction and perforation area

It is shown in Section 4.3.2.1 that the uplift force is generated by the wave that is forced to be pushed up to the soffit of the deck after hitting the girders. Most of the wave pressures act on the soffit of the protruded deck facing the wave attack. In the context of perforated bridge deck in the vertical plane of girders and parapets, the vertical impulsive and drag forces are most likely affected by the perforated girders but not the perforated parapets. The perforated girders are expected to reduce the volume of the water to be pushed up to the deck and in turn reduce the upward wave pressure exerted on the deck. Moreover, substantial reduction in vertical uplift force is anticipated if perforations are introduced on the protruded deck.

CHAPTER VI

CONCLUSIONS AND RECOMMENDATIONS

This chapter concludes the significant findings of tsunami acting on bridges and the contributions in the field of tsunami hazard mitigation. Recommendations for future works are proposed.

6.1 Significance of Findings

Important findings from the experimental and numerical studies are summarized in this section. They are presented into three main categories, i.e. experimental investigation of the stand-alone piers and complete pier-deck bridge models, numerical simulation of bridge prototypes and effect of perforations in bridge deck in reducing tsunami force on bridge deck.

Experimental investigations of the wave attack on stand-alone piers and a complete pier-deck bridge models reveal the following:

1. The leading edge of the wave, initially very small in depth, first strikes the bridge piers with a maximum velocity (but with a small flow depth) and splashes up the piers. The peak force on the bridge is registered later following the upward splash of the wave on the deck.

2. The pressure at the bottom of the pier records a maximum value about 3.5 to 4.5 times the hydrostatic pressure and remains at 1.5 to 2 times the hydrostatic pressure for a much longer period subsequently. The pressure at the mid-span of the front girder picks up at a later time after the peak pressure is registered in the pier. It attains a maximum value up to 2.5 to 3 times the hydrostatic pressure and remains at 1 to 1.5 times the hydrostatic pressures for a much longer period subsequently. The pressures on the inner girders are practically insignificant.

3. The hydrodynamic force on the bridge pier is influenced by the existence of the bridge deck which obstructs the free splash-up and topping over of the wave. For the configurations studied, the actual force on the pier in the real bridge could be underestimated by as much as 33 % if the widely accepted

drag coefficient of 2.0 is used. Therefore, it is important to consider the complete pier-deck system in experimental or analytical investigation of tsunami forces on the structural components.

Experimental investigation on five types of bridge deck configurations which consist of various perforation areas in girders and/or parapets reveal that perforation can contribute to mitigating the tsunami attack to a certain extent as follows:

1. The reduction percentage in the peak horizontal force varies in the rate close to the deck frontal area reduction, especially when the deck frontal area is rather small.
2. The results show that the perforation area of not less than 20 % the deck frontal area is effective in reducing the maximum force for both nominal wave amplitudes studied.

The results from the numerical simulation provide useful information on tsunami action on bridges which is beneficial to engineers and scientists as follows:

1. Tsunami flow around bridges with different configurations exhibits different effects on the structures. By simplifying the I-beam girder bridges to 3D Box (with piers), 3D Deck (I girder deck without piers) and 2D Deck (I girder deck without piers), the peak horizontal force and vertical uplift force at the initial wave impingement period are underestimated by about 15 % and 60 %, respectively. Hence, the use of the actual pier-deck configuration is vital as far as the peak force is concerned.
2. The highest pressure on the deck due to the wave impingement is concentrated on the front face of the deck. At the initial stage of the wave attack, both the front and interior girders contribute to the peak force exerted on the deck. Thereafter, with the flow surrounding the girders, the flow induces similar pressure on both faces of the interior girders, with the consequence of negligible contribution from the interior girders.
3. The simulation on real configuration of bridge prototypes show that the horizontal slowly-varying force is independent of the bridge clearance and it can be estimated by the proposed pressure distribution in this study. An

empirical method for estimating the peak horizontal, vertical uplift and additional gravity forces on bridge deck based on some multiple of the slowly-varying force (as reference load) is proposed. The proposed method are limited to the cases subjected to the wave scenario studied in this study.

6.2 Recommended Future Studies

The following recommendations are suggested to improve the study in the future:

1. To estimate forces on each individual component (pier or deck), it is necessary to have the entire bridge model extensively instrumented with pressure gauges for accurate measurement of forces on each component.
2. Large-scale physical model tests (< 1/10) are needed for bridges with the complex geometry to minimize the scale effects that can be enhanced by air entrainment, turbulence and upward splashing and to enable the measurement of pressure distribution profiles especially for vertical distribution.
3. The flow around bridges is highly three dimensional. Pressure measurements at various locations are necessarily important. In addition, flow visualization technique such as Particle Image Velocimetry (PIV) or Laser Doppler Velocimetry (LDV) may be adopted.
4. The movement of the bridge deck and the failure mechanisms subjected to the combinations of forces should be investigated through experimental and numerical studies.
5. Bridge configurations affect the forces on the deck substantially. Various configurations in terms of the deck aspect ratio and type of bridge deck should be explored in the future.

REFERENCES

Arikawa, T., Ikebe, M., Yamada, F., Shimosako, K. and Imamura, F. (2005). Large model test of tsunami force on a revetment and on a land structure. <u>Journal of Coastal Engineering</u>, Japan Society of Civil Engineers 52: 746-750 (in Japanese).

Arikawa, T., Ohtsubo, D., Nakano, F., Shimosako, K., Takahashi, S., Imamura, F. and Matsutomi, H. (2006). Large model test on surge front tsunami force. <u>Journal of Coastal Engineering</u>, Japan Society of Civil Engineers 53: 796-800 (in Japanese).

Arikawa, T., Nakano, F., Ohtsubo, D., Shimosako, K. and Ishikawa, N. (2007). Research on destruction and deformation of structures due to surge front tsunami. <u>Journal of Coastal Engineering</u>, Japan Society of Civil Engineers 54: 841-845 (in Japanese).

Arikawa, T., Nakano, F., Shimosako, K. and Yamano, T. (2008). Behaviors of concrete wall under the impulsive tsunami force. <u>Journal of Coastal Engineering</u>, Japan Society of Civil Engineers 55: 261-265 (in Japanese).

Arnason, H. (2005). <u>Interactions between an Incident Bore and a Free-Standing Coastal Structure</u>. Ph.D. Thesis, University of Washington, Seattle.

Asakura, R., Iwase, K., Ikeya, T., Takao, M., Kaneto, T., Fujii, N. and Ohmori, M. (2000). An experimental study on wave force acting on on-shore structures due to overflowing tsunamis. <u>Journal of Coastal Engineering</u>, Japan Society of Civil Engineers 47: 911-915 (in Japanese).

Ballantyne, D. (2006). Sri Lanka lifelines after the December 2004 Great Sumatra Earthquake and Tsunami. <u>Earthquake Spectra</u> 22(S3): S545-559.

Camfield, F. E. (1994). Tsunami effects on coastal structures, In Coastal Hazards: Perception, Susceptibility and Mitigation. <u>Journal of Coastal Research</u> (Special Issue No. 12): 177-187.

CCH. (2000). <u>The City and County of Honolulu Building Code</u>. Chapter 16, Article 11. Department of Planning and Permitting of Honolulu, Hawaii.

Chanson, H., Aoki, S. and Maruyama, M. (2003). An experimental study of tsunami runup on dry and wet horizontal coastlines. <u>Science of Tsunami Hazards</u> 20(5): 278-293.

Chung, K. F. and Lawson, R. M. (2001). Simplified design of composite beams with large web openings to Eurocode 4. <u>Journal of Construction Steel Research</u> 57: 135-163.

Chung, K. F., Liu, T. C. H. and Ko, A. C. H. (2001). Investigation on Vierendeel mechanism in steel beams with circular web openings. Journal of Construction Steel Research 57: 467-490.

Chung, K. F., Liu, C. H. & Ko, A. C. H. (2003). Steel beams with large web openings of various shapes and sizes: an empirical design method using a generalized moment-shear interaction. Journal of Construction Steel Research 59: 1179-1200.

Cross, R. H. (1967). Tsunami surge forces. Journal of Waterways and Harbors Division, Proceedings of the ASCE 93(WW4): 201-231.

Cuomo, G., Shimosako, K. and Takahashi, S. (2009). Wave-in-deck loads on coastal bridges and the role of air. Coastal Engineering 56: 793-809.

Douglass, S. L., Chen, Q. J., Olsen, J. M., Edge, B. L. and Brown, D. (2006). Wave forces on bridge decks. U.S. Department of Transportation, Federal Highway Administration, 74.

Douglass, S. L. and Krolak, J. (2008). Highways in the coastal environment. Federal Highway Administration, National Highway Institute, FHWA NHI-07-096, Hydraulic Engineering Circular No. 25: 246.

Endoh, K. and Unjoh, S. (2006). Analytical study on the response characteristics of bridges against tsunami. Proceedings of the 61st JSCE Annual Meeting, 869-870. Shiga: Japan Society of Civil Engineers (in Japanese).

Farris, G. S., Smith, G. J., Crane, M. P., Demas, C. R., Robbins, L. L. and Lavoie, D. L. (2007). Science and the storms: the USGS response to the hurricanes of 2005. U.S. Geological Survey Circular 1306, 283.

FEMA-55. (2000). Coastal construction manual: Principles and practices of planning, siting, designing, constructing, and maintaining residential buildings in coastal areas. Federal Emergency Management Agency.

FEMA-P646. (2008). Guidelines for design of structures for vertical evacuation from tsunamis. Federal Emergency Management Agency.

Flow-3D. (2007). Flow-3D user manual: Excellence in flow modeling software, v 9.2. Flow Science, Inc., Santa Fe, N.M.

Fukui, Y., Nakamura, M., Shiraishi, H. and Sasaki, Y. (1963). Hydraulic study on tsunami. Coastal Engineering in Japan 6: 67-82.

Ghobarah, A., Saatcioglu, M. and Nistor, I. (2006). The impact of the 26 December 2004 Earthquake and Tsunami on structures and infrastructure. Engineering Structures 28: 312-326.

Goda, Y. (1973). A new method of wave pressure calculation for the design of composite breakwaters. <u>Report of the Port and Harbour Research Institute</u>, 31-69 (in Japanese).

Hamzah, M. A., Mase, H. and Takayama, T. (2000). Simulation and experiment of hydrodynamic pressure on a tsunami barrier. <u>Coastal Engineering in Japan</u>: 1501-1507.

Hirt, C. W. and Nichols, B. D. (1981). Volume of fluid (VOF) method for the dynamics of free boundaries. <u>Journal of Computational Physics</u> 39: 201-225.

Hirt, C. W. and Sicilian, J. M. (1985). A porosity technique for the definition of obstacles in rectangular cell meshes. <u>Proceedings of the 4th International Conference on Ship Hydrodynamics</u>, 1-19. Washington, D.C.: National Academy of Science.

Ho, D. K. H., Donohoo, S. M., Boyes, K. M. and Lock, C. C. (2003). Numerical analysis and the real world: It looks pretty but is it right? <u>Proceedings of the 9th NAFEMS World Congress</u>, Orlando, FL.: The International Association for the Engineering Analysis Community.

Hughes, S. A. (2005). <u>Physical models and laboratory techniques in coastal engineering</u>. (Advanced Series on Ocean Engineering Vol. 7). Singapore: World Scientific Publishing Co., Inc.

Iemura, H., Pradono, M. H. and Takahashi, Y. (2005). Report on the tsunami damage of bridges in Banda Aceh and some possible countermeasures. <u>Proceedings of the 28th JSCE Earthquake Engineering Symposium</u>, Tokyo: Japan Society of Civil Engineers.

Iemura, H., Pradono, M. H., Yasuda, T. and Tada, T. (2007). Experiments of tsunami force acting on bridge models. <u>Journal of Earthquake Engineering</u>, Japan Society of Civil Engineers 29.

Ikari, H. and Gotoh, H. (2007). Numerical simulation of washed process of girder bridge by tsunami run-up. <u>Journal of Coastal Engineering</u>, Japan Society of Civil Engineers 54: 211-215 (in Japanese).

Ikeno, M. and Tanaka, H. (2003). Experimental study on impulsive force of drift body and tsunami running up to land. <u>Journal of Coastal Engineering</u>, Japan Society of Civil Engineers 50: 721-725 (in Japanese).

Ikeno, M., Mori, N. and Tanaka, H. (2001). Experimental study on tsunami force and impulsive force by a drifter under breaking bore like tsunami. <u>Journal of Coastal Engineering</u>, Japan Society of Civil Engineers 48: 846-850 (in Japanese).

JPHA. (1999). Technical standards and commentaries of port and harbor facilities. Japan Port and Harbour Association (in Japanese).

JRA. (2002). Specifications for highway bridges, Part 1: Common design principles. Japan Road Association, Maruzen (in Japanese).

Kataoka, S., Kusakabe, T. and Nagaya, K. (2006). Wave forces acting on bridge girders struck by tsunami. Proceedings of the 12th Japan Earthquake Engineering Symposium, 154-157. Tokyo: Japan Society of Civil Engineers (in Japanese).

Kusakabe, T., Matsuo, O. and Kataoka, S. (2005). Introduction of a methodology to mitigate tsunami disaster by the pre-evaluation of tsunami damage considering damage investigation of 2004 tsunami disaster in the Indian Ocean. Proceedings of the 21st US-Japan Bridge Engineering Workshop, Tsukuba, Japan.

Lawson, R. M., Lim, J., Hicks, H. J. and Simms, W. T. (2006). Design of composite asymmetric cellular beams and beams with large web openings. Journal of Construction Steel Research 62: 614-629.

Liu, T. C. H. and Chung, K. F. (2003). Steel beams with large web openings of various shapes and sizes: finite element investigation. Journal of Construction Steel Research 59: 1159-1176.

Lukkunaprasit, P. and Ruangrassamee, A. (2008). Building damage in Thailand in 2004 Indian Ocean tsunami and clues for tsunami-resistant design. The Institution of Engineers Singapore Journal, Part A: Civil and Structural Engineering, IES 1(1): 17-30.

Maheshwari, B. K., Sharma, M. L. and Narayan, J. P. (2006). Geotechnical and structural damage in Tamil Nadu, India, from the December 2004 Indian Ocean Tsunami. Earthquake Spectra 22(S3): S475-493.

Mizutani, S. and Imamura, F. (2000). Hydraulic experimental study on wave force of a bore acting on a structures. Journal of Coastal Engineering, Japan Society of Civil Engineers 47: 946-950 (in Japanese).

Mizutani, S. and Imamura, F. (2002). Design of coastal structure including the impact and overflow of tsunami. Journal of Coastal Engineering, Japan Society of Civil Engineers 49: 731-735 (in Japanese).

Modjeski & Masters, I. (2007). Guide specifications for bridges vulnerable to coastal storms. 40 (90% Draft Report).

Moriyama, T., Shoji, G., Fujima, K. and Shigihara, Y. (2008). Experimental study associated with tsunami wave load acting onto a bridge deck. General Meeting of

the Japan Association of Earthquake Engineering, 146-147. Sendai, Japan: (in Japanese).

Nimmala, S. H., Yim, S. C., Cheung, K. F. and Wei, Y. (2006). Tsunami design criteria for coastal infrastructure: A case study for Spencer Creek Bridge, Oregon. Oregon Department of Transportation.

Okada, S., Mitamura, H. and Ishikawa, H. (2005). The collapse mechanism and the temporary restoration of Omori Bridge damaged by the storm surge of typhoon No. 18 in 2004. Proceedings of the 21st US-Japan Bridge Engineering Workshop, Tsukuba, Japan.

Ramsden, J. D. and Raichlen, F. (1990). Forces on a vertical wall caused by incident bores. Journal of Waterway, Port, Coastal and Ocean Engineering, American Society of Civil Engineers 116(5): 592-613.

Ramsden, J. D. (1996). Forces on a vertical wall due to long waves, bores and dry-bed surges. Journal of Waterway, Port, Coastal and Ocean Engineering, American Society of Civil Engineers 122(3): 134-141.

Richardson, E. V. and Davis, S. R. (2001). Evaluating scour at bridges. Federal Highway Administration, National Highway Institute, FHWA-NHI-01-001, Hydraulic Engineering Circular No. 18: 378.

Scawthorn, C., Ono, T., Iemura, H., Ridha, M. and Purwanto, B. (2006). Performance of lifelines in Banda Aceh, Indonesia, during the December 2004 Great Sumatra Earthquake and Tsunami. Earthquake Spectra 22(S3): S511-544.

Schumacher, T., Higgins, C., Bradner, C., Cox, D. and Yim, S. (2008). Large-scale wave flume experiments on highway bridge superstructures exposed to hurricane wave forces. The Six National Seismic Conference on Bridges & Highways, Charleston, South Carolina.

Sheth, A., Sanyal, S., Jaiswal, A. and Gandhi, P. (2006). Effects of the December 2004 Indian Ocean Tsunami on the Indian Mainland. Earthquake Spectra 22(S3): S435-473.

Shoji, G. and Mori, Y. (2006). Hydraulic model experiment to simulate the damage of a bridge deck subjected to tsunamis. Journal of Coastal Engineering, Japan Society of Civil Engineers 53: 801-805 (in Japanese).

Sugimoto, T. and Unjoh, S. (2007). Hydraulic model tests on the bridge structures damaged by tsunami and tidal wave. Proceedings of the 23rd US-Japan Bridge Engineering Workshop, 233-242. Tsukuba, Japan.

Sugimoto, T. and Unjoh, S. (2008). Experimental study on damage mechanism of bridges by tsunami. Proceedings of the 11th Symposium on Ductility Design Method for Bridges, 97-100. Tokyo, Japan.

Sugimoto, T., Usui, T. and Unjoh, S. (2008). The effect of tsunami and storm surge on bridges in flume test. Civil Engineering Journal, Public Work Research Institute 50(11): 24-29 (in Japanese).

Tanimoto, K., Tsuruya, K. and Nakano, S. (1984). Tsunami force of Nihonkai-Chuku Earthquake in 1983 and cause of revetment damage. Proceedings of the 31st Japanese Conference of Coastal Engineering, 257-261. (in Japanese).

Togashi, H. (1986). Wave force of tsunami bore on a vertical wall. Science of Tsunami Hazards 41(1): 25-38.

Unjoh, S. (2005). Damage to transportation facilities. The damage induced by Sumatra earthquake and associated tsunami of December 26, 2004, A report of the reconnaissance team of Japan Society of Civil Engineers, 66-76.

Yeh, H. (2007). Design tsunami forces for onshore structures. Journal of Disaster Research 2(6): 531-536.

Yim, S. C. (2005). Modeling and simulation of tsunami and storm surge hydrodynamics loads on coastal bridge structures. Proceedings of the 21st US-Japan Bridge Engineering Workshop, Tsukuba, Japan.

ศูนย์วิทยทรัพยากร
จุฬาลงกรณ์มหาวิทยาลัย

APPENDICES

Appendix A

Calibration Charts

(a) Wave gauge No.1   (b) Wave gauge No. 2
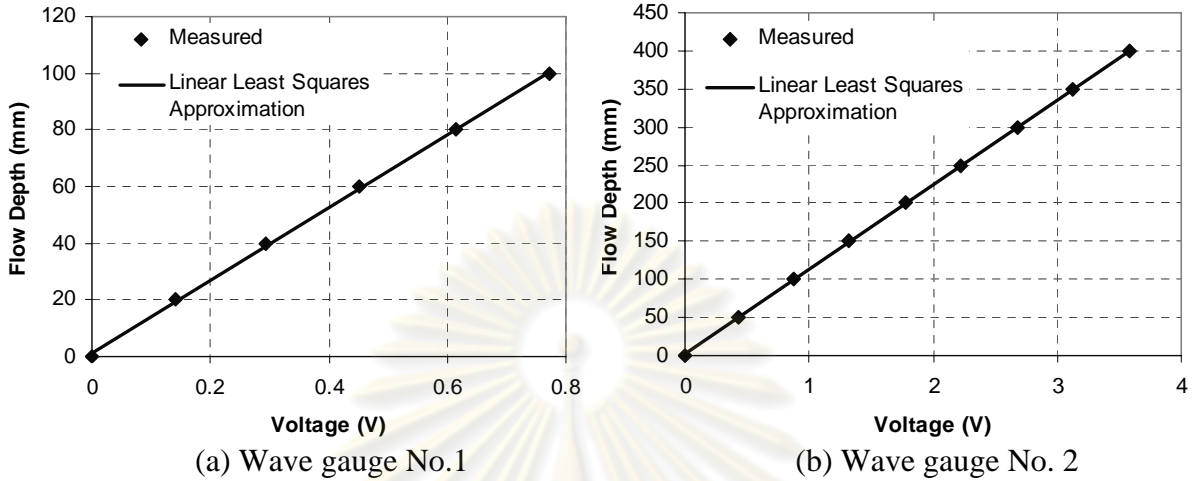
Figure A1 Correlation between voltage and flow depth
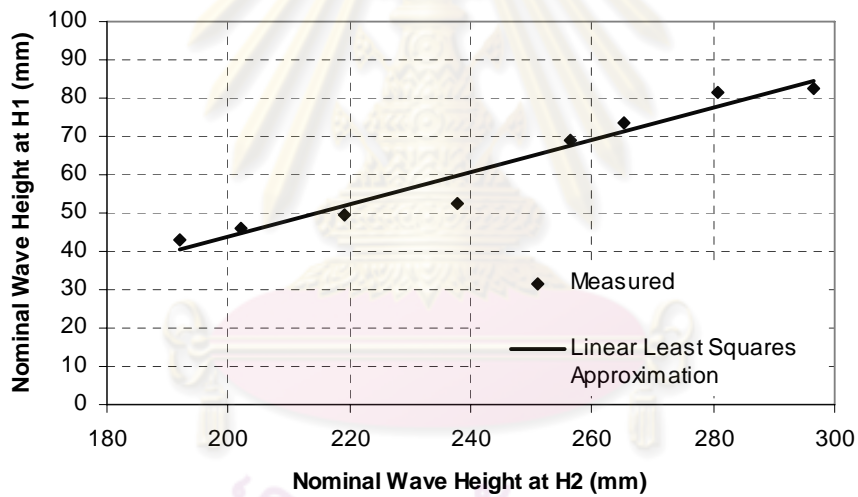
Figure A2 Correlation of nominal wave heights between H1 and H2
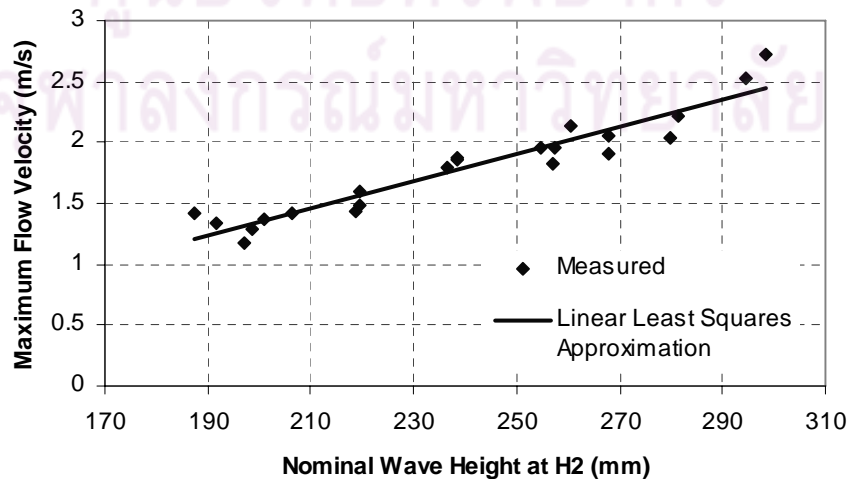
Figure A3 Correlation between velocity and wave height
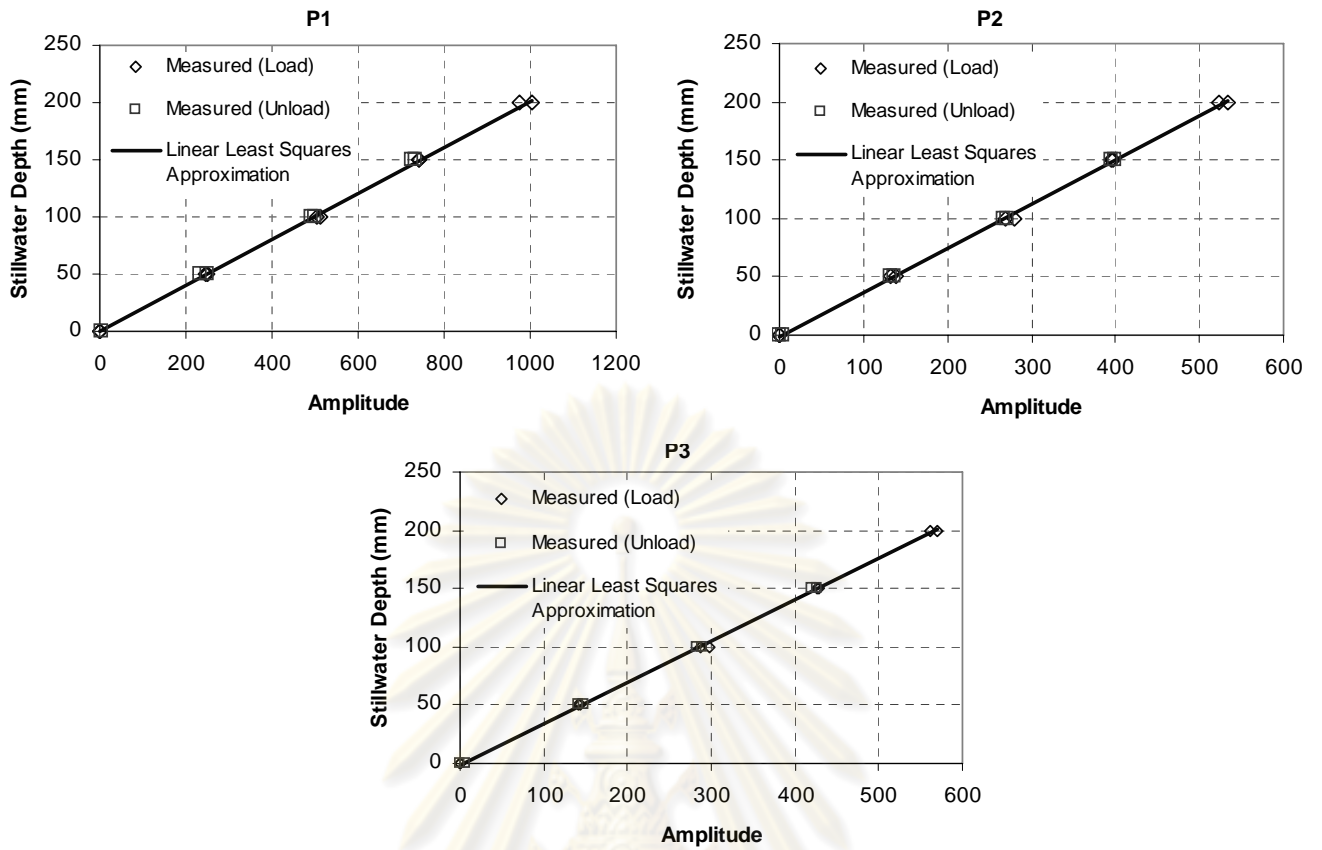
Figure A4 Correlation between still-water depth and amplitude for pressure gauges
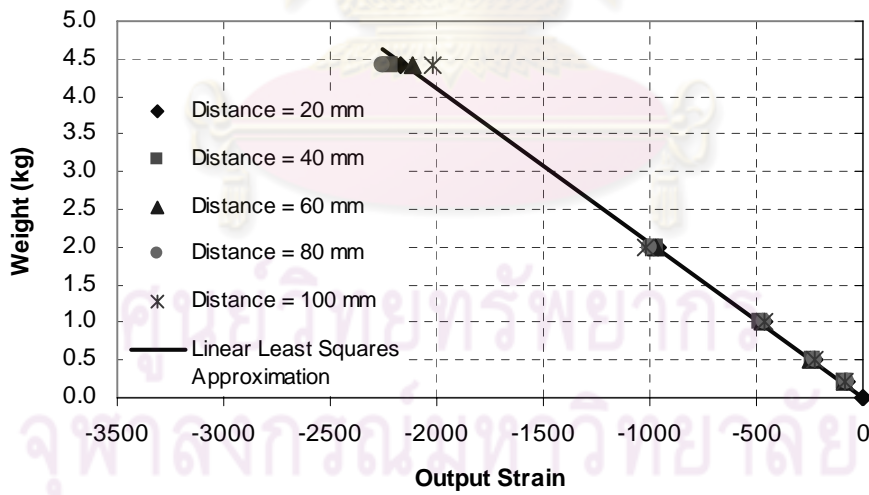
Figure A5 Correlation between standard weight and output strain of load cell

Appendix B

Force and Pressure Time Histories of Bridges without Perforations in Girders and Parapets
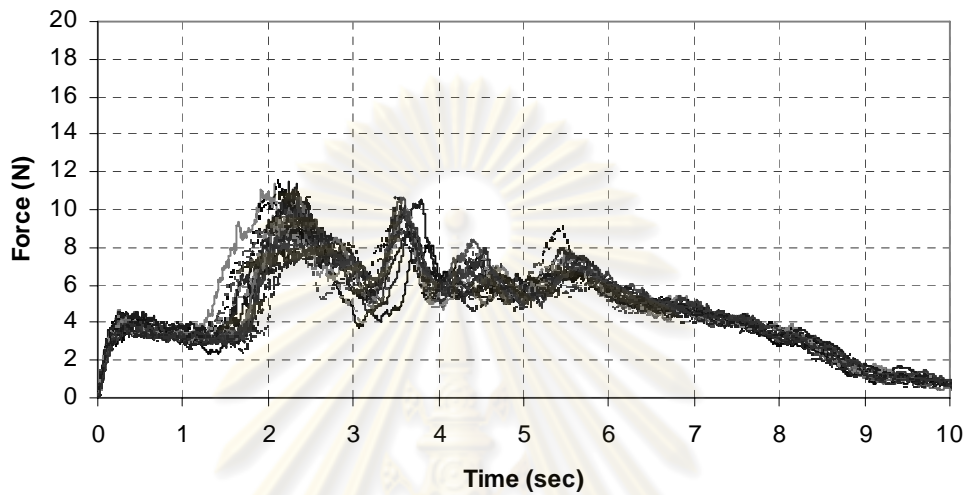
(a) 65 mm nominal wave height
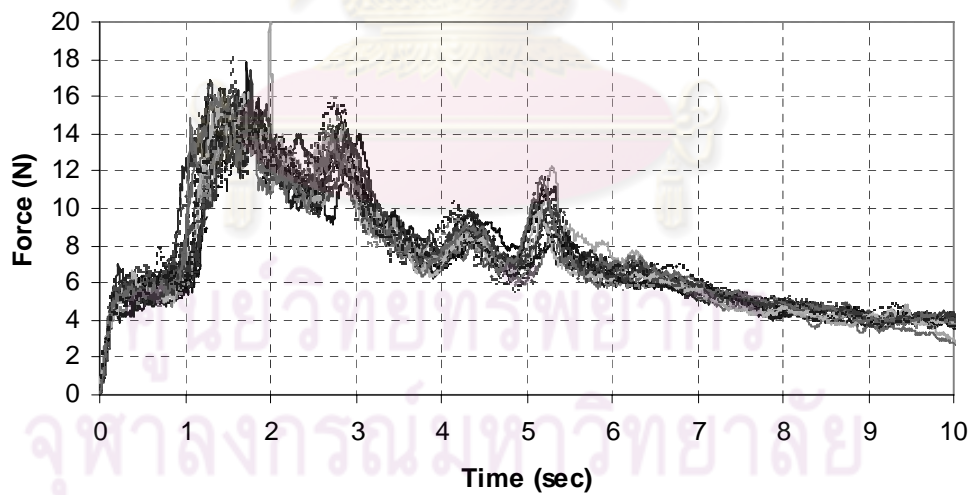
(b) 80 mm nominal wave height

Figure B1 Total horizontal force time histories of the entire bridge model
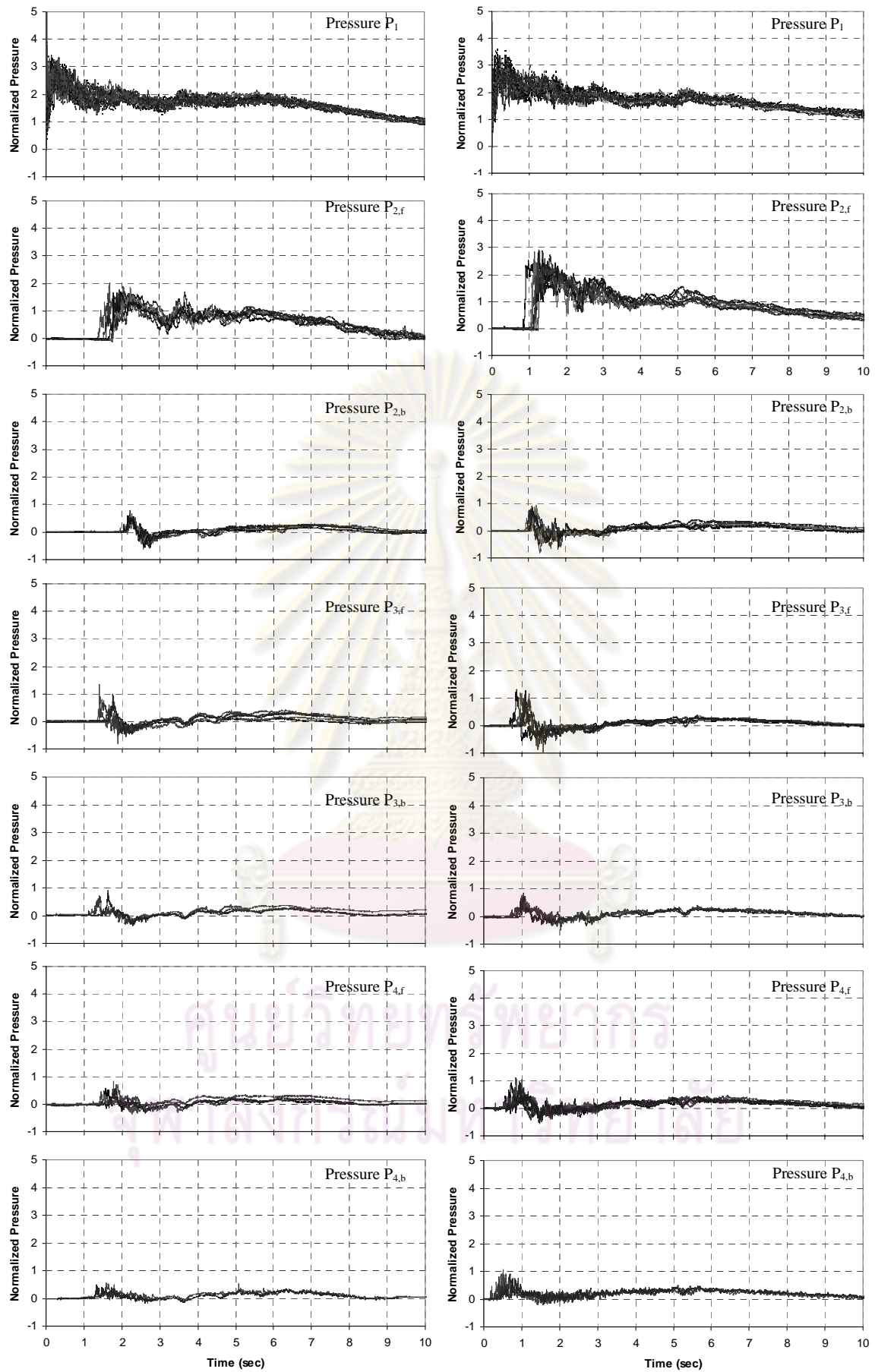
Figure B2 Pressure time histories at 65 mm (left) and 80 mm (right)

nominal wave heights

Appendix C

Force and Pressure Time Histories of Bridges
with Perforations in Girders and/or Parapets

(a) G20+P0 (H = 65 mm)

(b) G20+P0 (H = 80 mm)

(c) G20+P20 (H = 65 mm)

(d) G20+P20 (H = 80 mm)

(e) G0+P60 (H = 65 mm)

(f) G0+P60 (H = 80 mm)

(g) G10+P60 (H = 65 mm)
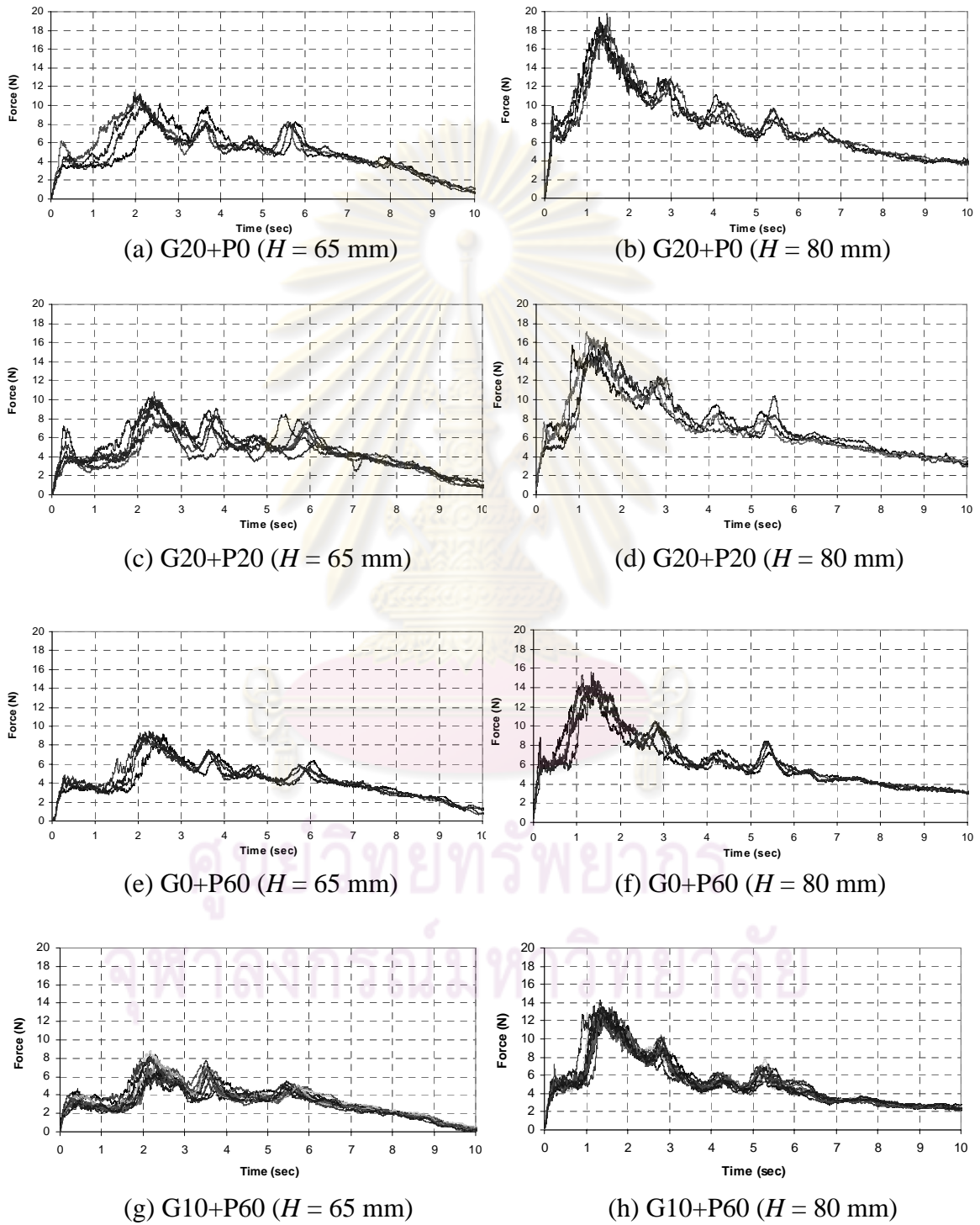
(h) G10+P60 (H = 80 mm)

Figure C1 Time histories of forces for perforated bridge decks
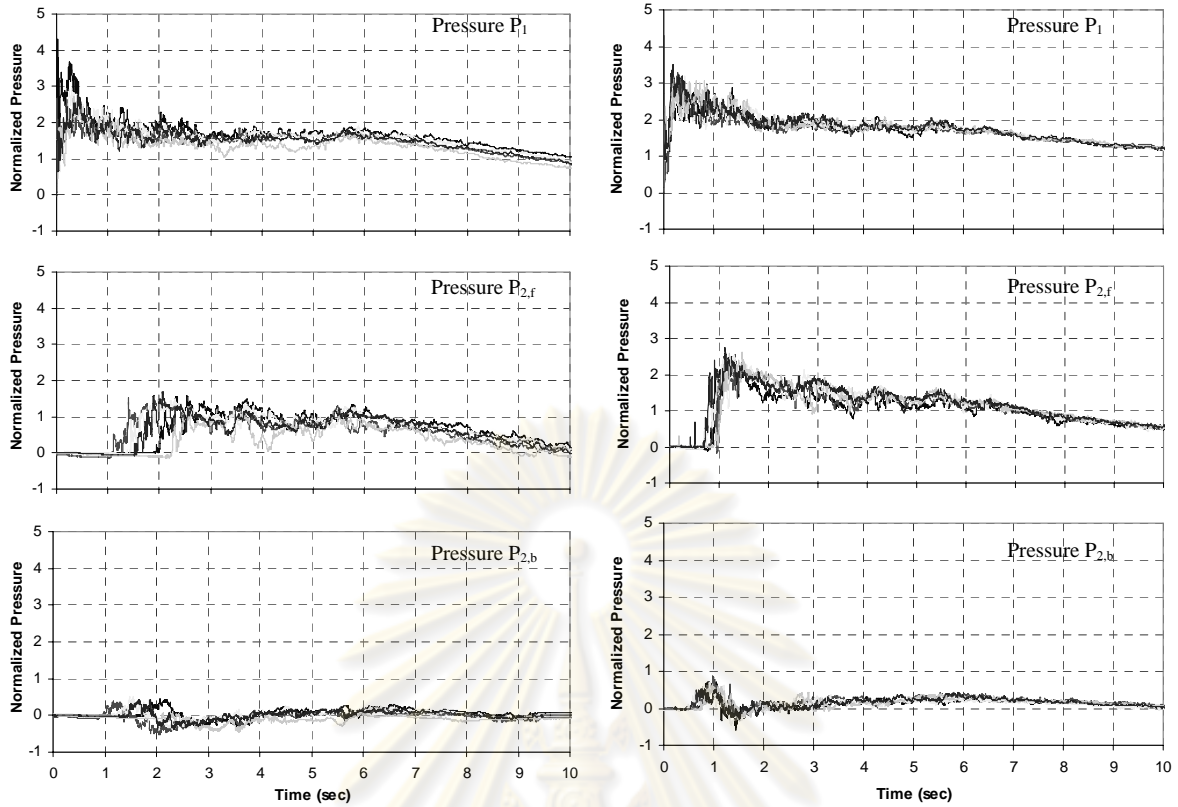
(a) G20+P0 (*H* = 65 mm)

(b) G20+P0 (*H* = 80 mm)
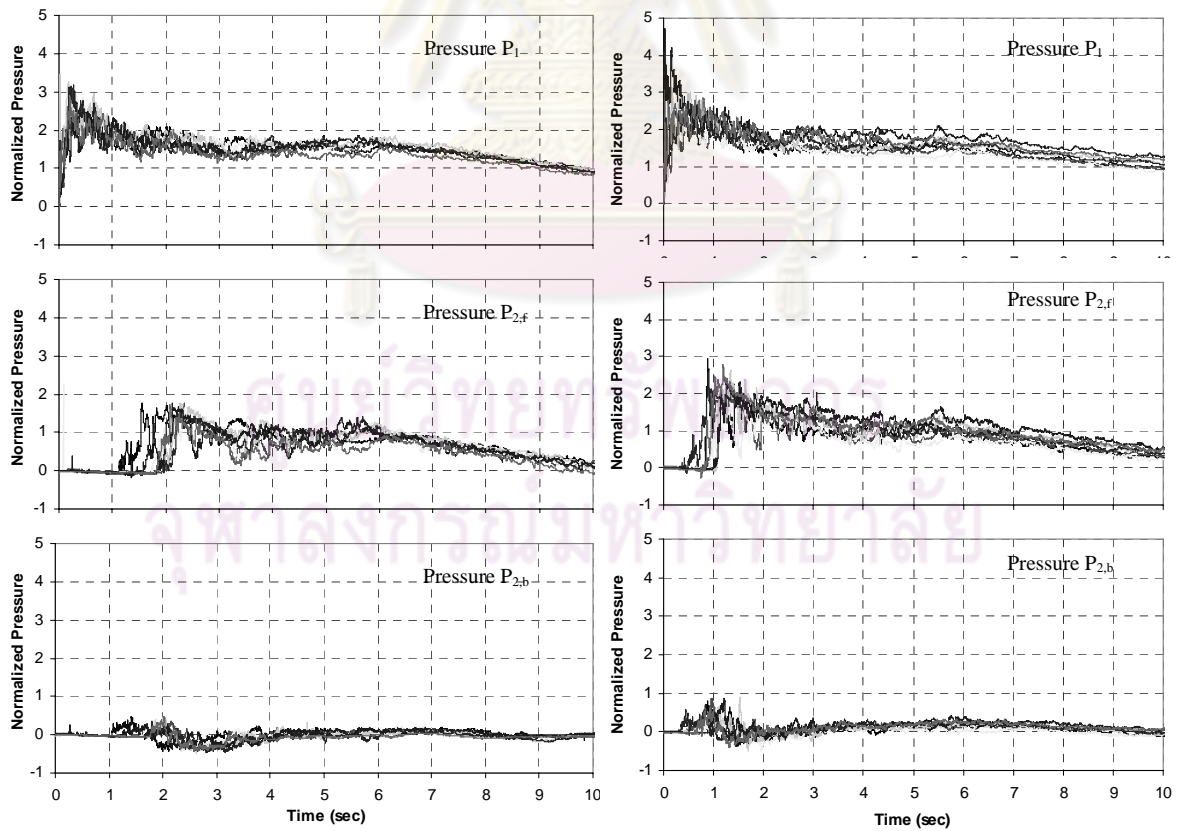
(c) G20+P20 (*H* = 65 mm)

(d) G20+P20 (*H* = 80 mm)

Figure C2 Time histories of pressures for perforated bridge decks
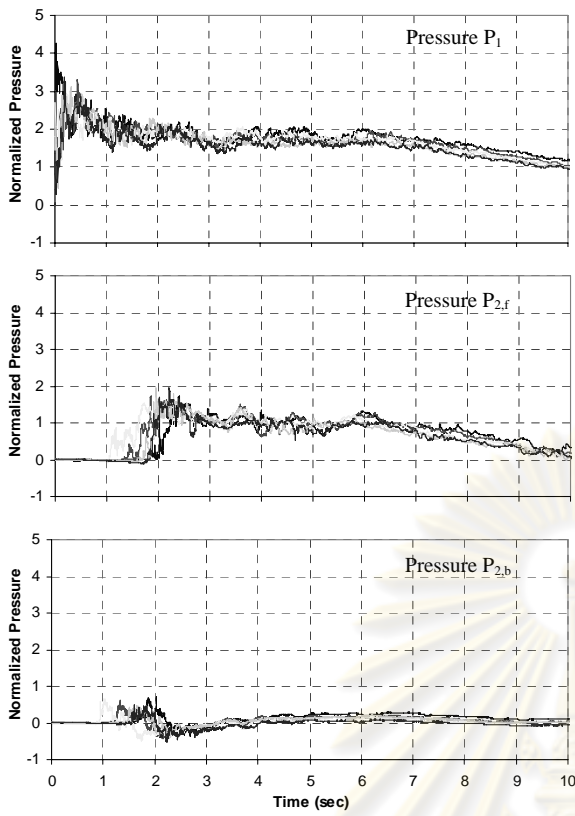
(e) G0+P60 (H = 65 mm)
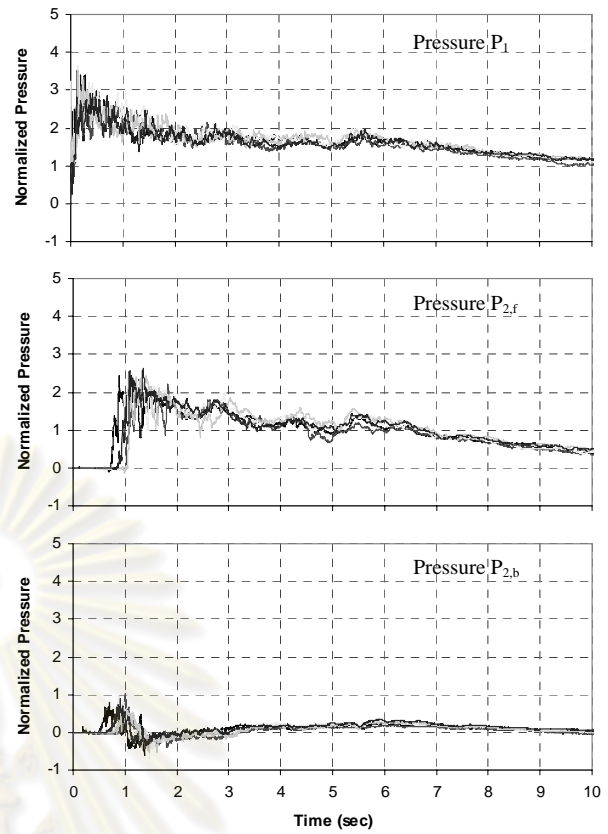
(f) G0+P60 (H = 80 mm)
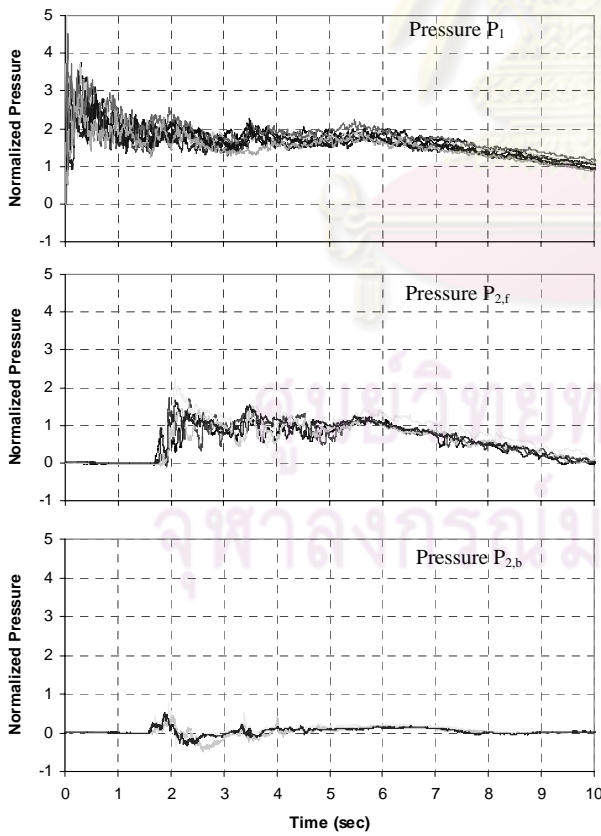
(g) G10+P60 (H = 65 mm)
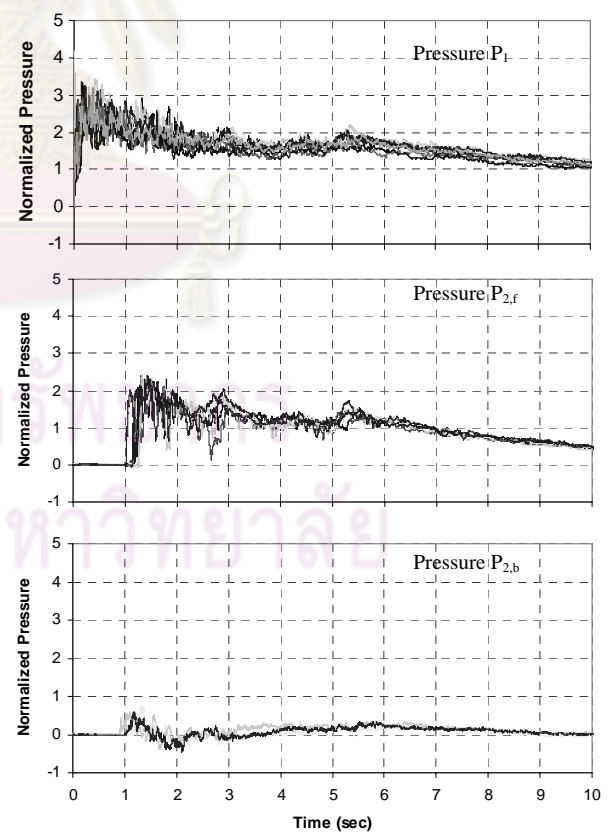
(h) G10+P60 (H = 80 mm)

Figure C2 (Cont'd)

Appendix D

Pressure and Flow Velocity at 8 m Nominal Wave Height
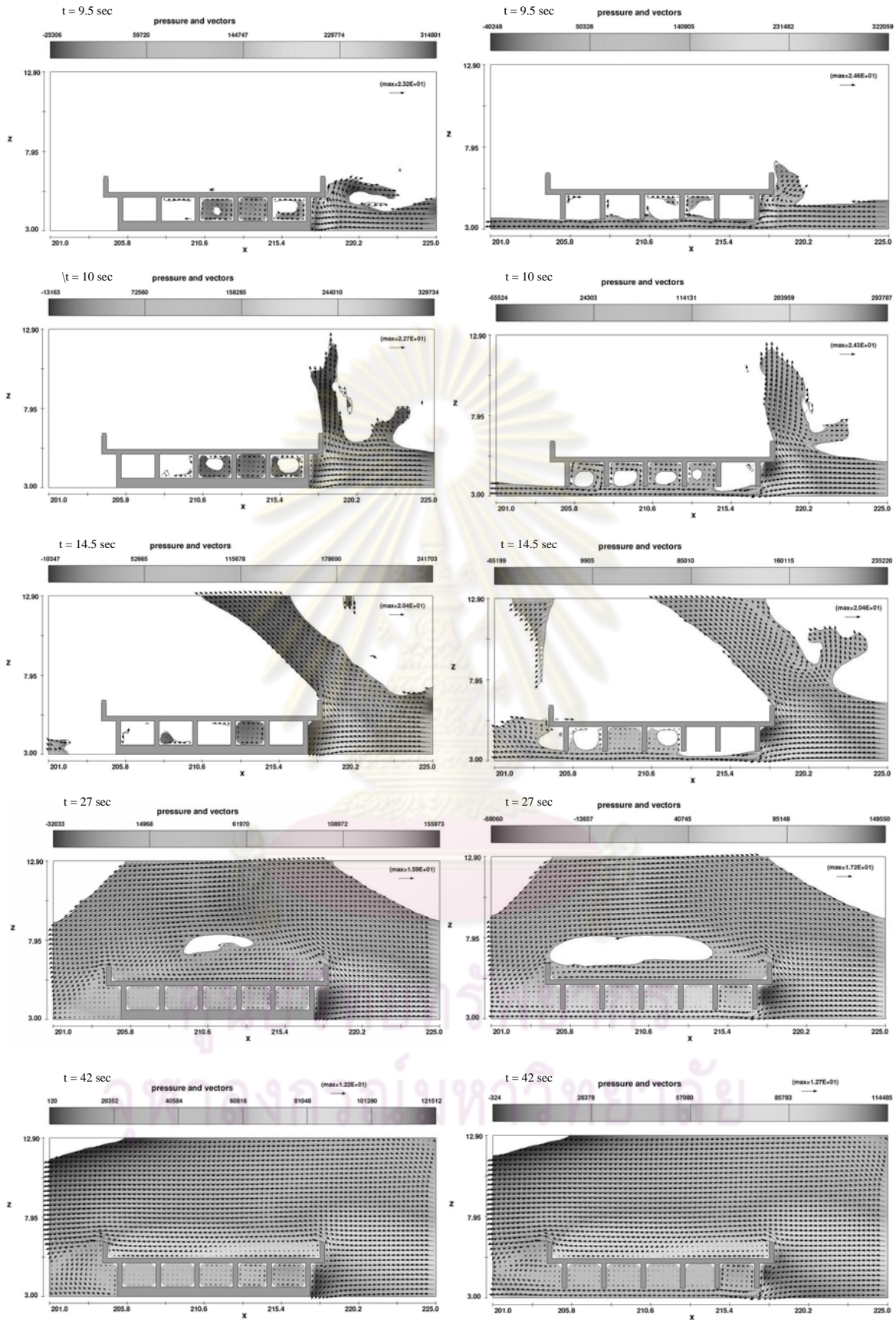
Figure D1 Pressure (color) and flow velocity (vector) at the (left) end-span and (right)
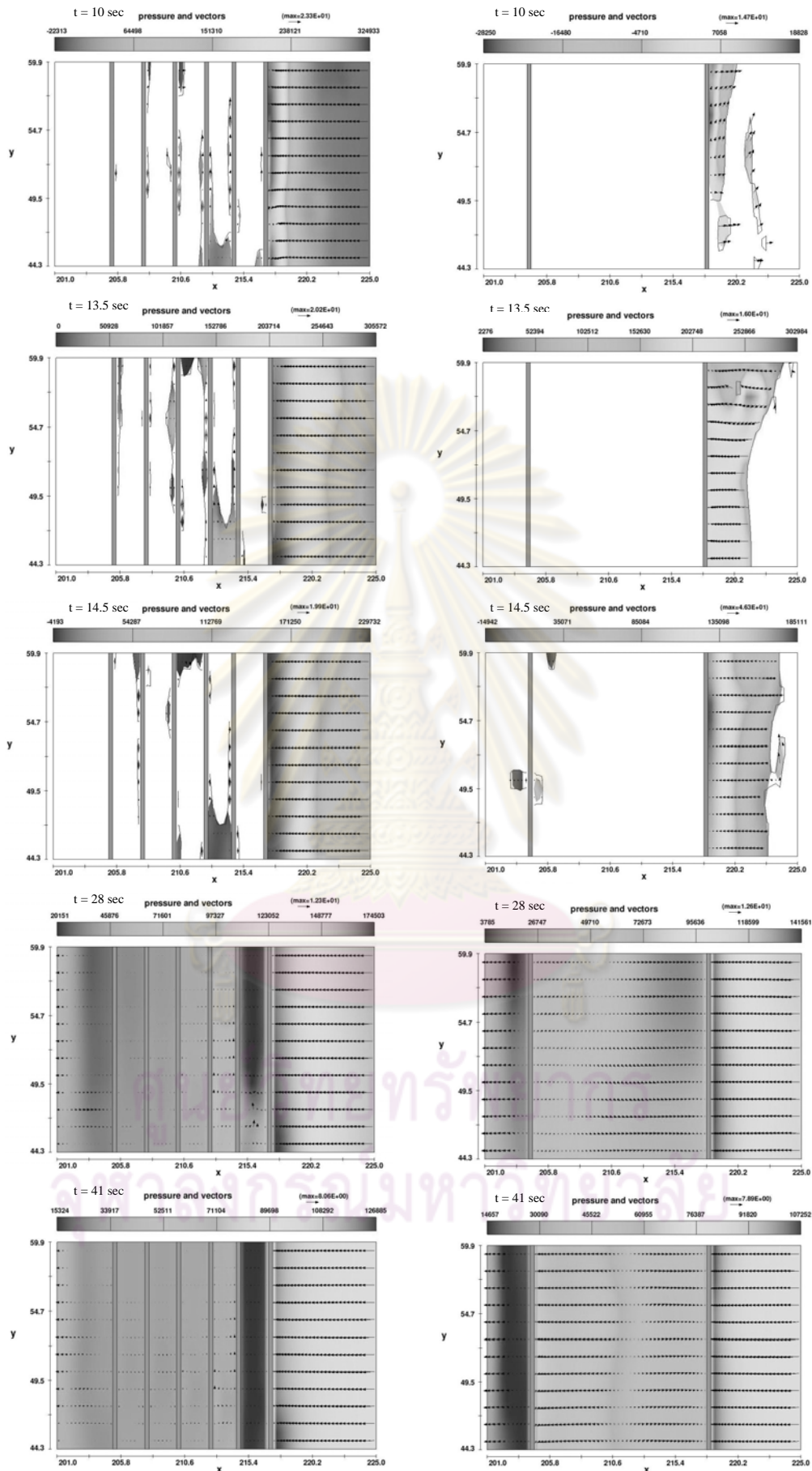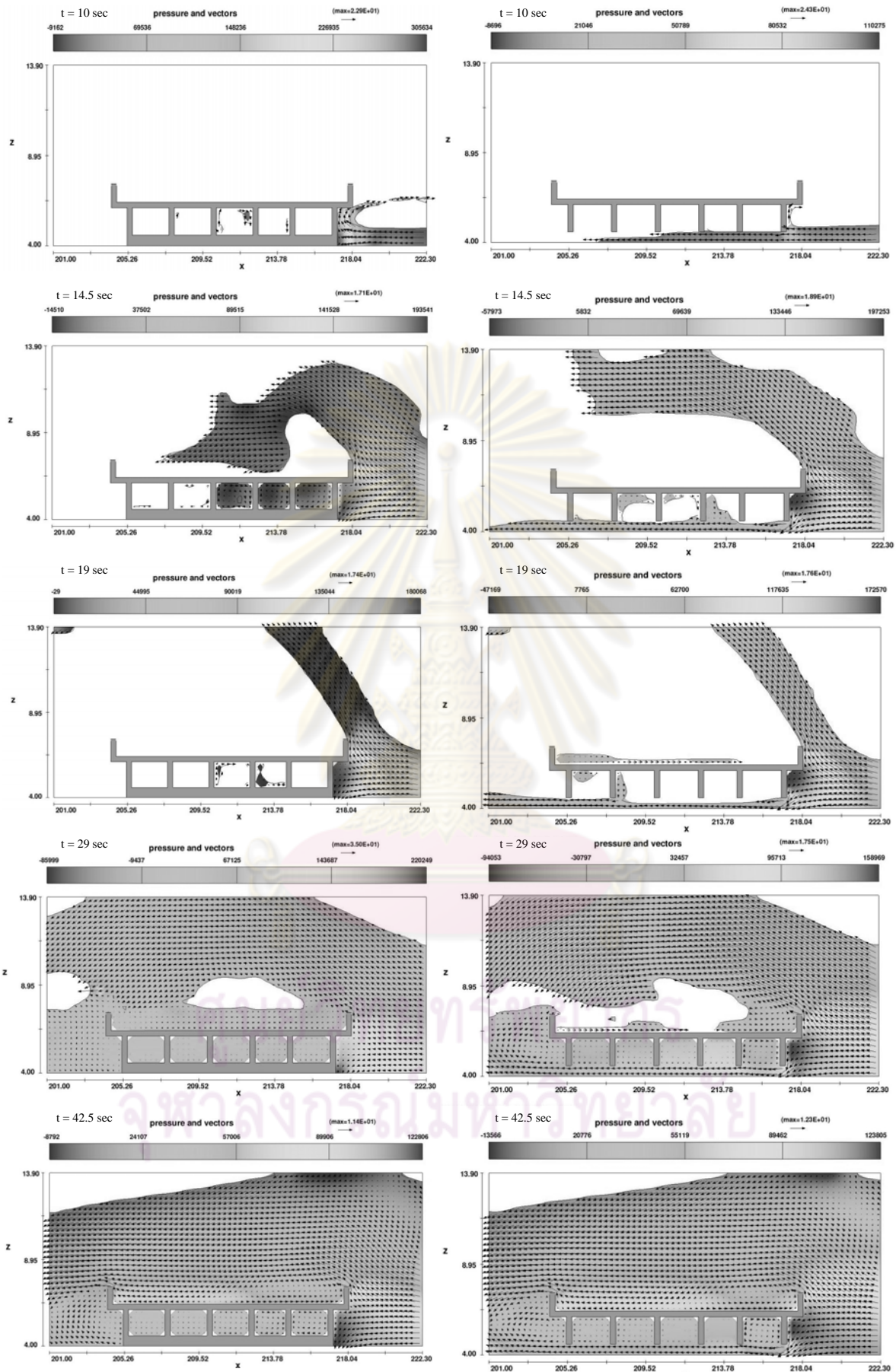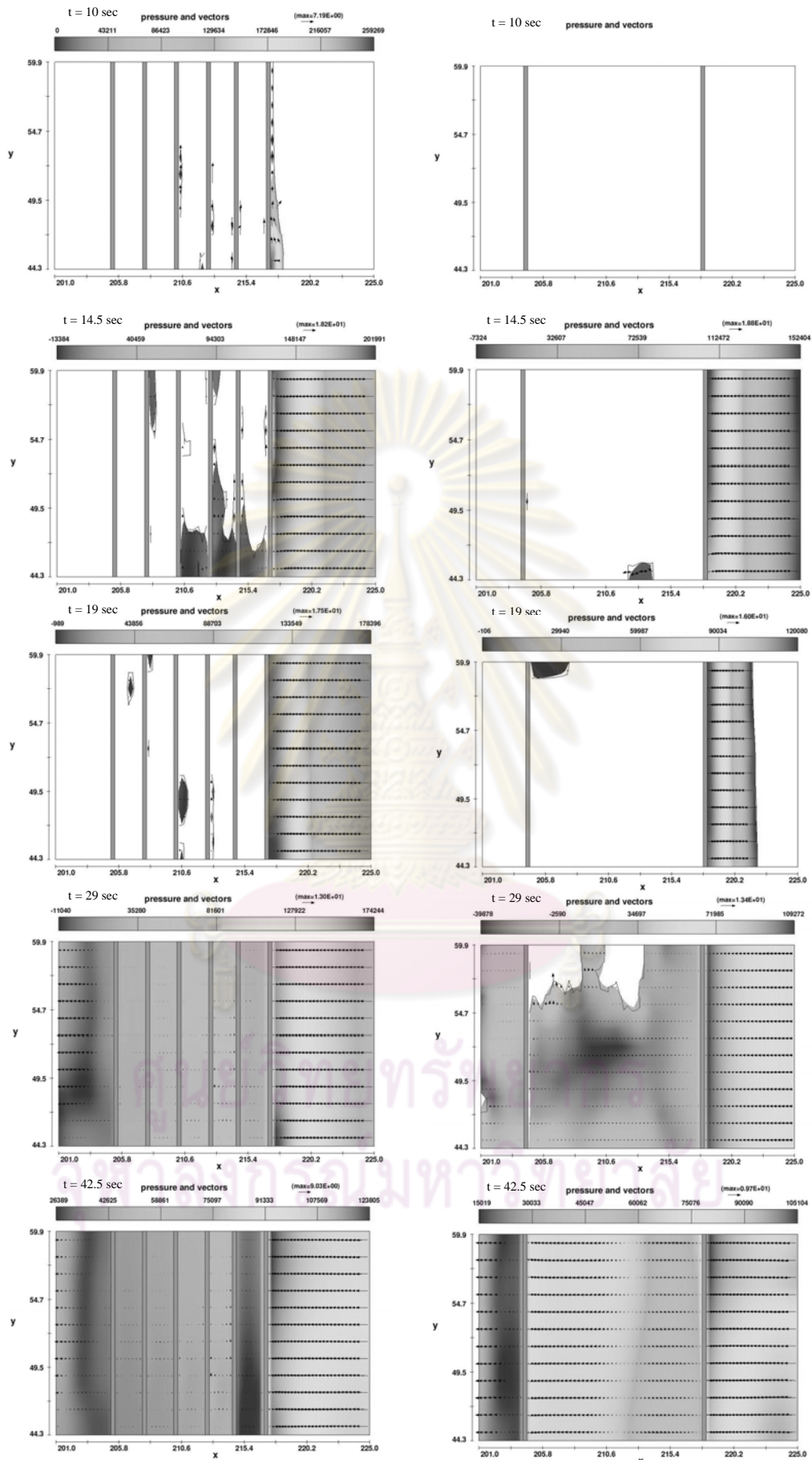
mid-span for CR36
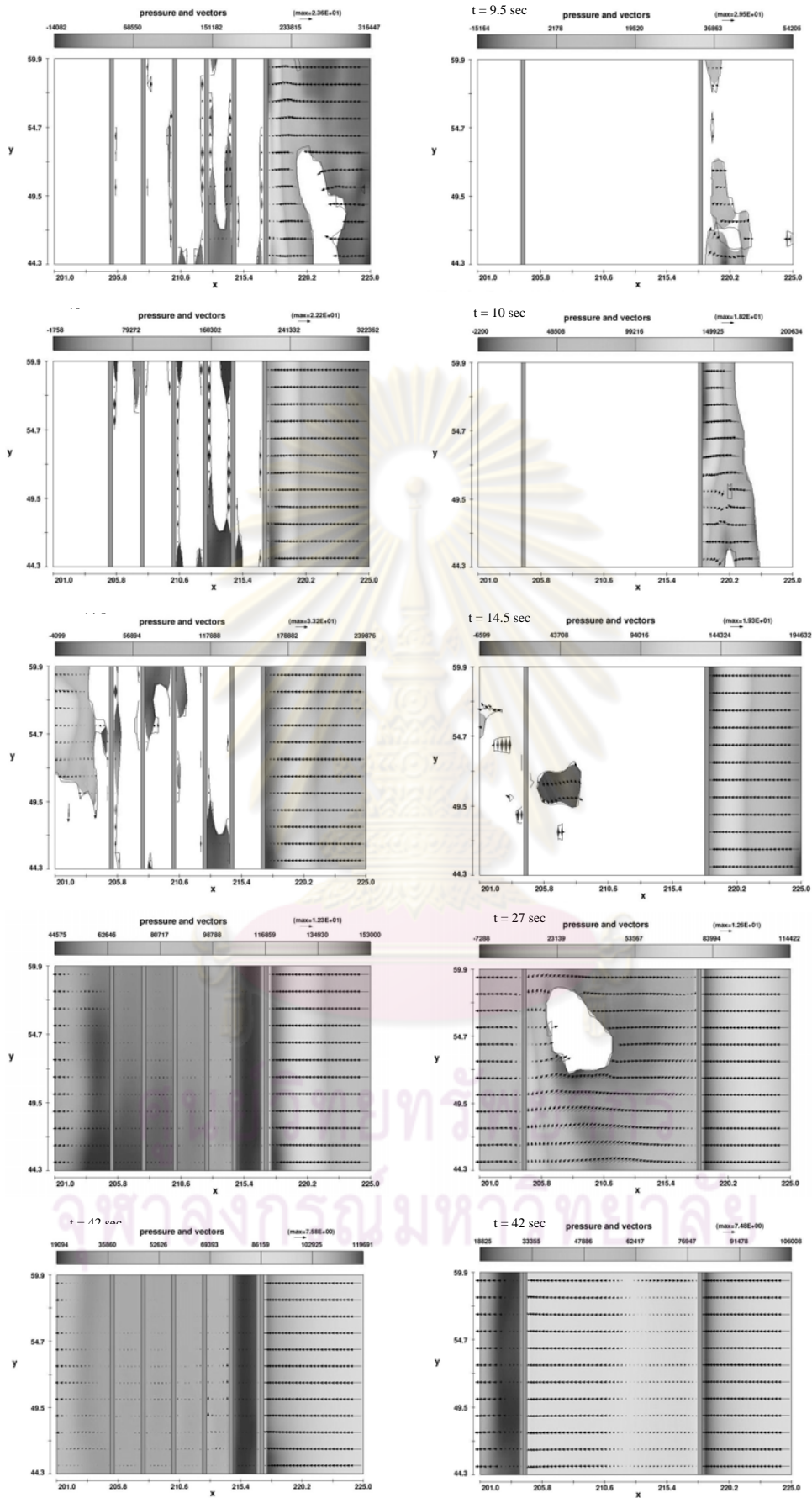
Figure D2 Pressure (color) and flow velocity (vector) at the mid-height of the (left) front girder and (right) front parapet for CR36
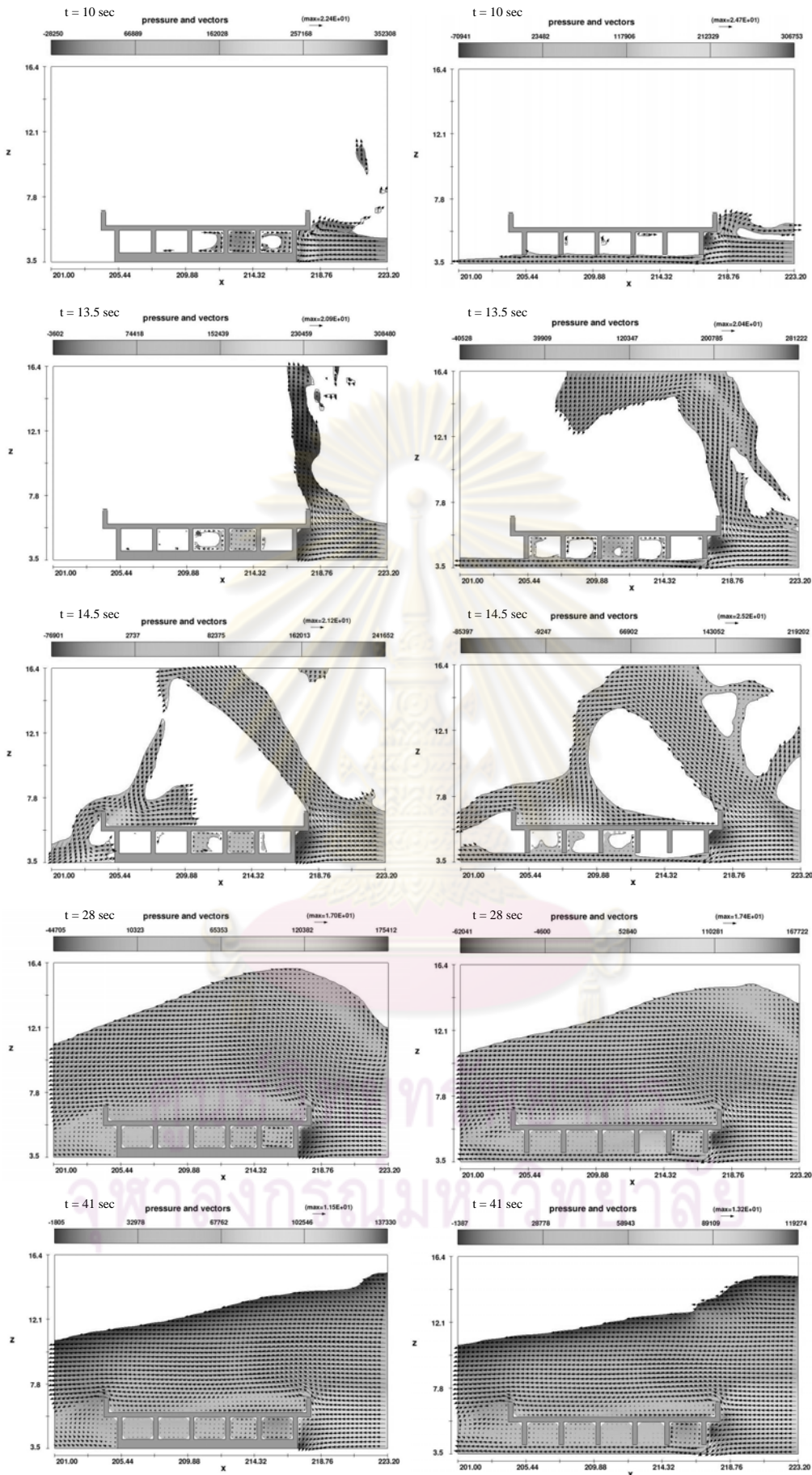
Figure D3 Pressure (color) and flow velocity (vector) at the (left) end-span and (right)

mid-span for CR41

Figure D4 Pressure (color) and flow velocity (vector) at the mid-height of the (left) front girder and (right) front parapet for CR41
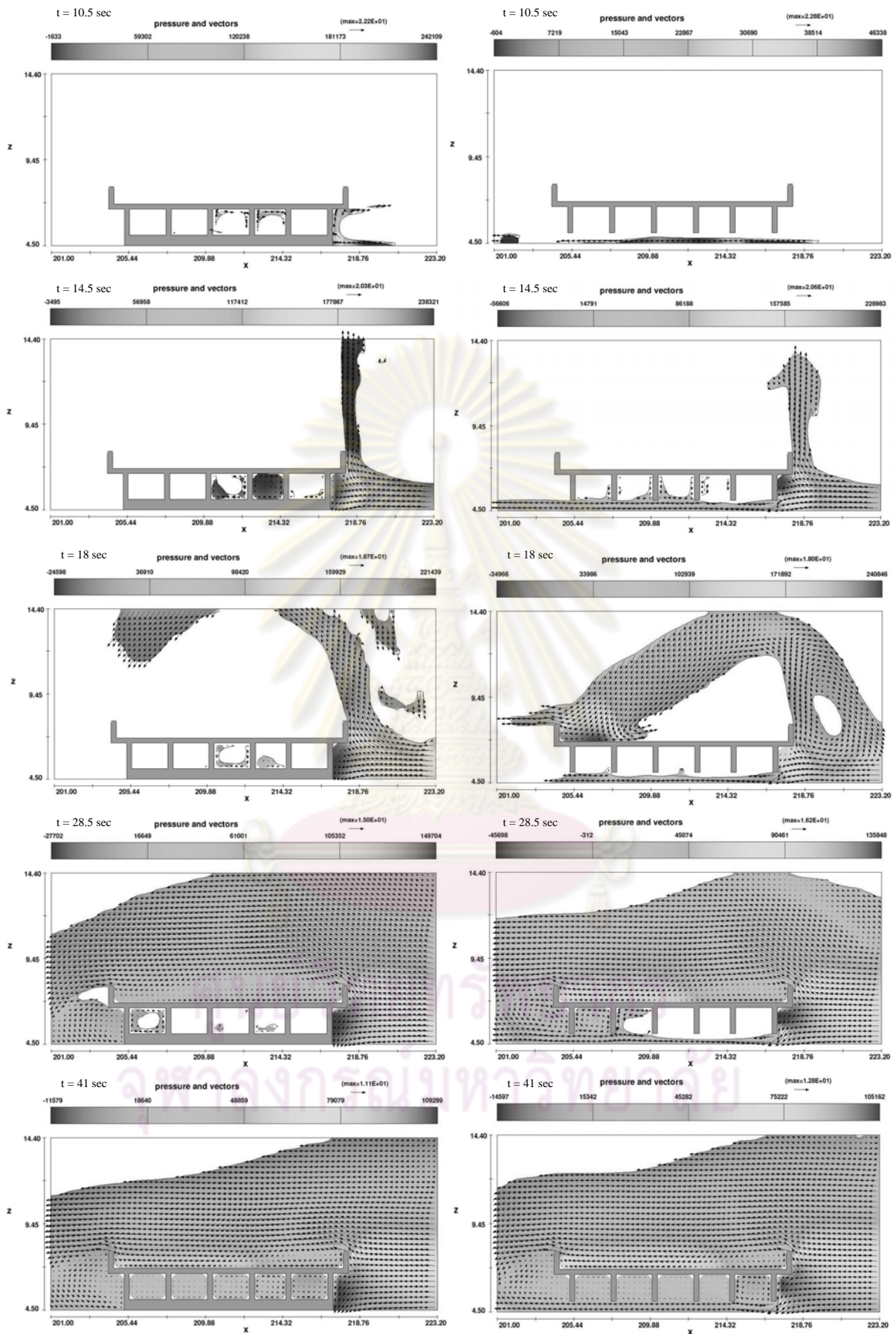
Figure D5 Pressure (color) and flow velocity (vector) at the (left) end-span and (right) mid-span for CR46

Figure D6 Pressure (color) and flow velocity (vector) at the mid-height of the (left) front

girder and (right) front parapet for CR46

Figure D7 Pressure (color) and flow velocity (vector) at the (left) end-span and (right)
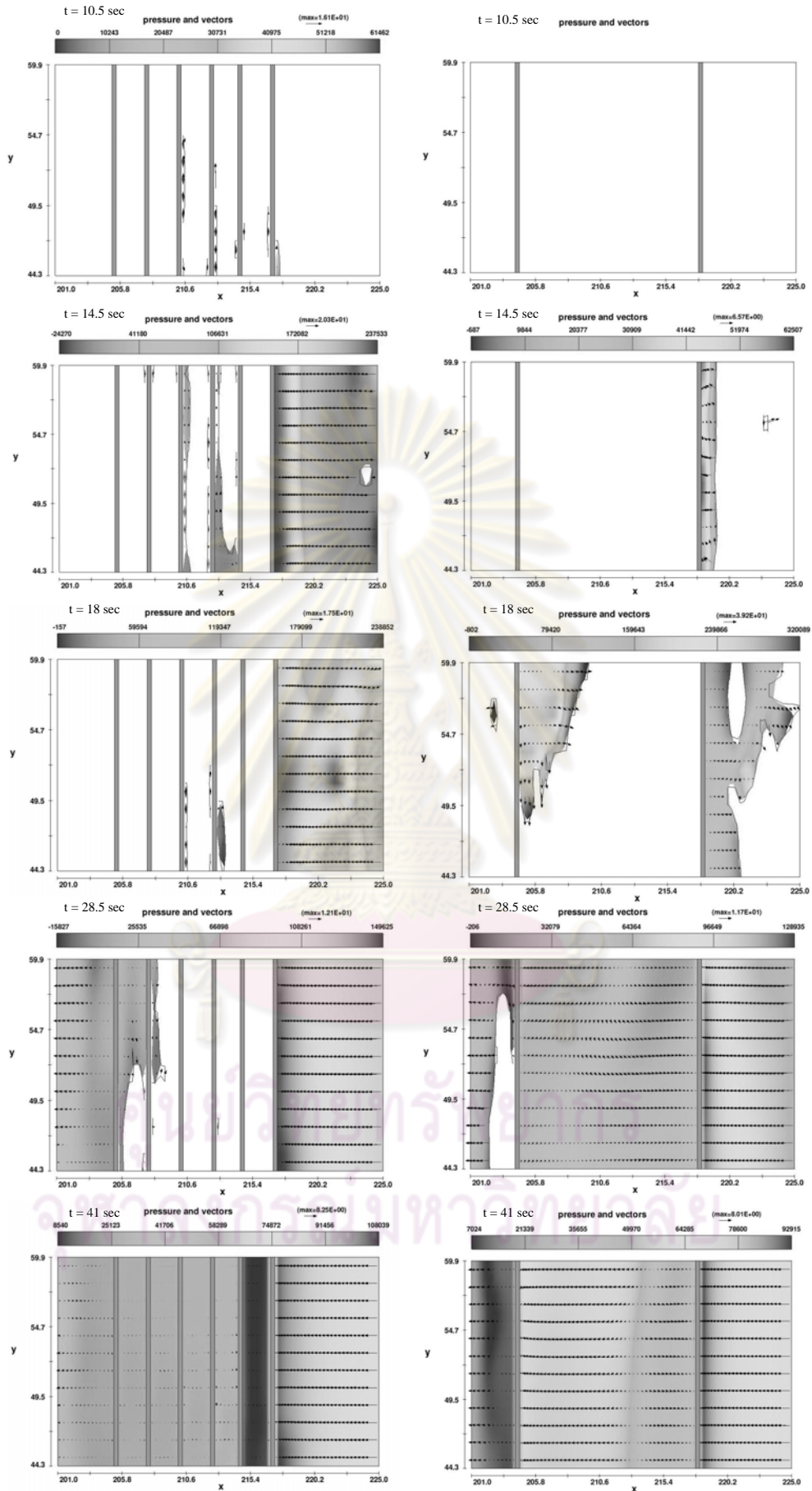
mid-span for CR51

Figure D8 Pressure (color) and flow velocity (vector) at the mid-height of the (left) front girder and (right) front parapet for CR51
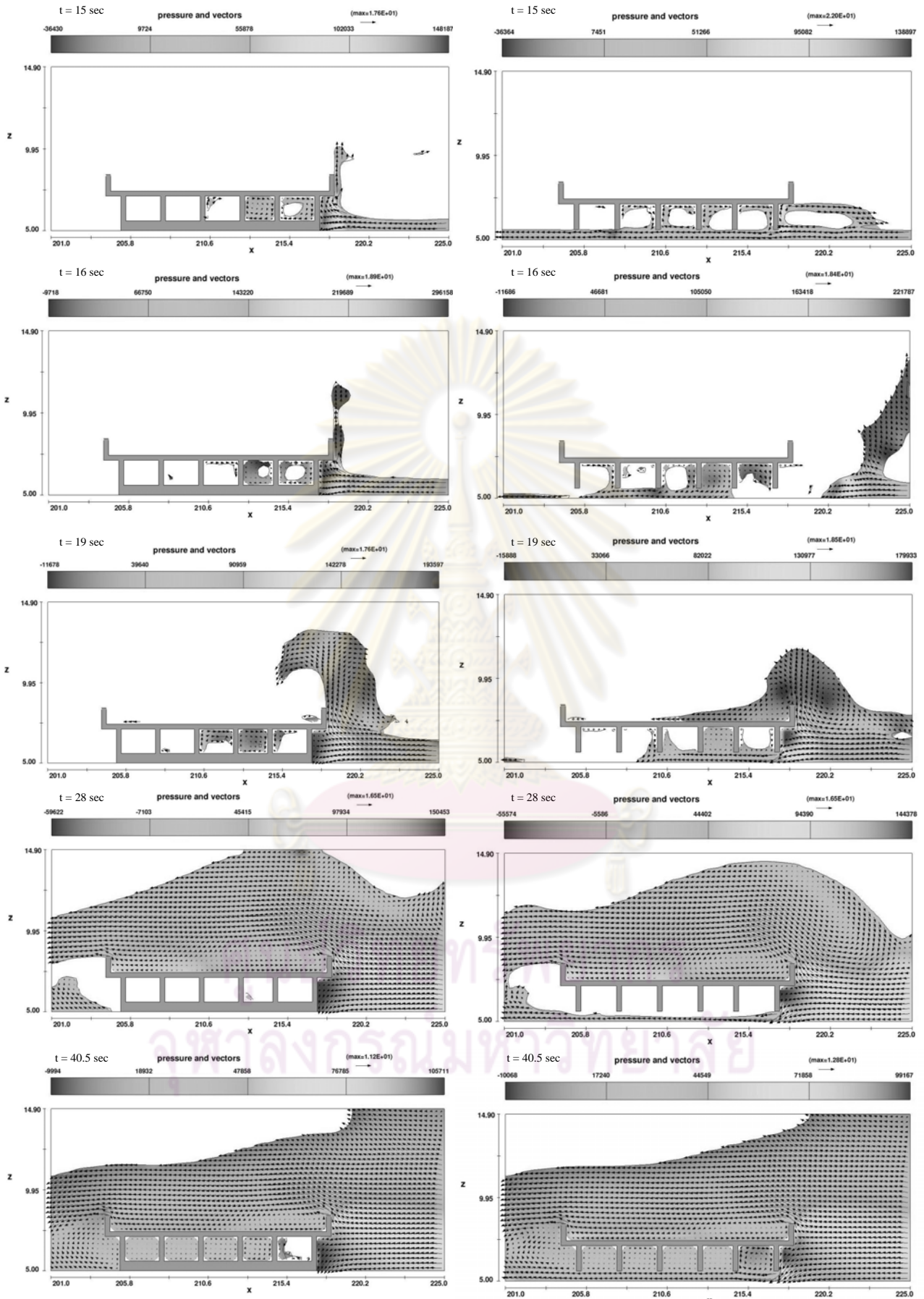
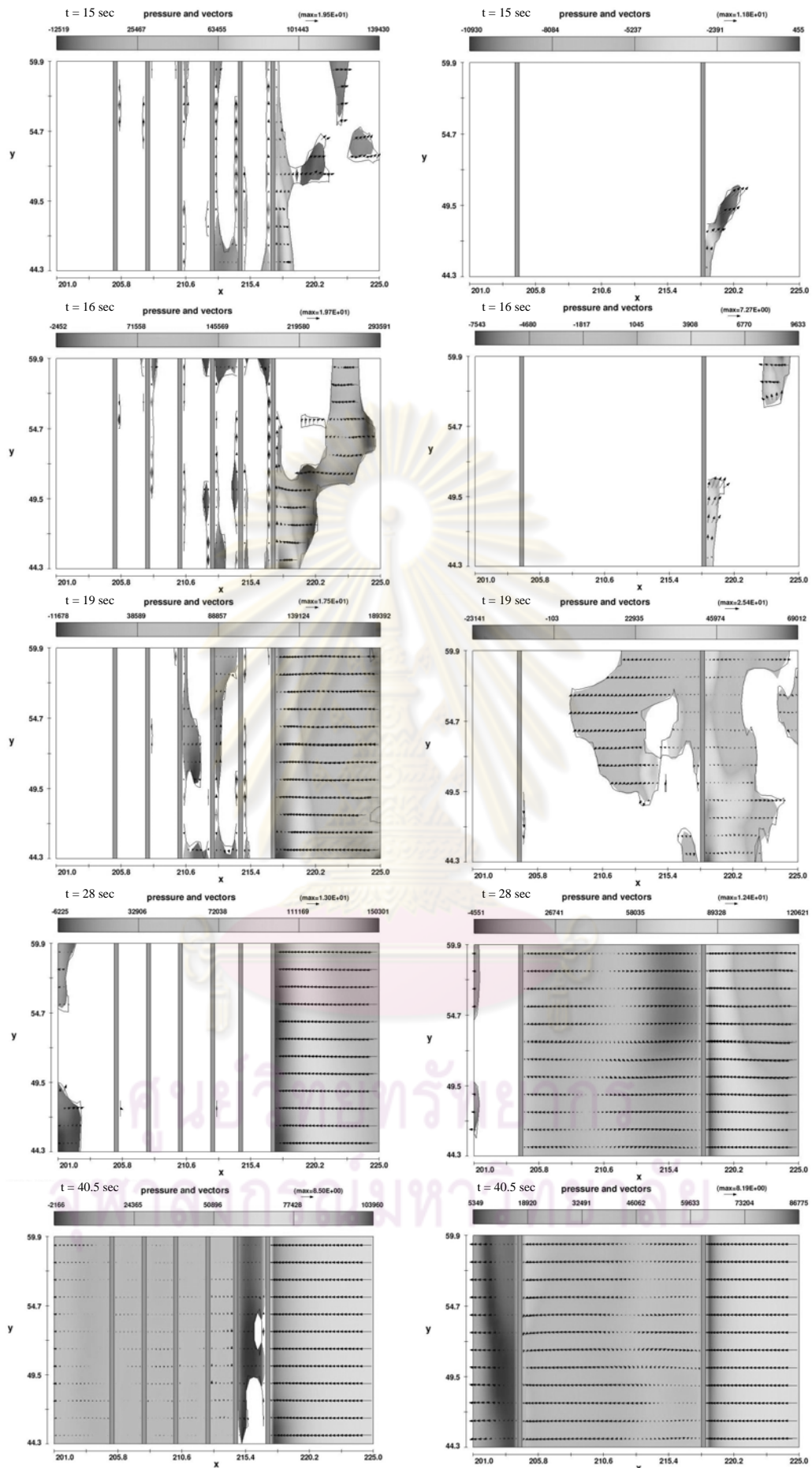Figure D9 Pressure (color) and flow velocity (vector) at the (left) end-span and (right) mid-span for CR56

Figure D10 Pressure (color) and flow velocity (vector) at the mid-height of the (left) front girder and (right) front parapet for CR56
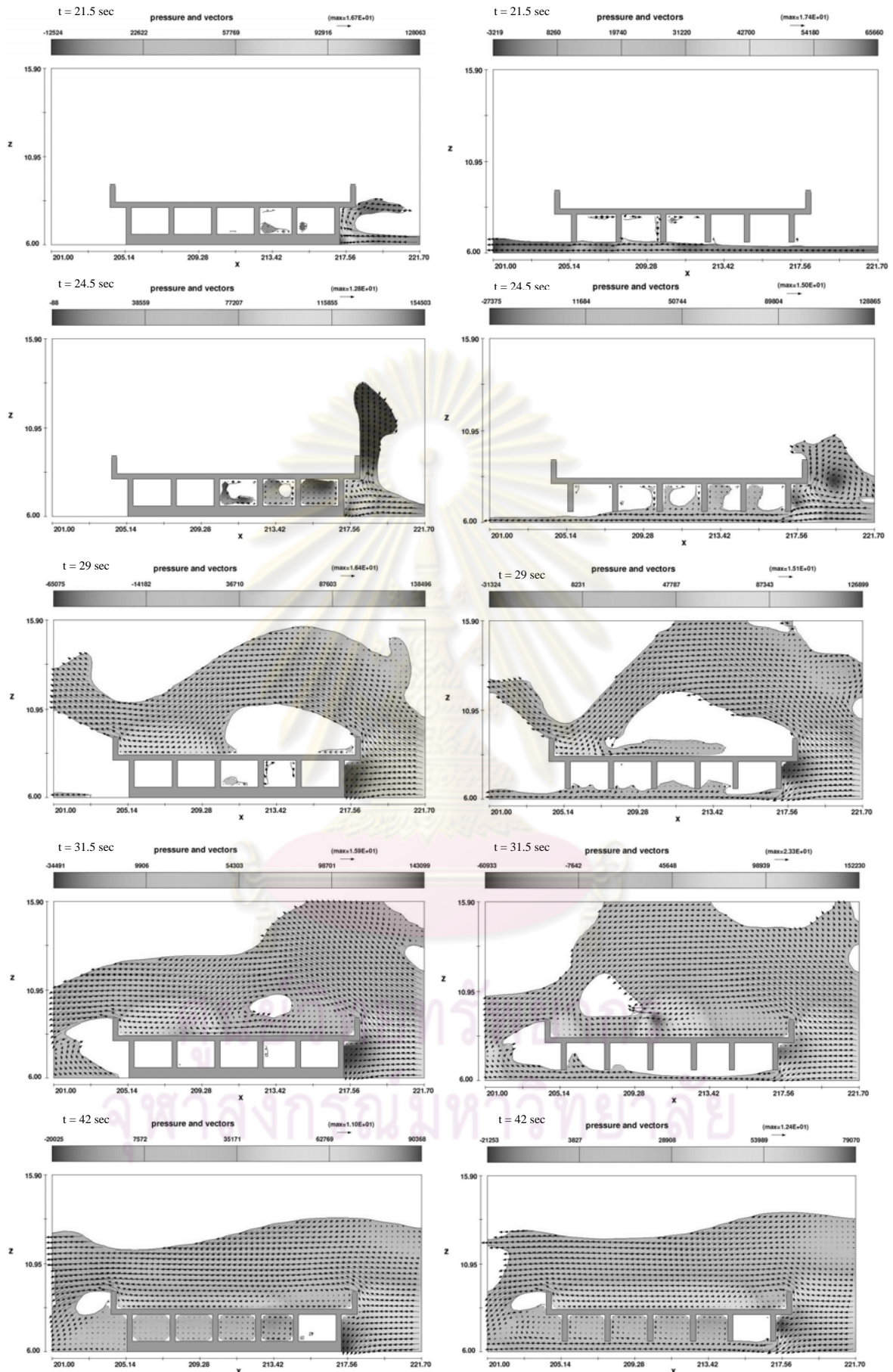
Figure D11 Pressure (color) and flow velocity (vector) at the (left) end-span and (right) mid-span for CR66
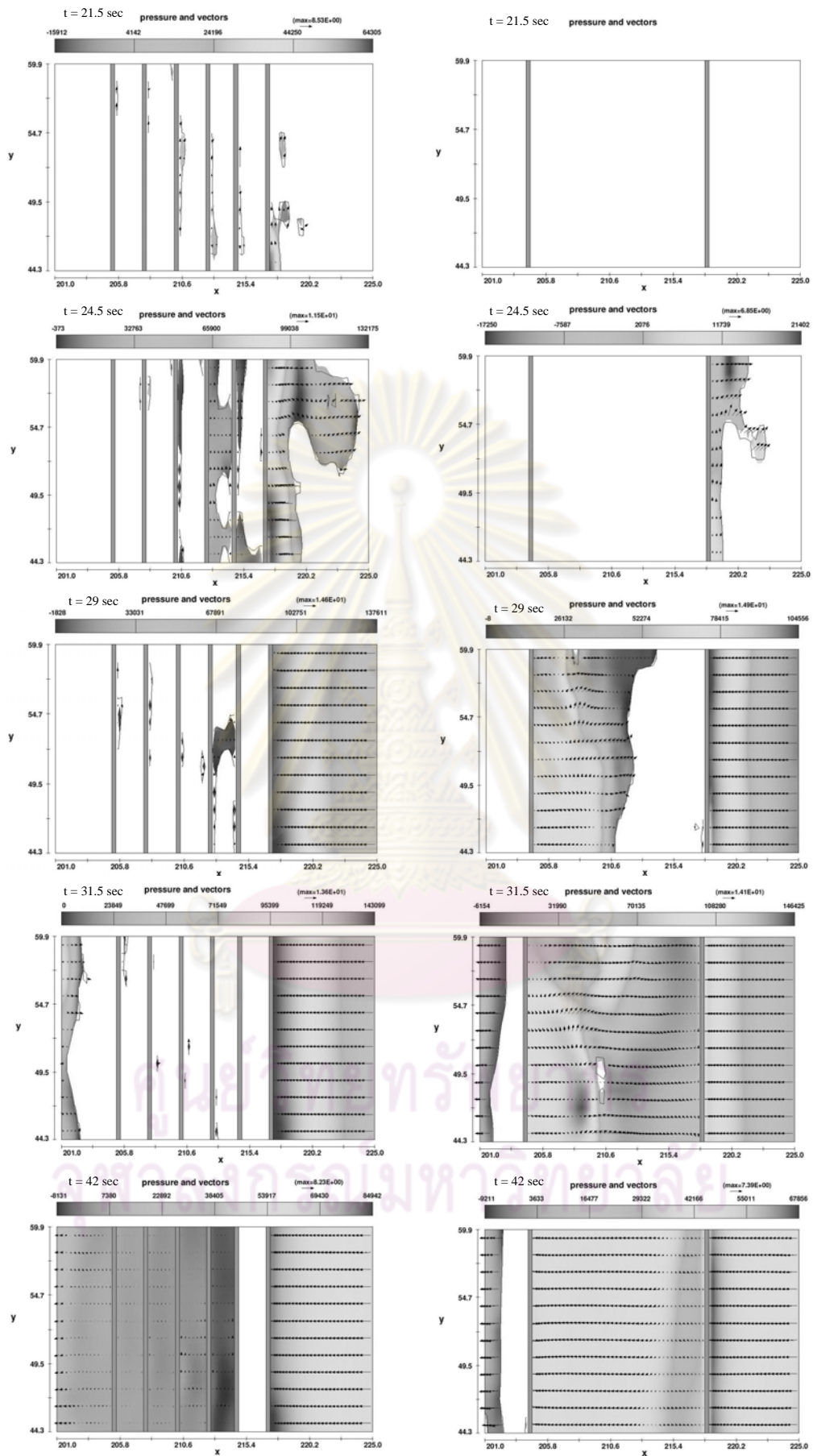
Figure D12 Pressure (color) and flow velocity (vector) at the mid-height of the (left) front girder and (right) front parapet for CR66
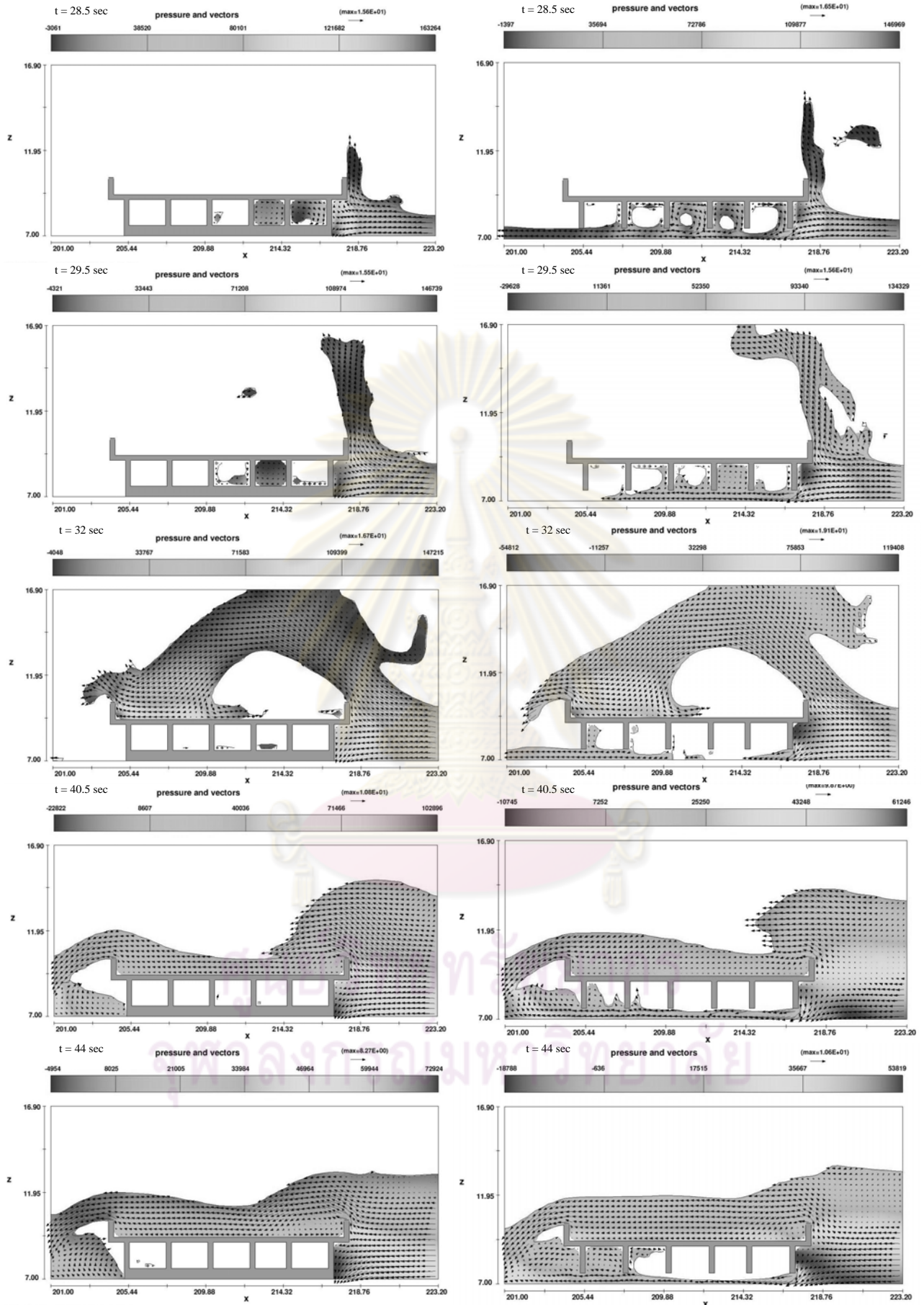
Figure D13 Pressure (color) and flow velocity (vector) at the (left) end-span and (right) mid-span for CR76
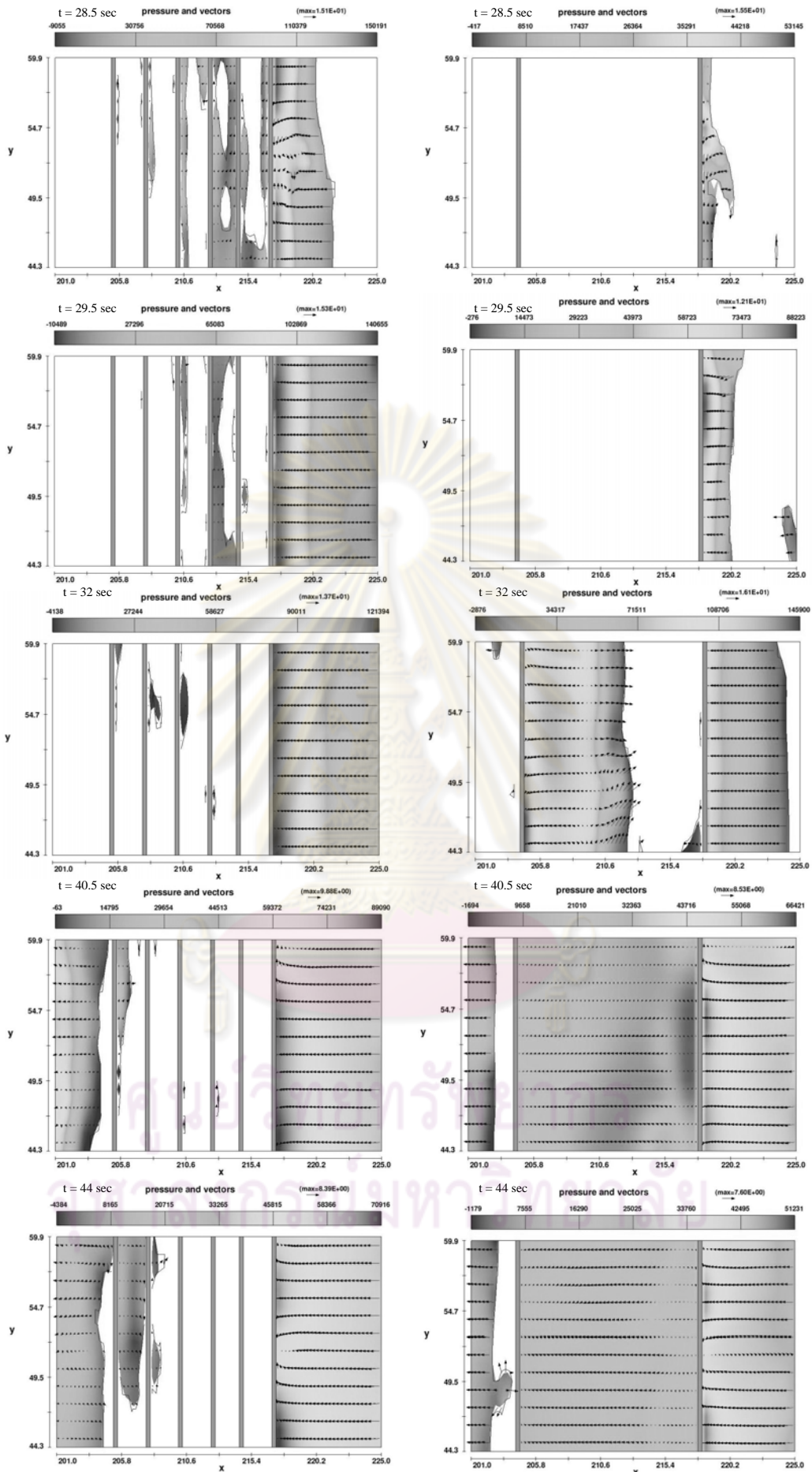
Figure D14 Pressure (color) and flow velocity (vector) at the mid-height of the (left) front girder and (right) front parapet for CR76

Appendix E

Publications and Presentations

International Journal Papers

1. **Lau, T.L.**, Lukkunaprasit, P., Ruangrassamee, A., Ohmachi, T. "Performance of Bridges with Solid and Perforated Parapets in Resisting Tsunami Attacks," (Accepted in the Journal of Earthquake and Tsunami – Special Volume).

2. **Lau, T.L.**, Lukkunaprasit, A., Ohmachi, T. "An Experimental Investigation of Tsunami Action on an Inland Bridge using a Complete Pier-Deck Bridge Model," (Provisionally accepted in the Coastal Engineering Journal).

International Conference Papers

1. **Lau, T.L.**, Lukkunaprasit, P., Ruangrassamee, A., Ohmachi, T. "Performance of Bridges with Solid and Perforated Parapets in Resisting Tsunami Attacks," *Proceedings of the International Symposium on the Restoration Program from Giant Earthquakes and Tsunamis*, Phuket, Thailand, Jan 22-24, 2008, pp. 155-160.

2. **Lau, T.L.**, Lukkunaprasit, P., Ruangrassamee, A., Ohmachi, T. "Physical Modeling: an Estimation of Wave Forces on an Inland Bridge Subject to Tsunami Bores," *Proceedings of the 5th International Conference on Urban Earthquake Engineering*, Tokyo, Japan, March 3-4, 2008, pp. 441-446.

3. **Lau, T.L.**, Ohmachi, T., Lukkunaprasit, P., Ruangrassamee, A. "Tsunami Forces on Bridge Deck Estimated from Hydraulic Model Experiments," The 10th JSCE International Summer Symposium, Tokyo, Japan, Sept 18, 2008.

4. Lukkunaprasit, P., **Lau, T.L.**, Ruangrassamee, A., Ohmachi, T. "Tsunami Wave Loading on a Bridge Deck with Perforations," *Proceedings of the 14th World Conference on Earthquake Engineering*, Beijing, China, Oct 12-17, 2008.

5. **Lau, T.L.**, Ohmachi, T., Inoue, S. "Numerical Simulation of Tsunami Flow around I-Girder Bridge Decks," *Proceedings of the 6th International Conference on Urban Earthquake Engineering*, Tokyo, Japan, March 3-4, 2009, pp. 823-828.

VITAE

Tze Liang Lau was born in Penang, Malaysia on January 8th, 1975. He received the B.Eng. (Hons.) degree in Civil Engineering and M.Sc. degree in Structural Engineering from Universiti Sains Malaysia in 1999 and 2001, respectively. He is an academic staff of the School of Civil Engineering, Universiti Sains Malaysia since April, 2004. During his doctoral study in Chulalongkorn University under the support from the Japan International Cooperation Agency (JICA) Project for AUN/SEED-Net (June 2006 - May 2009), he was a visiting research student at Ohmachi Laboratory, Tokyo Institute of Technology, Japan from February, 2008 until January, 2009. His research interests include various areas of tsunami and earthquake engineering.